Topics in Cosmology and Gravitation

by

Francis Duplessis

A Dissertation Presented in Partial Fulfillment
of the Requirements for the Degree
Doctor of Philosophy

Approved March 2017 by the
Graduate Supervisory Committee:

Damien Easson, Chair
Philip Mauskopf
Maulik Parikh
Tanmay Vachaspati

ARIZONA STATE UNIVERSITY

May 2017

ABSTRACT

Two ideas that extends on the theory of General Relativity are introduced and then the phenomenology they can offer is explored. The first idea shows how certain types of $f(R)$ gravity allows for traversable wormholes among its vacuum solutions. This is surprising to find in such simple setting as these type of solutions usually requires fairly complex constructions to satisfy the equations of motion of a gravitational theory. The second idea is the matter bounce description of the early universe where a fairly unique feature of the model is identified. Consequences of this feature could allow the paradigm to distinguish itself from other alternative descriptions, such as inflation, through late time observations. An explicit example of this claim is worked out by studying a model involving an interaction in the dark sector. Results of a more astrophysical nature, where a careful analysis of the morphology of blazar halos is performed, are also presented in the Appendix. The analysis determined that the Q-statistic is an appropriate tool to probe the properties of the intergalactic magnetic fields responsible for the halos formation.

ACKNOWLEDGMENTS

If it weren't for an entourage of great mentors, friends and family, the blood and sweat that dripped as this thesis was forged would have caused me serious mental scars.

As such I'd first like to thank my advisor Damien Easson who was always supportive of my endeavors and willing to stick his neck out in order to help whenever things got tough. In the same vain, I am also incredibly grateful to Robert H. Brandenberger, Yifu Cai and Tanmay Vachaspati. These four persons expressed patience with my pessimism and gave me the nudges I needed to accomplish my goals. Beyond mentorship, I also consider them friends through the many times we've broke bread together.

I also thank my committee members Maulik Parikh with who I had many fruitful discussion about physics and Phil Mauskopf whose curiosity, knowledge and broad interest of physics is something to aspire to.

A warm thank you to all my other collaborators over the years, they've taught me invaluable lessons: E. McDonough, E. Saridakis, D. Wang and Y. Wang. I also extend it to the numerous friends that I've gathered through the degree: Juggalo Chad, Jeff Hyde, Yao Ji, Hank Lamm, Jayden Newstead, Nadia Newstead Zatsepin, Nikhil Monga, Subir Sabharwal, Ayush Saurabh, Patrick [a.k.a. PER, PCR, P3] Sims, Robert Strausbaugh, Russ Terbeek and all others I might have missed.

A special shutout to any of the crews associated with 4016 S Holbrook Ln or Legacy. It is unlikely that they ever see this, but you know who you are if you do. Some of the best memories of my time in this State (and beyond!) have been shared with you guys. In the same context, I am indebted to Mark George Wirth who converted me into an outdoorsy person which reshaped some of my outlook on life. Through a bunch of effort we finally became *sort of alright* climbers. Hopefully our quest to crush the gnar will continue well beyond our time in Arizona and we might achieve the statue of *decent* climber someday.

A big thanks to Marylin for her generosity in letting me borrow her husband for all those

climbing trips.

One cannot forget to mention the $\mathscr{BMF}$ group comprised of Eliot Hijano and Grant Salton. It could even be argued that Hobby the Fish is a honorary member due to a brief participation. Two head, one foot.

Finally, j'aimerais remercier ma petite famille qui m'encourageait de loin. À Lise et Doug et leurs capabilités surhumaine en tant que randonneurs. À Grand Papa et ces e-mails. Merci Popa d'être venue m'aidez à m'installer et pour les visites avec Sylvie! Merci Fred et Isa d'avoir osé grimper de grandes montagnes. Merci Maman pour ton empathie sur mon impatience avec les téléphones, et merci à toi et Pierre d'avoir passé me rendre visite durant le dernier sprint. Bye Trixie, bonne chance dans le néant.

TABLE OF CONTENTS

LIST OF FIGURES

Figure Page

CHAPTER 1

INTRODUCTION: CONTRIBUTION OF THE AUTHOR

This thesis presents 3 papers co-written by the author of this thesis while in collaboration with many individuals. In High Energy Physcis, it is the custom to list the authors of a paper in alphabetical order and not based on the magnitude of the workload. For the three papers being showcased, the author of this thesis was a main contributor in working out the details, content and writing of the papers.

The papers were lightly formatted and modified from their published versions to fit the flow of the thesis. Chapter 3 presents the paper *Traversable wormholes & non-singular black holes from the vacuum of quadratic gravity* [1] co-written with D. Easson. This work discovered new exotic solutions, namely transversable wormholes, that were found in the vacuum of a class of very simple $f(R)$ theories of gravity. The solutions themselves were also elegant, a feature that is not commonly seen in the literature of wormholes. This simplicity was possible because of the existence of solutions that were conformally singular in these theories.

Chapter 5 presents the paper *Searching for a matter bounce cosmology with low redshift observations* [3] co-written with Y-F. Cai, D. Easson and D.G. Wang. The Matter Bounce alternative to cosmological Inflation is shown to possess an interesting feature that is largely model independant. Namely, the energy scale at which the perturbations are set is small enough that the possible range can be probed by late time observations. This opens a new way of testing these models as the physical principles that operated during the generation of the perturbations that are eventually seen in the CMB should also be revelant today.

Finally, Appendix C presents the paper *Probing Stochastic Inter-Galactic Magnetic Fields Using Blazar-Induced Gamma Ray Halo Morphology* [4] co-written with T. Vachaspati. In this chapter we've extended previous work found in the literature to investigate the morphologies of blazar halos. We introduced the Pair-Production (PP) surface which gives a nice visualization to understand how the halo shapes are determined. We also investigated whether the Q-statistic is a useful tool to extract information about the magnetic field responsible for the halo formation. It was shown that the statistic is sensitive to the helicity, strength and coherence length of the magnetic field.

CHAPTER 2

A BRIEF OVERVIEW OF MODIFIED GRAVITY

It was in 1915 that Albert Einstein first proposed the full mathematical framework of General Relativity (GR) [5], a theory which currently represent our best understanding of gravity. Since then, it became apparent that the initial logical steps leading to GR did not make it entirely unique; Einstein's original framework was only the simplest possibility. Although no observations suggests the need of a more complex gravitational theory, the motivations for additional research on extensions of GR came from a theoretical standpoint. For instance, it is known that GR cannot be renormalized (see [6] for a review) while some alternatives do not a priori have that problem.

The state of the art understanding of GR comes from a Quantum Field Theory (QFT) perspective. Assuming Lorentz invariance, Weinberg has shown [7] that GR is the unique Lagrangian solely describing a massless spin-2 field in four dimensions. A consistent theory of such massless field requires diffeomorphism invariance as a gauge symmetry and also implies the equivalence principle [8]. From a QFT point of view, we expect GR to be a the low energy approximation of some more complete Effective Field Theory (EFT) that includes higher order corrections. Any such extensions inevitably introduces new degrees of freedom, whether it be through adding new fields or higher curvature/derivative terms. Below, we describe how these additional terms would look like. We shall restrict our discussion to 3+1 dimensions. Moreover we will use a mostly pluses metric signature i.e. $\eta = diag(-1,1,1,1)$ and fundamental units $c = \hbar = 1$.

Let us first write down the action of GR, named the Einstein-Hilbert action,

$$S_{EH} = \int d^4x\sqrt{-g}(\frac{M_p^2}{2}R - M_p^2\Lambda), \tag{2.1}$$

with $g_{\mu\nu}$ being the metric, g its determinant, R the Ricci scalar and Λ being some constant

which we call the cosmological constant. One can add a matter content to the theory by adding S_m, the matter action, to S_{EH}. This does introduce extra degrees of freedom but we do not refer to this as a modification of gravity if they simply have minimal coupling to the metric (i.e. couplings due to derivatives being covariant $\partial_\mu \to \nabla_\mu$ and from the volume form $\sqrt{-g}d^4x$). Alternatively, there exist many non-minimal interactions between a field and the metric that can be added to S_{EH}, the galileons [9] are an example, and those type of construction fall in the realm of what we call modified gravity. We will not focus on exploring these types of models in this review, but shall instead turn our attention to theories of gravity that contains terms of higher order in curvature. Using the metric to construct the Christoffel symbols,

$$\Gamma^\rho_{\mu\nu} = \frac{1}{2}g^{\rho\zeta}\left(\partial_\mu g_{\nu\zeta} + \partial_\nu g_{\mu\zeta} - \partial_\zeta g_{\mu\nu}\right), \tag{2.2}$$

we can write down the Riemann tensor,

$$R^\rho_{\mu\zeta\nu} = \nabla_\zeta \Gamma^\rho_{\mu\nu} - \nabla_\nu \Gamma^\rho_{\mu\zeta} + \Gamma^\alpha_{\mu\nu}\Gamma^\rho_{\alpha\zeta} - \Gamma^\alpha_{\mu\zeta}\Gamma^\rho_{\alpha\nu}, \tag{2.3}$$

whose index can be contracted to form the Ricci tensor,

$$R_{\mu\nu} = R^\rho_{\mu\rho\nu}, \tag{2.4}$$

and the Ricci scalar $R = R^\mu_\mu$. At second order in curvature, the possible invariants that can be constructed out of these are,

$$R^2,\ R_{\mu\nu}R^{\mu\nu},\ R_{\rho\mu\zeta\nu}R^{\rho\mu\zeta\nu}. \tag{2.5}$$

Therefore, we can write

$$S = \int d^4x\sqrt{-g}\left(\frac{M_p^2}{2}R - M_p^2\Lambda + \alpha R^2 + \beta R_{\mu\nu}R^{\mu\nu} + \gamma R_{\mu\nu\rho\sigma}R^{\mu\nu\rho\sigma} + ...\right)$$

with the ... denoting higher order corrections and $\alpha,\ \beta,\ \gamma$ are some dimensionless coefficients.

An extended version of the original Einstein-Hilbert action is called quadratic gravity whenever one truncates any terms higher than second order in curvature. In 1977, Stelle managed to show that quadratic gravity was renormalizable [10]. However this came at a hefty price as renormalizability seemed to require terms that propagated ghosts (see appendix 5.5 for a discussion of the ghost issue). To extend this quadratic theory even further, one could also add terms having extra derivatives such as $R_{\mu_1\nu_1\rho_1\sigma_1}\mathscr{O}^{\mu_1\nu_1\rho_1\sigma_1}_{\mu_2\nu_2\rho_2\sigma_2}R^{\mu_2\nu_2\rho_2\sigma_2}$ with $\mathscr{O}$ being a differential operator. Such theories are studied in [11] where it is argued that it is possible to avoid the ghosts, as found in quadratic gravity, when considering non-local operators for $\mathscr{O}$.

If one does not demand renormalizability, then we have plenty of possibilities to extend GR without encountering ghosts. In the case of Lovelock theories [12], one demands that the equation of motions stays second order in derivatives. This requirement imposes a constraint on the Lagrangians L that can be built and force the theory to be constructed from the terms,

$$L = \sum_{m=0}^{\infty} c_m L_m, \tag{2.6}$$

$$L_m = \frac{1}{2^m}\frac{1}{m!}\delta^{a_1}_{[c_1}\delta^{b_1}_{d_1}...\delta^{a_m}_{c_m}\delta^{b_m}_{d_m]}R^{c_1d_1}_{a_1b_1}...R^{c_md_m}_{a_mb_m}. \tag{2.7}$$

The $m=0$ and $m=1$ terms yields the cosmological constant and Ricci scalar respectively. Due to the (anti)symmetries of $R_{\mu\nu\rho\sigma}$, the terms L_m are guarranteed to vanish for $m > D/2$. In our four dimensional case of interest, this yields a single extra term that is added to the EH action and it is called the Gauss-Bonnet term,

$$\mathscr{G} = R^2 - 4R^{\mu\nu}R_{\mu\nu} + R^{\mu\nu\sigma\rho}R_{\mu\nu\sigma\rho}. \tag{2.8}$$

This term is a linear combination of the invariants constructed in (2.5). To single it out, we rewrite the quadratic gravity action as,

$$S = \int d^4x\sqrt{-g}(\frac{M_p^2}{2}R - M_p^2\Lambda + \alpha R^2 + \beta C^2 + \gamma\mathscr{G}), \tag{2.9}$$

where $C^2 = C_{\mu\nu\rho\sigma}C^{\mu\nu\rho\sigma} = R^{\mu\nu\sigma\rho}R_{\mu\nu\sigma\rho} - 2R^{\mu\nu}R_{\mu\nu} + \frac{1}{3}R^2$ is the square of the Weyl curvature tensor which is responsible for the appearance of ghost degrees of freedom. The Lovelock theory has $\alpha = \beta = 0$, which eliminates the threat. Interestingly the remaining Gauss-Bonnet term is a total derivative in four dimension and can be integrated out as to not affect the equations of motions (EOM), it only becomes important when discussing questions involving spacetime boundaries. Therefore the EOM from the Lovelock theory reduces to the same as the Einstein-Hilbert action in $D = 4$. For additional details on Lovelock theories see [13].

What about the R^2 term? This coefficient is not found in the Lovelock theory as its inclusion would introduce higher than second order derivative terms in the EOM. This leads to an additional scalar degree of freedom (DOF) in the theory which is fortunately healthy [14]. An action having solely R and R^2 is a special case of a more general class of ghost-free modified gravity called, f(R) theories of gravity [15, 16]. Their Lagrangians simply replaces the Ricci scalar of the EH action by an arbitrary function of R,

$$S = \frac{M_p^2}{2}\int d^4x\sqrt{-g}f(R) + S_m. \tag{2.10}$$

Chapter 2 uncovers new exotic solutions in this class of modified gravity theories but mostly focuses on the $f(R) = R^2$ case for reasons explained in the chapter's introduction. Following [16], we will now show how f(R) theories of gravity are closely related to scalar-tensor theories in which the tensor field (the graviton) non-minimally couples to a scalar field. Let us introduce a Lagrange multiplier χ and consider the action,

$$S = \frac{M_p^2}{2}\int d^4x\sqrt{-g}[f(\chi) + f_{,\chi}(\chi)(R-\chi)] + S_m. \tag{2.11}$$

Varying the action with χ gives us the EOM,

$$f_{,\chi\chi}(\chi)(R-\chi)=0, \tag{2.12}$$

which forces $\chi = R$ if $f_{,\chi\chi}$ does not vanish. Under this circumstance, the actions (2.10) and (2.11) are equivalent and are a special case of a Brans-Dicke (BD) scalar-tensor theory,

$$S_{BD}=\int d^4x\sqrt{-g}\big[\frac{M_p^2}{2}\big(\frac{\Phi}{2}R+\frac{\omega_{BD}}{2\Phi}(\nabla\Phi)^2\big)-U(\Phi)\big]+S_m, \tag{2.13}$$

with $\Phi = df/d\chi$, $\omega_{BD}=0$ and $U(\Phi)=\frac{M_p^2}{2}\big(\chi(\Phi)\Phi-f(\chi(\Phi))\big)$.

We can go further by performing a conformal transformation. Define the rescaled metric as $\tilde{g}_{\mu\nu}=\Omega^2 g_{\mu\nu}$[1,2], and choose the conformal factor to be $\Omega=\Phi^{1/2}$. The Ricci scalar then transforms as

$$R=\Omega^{-2}\big(\tilde{R}+6\tilde{\nabla}_\mu\tilde{\nabla}^\mu\omega-6\tilde{g}^{\mu\nu}\partial_\mu\omega\partial_\nu\omega\big), \tag{2.14}$$

with $\omega=\ln\Omega=\frac{1}{2}\ln\Phi$. Moreover the volume form rescales as $\sqrt{-g}=\Omega^{-4}\sqrt{-\tilde{g}}$. This yields the action,

$$S=\int d^4x\sqrt{-\tilde{g}}\big[\frac{M_p^2}{2}\big(\tilde{R}+6\tilde{\nabla}^2\omega-6\tilde{g}^{\mu\nu}\partial_\mu\omega\partial_\nu\omega\big)-\Phi^{-4}U(\Phi)\big]+S_m, \tag{2.15}$$

The term $6\tilde{\nabla}^2\omega$ can be integrated out and does not contribute to the EOM, therefore we drop it. We now introduce a new field $\phi=\sqrt{6}M_p\omega$ and potential,

$$V(\phi)=\frac{M_p}{2}\frac{\Phi R-f(R)}{\Phi^2}, \tag{2.16}$$

allowing us to write,

$$S=\int d^4x\sqrt{-\tilde{g}}\big[\frac{M_p^2}{2}\tilde{R}-\frac{1}{2}\tilde{g}^{\mu\nu}\partial_\mu\phi\partial_\nu\phi-V(\phi)\big]+S_m. \tag{2.17}$$

Therefore we see that whenever the conformal transformation can be performed, the gravitational sector of $f(R)$ theories are equivalent to Einstein gravity minimally coupled

[1] From now on we will employ the notation that tilded objects are constructed from the rescaled metric $\tilde{g}$.

[2] Note that $\tilde{g}_{\mu\nu}$ is only well defined if Ω is strictly positive, the case in which it is not will be of importance to Chapter 2.

to a scalar field. This also shows that the act of promoting $R \to f(R)$ simply introduced a new scalar degree of freedom, which also turns out to be healthy. This duality can be quite useful and one can choose to study the theory using the action in either form: in certain cases, keeping the $f(R)$ term explicit is easier while in others it is beneficial to deal with ϕ, $\tilde{R}$. We call the Jordan frame the situation in which the Ricci scalar is multiplied by some function of the scalar field, which is the case for the $f(R)$ form of the action here. On the other hand, the frame obtained by disentangling the coupling between the scalar field and the Ricci scalar in the way we've just done is called the Einstein frame. Note that we have not discussed the effect of this transformation on the matter action S_m. In the Jordan frame, the matter is minimally coupled to the metric. However upon going to the Einstein frame the matter is generally not only coupled to the new graviton $\tilde{g}_{\mu\nu}$ but also to the scalar field ϕ. In the special case that S_m enjoys a conformal symmetry, the scalar field's presence is not felt by the matter content.

As was already mentioned earlier, the EH action is the unique Lagrangian for a massless spin-2 field in 3+1 dimensions. Our discussion so far was concerned about modification of the R term in the EH action which is the term governing the graviton's dispersion relations when expanded around a background (read kinetic and gradient terms). These types of modification kept the action invariant under diffeomorphism. However if we are willing to forgo this gauge symmetry, we can introduce a mass term for the graviton and in doing so introduce 3 new dof (for a total of 5 dof which is expected of a massive spin 2 particle). The idea of massive gravity dates back to Fierz and Pauli [42] who tried to simply add the following linear mass term to the perturbed EH action,

$$\mathscr{L}_{FP} = \frac{-1}{8} m^2 (h_{\mu\nu} h^{\mu\nu} - (h^{\mu}_{\mu})^2). \tag{2.18}$$

However this theory does not reduce to *GR* in the limit that the mass vanishes. This behavior is known as the van Dam-Veltman-Zakharov (vDVZ) discontinuity [43] and is a symptom of neglecting the non-linearities in Eq. (2.18). It was eventually shown [44] that

a non-linear treatment could indeed tame the discontinuity and hopefully produce a theory that reduced to GR in the correct limit, but the efforts were tainted by the seemingly unavoidable introduction of a sixth ghostlike DOF named the Boulware-Deser ghost [45]. It is not until 2010 that de Rham, Gabadadze and Tolley [47] identified five combinations of terms (three of them non-linear) from which a massive gravity action could be built and not be plagued by the BD ghost issue. The gravitational theory constructed out of these terms is known as dRGT massive gravity and we refer the interested reader to the following in depth reviews [18, 19] for additional details. The paper [2], co-written by the author of this thesis, studies the cosmological solutions in dRGT massive gravity when the kinetic term is also replaced by an arbitrary f(R) function.

CHAPTER 3

NEW EXOTIC SOLUTIONS IN PURE R^2 GRAVITY

Recently, an exploration of the vacuum solutions of pure R^2 gravity uncovered new black hole solutions, resulting, in part, from the lack of a generalized Birkhoff theorem [20]. As a theory, quadratic gravity has some interesting features: it possesses scale invariance and with the addition of the Weyl curvature tensor $C^2 = C_{\mu\nu\rho\sigma}C^{\mu\nu\rho\sigma}$, is renormalizable [10]. Numerically it has been shown that the most general quadratic gravitational action, $R^2 - \alpha C^2$ for some constant α, also admits new black hole solutions [21]. Pure R^2 gravity is the only pure quadratic gravity that is ghost free [14, 22] and, as an example of an $f(R)$ theory, is sometimes dual to the Einstein-Hilbert action of General Relativity (GR) minimally coupled to a scalar field. We've introduced this duality in Chapter 1 and here we shall discuss the cases where the duality fails in section 3.1. It is precisely in this regime that the new black hole solutions of [20] were found. The authors interpreted these solutions as a part of the strong coupling limit of GR.

In Einstein's theory of General Relativity, every metric $g_{\mu\nu}$, is a solution to Einstein's equations for some associated stress energy tensor $T_{\mu\nu}$. It is therefore a challenging task to determine which solutions should be considered physical solutions. This dilemma lead to the development of *ad hoc* energy conditions intended to reasonably restrict properties of the sourcing matter. The weakest such condition, the Null Energy Condition (NEC), stipulates that the stress energy tensor of matter should satisfy $T_{\mu\nu}k^\mu k^\nu \geq 0$ for any arbitrary null vector k^μ. Imposing such conditions prohibits the construction of many spacetimes in the context of GR, including traversable wormholes [23] [3]. Wormholes have appeared in many science fiction settings, recently giving rise to additional research on the subject [24]. Besides a means of rapid interstellar travel used by advanced civilizations, wormholes are

[3] See Appendix 5.5 for details

discussed in the quest to understand the relation between entanglement and the possible emergence of spacetime [25]. Such ideas were applied to the information paradox, yielding the so called, $ER = EPR$ conjecture [26], which suggests that entangled particles are connected via a (non-traversable) Einstein-Rosen bridge. Likewise, it has long been speculated that quantum gravity may somehow resolve singularities in black hole spacetimes leading some researchers to the idea that the Universe itself, might have been created on the interior of a black hole (for some early work see [27, 29, 30, 33, 32, 28, 34, 35, 31, 36, 37]).

In this chapter, we show that the vacuum space of R^2 gravity permits new traversable wormhole and non-singular black hole solutions. We emphasize that these structures are supported only by the vacuum and do not require any unusual states of matter. In section 3.1 we discuss how such spacetimes are possible and present our solutions in section 3.2. We then show explicitly in section 3.3 that observers and light rays can traverse the throat of the wormhole and discuss some of the trajectory's properties in section 3.4. Finally, we discuss the appearance of the wormhole to asymptotic observers in section 3.5.

3.1 R^2 Gravity and Its Vacuum Structure

The R^2 gravity action is a specific example of the more general $f(R)$ action that was introduced in Chapter 1,

$$S = \frac{M_p^2}{2}\int d^4x\sqrt{-g}f(R) + S_m. \tag{3.1}$$

When the matter action S_m exhibits conformal symmetry and $F(R) = df/dR$ is non-vanishing, it is well known that this action is equivalent to Einstein gravity minimally coupled to a scalar field. This is shown by writing the action in terms of the metric $\tilde{g}_{\mu\nu} = \Omega^2 g_{\mu\nu}$, where the conformal factor is given by $\Omega = F(R)^{1/2}$. Therefore, any solutions found in such $f(R)$ theories will also be found in Einstein gravity coupled to a scalar field. However, as was shown in [20], this is not necessarily the case when $F(R)$ vanishes, and the metric $\tilde{g}_{\mu\nu}$, is

ill defined.

In $f(R)$ gravity the metric $g_{\mu\nu}$ has equation of motion,

$$F(R)R_{\mu\nu} - \frac{1}{2}f(R)g_{\mu\nu} - \nabla_\mu\nabla_\nu F(R) + g_{\mu\nu}\Box F(R) = M_p^{-2}T_{\mu\nu}. \tag{3.2}$$

In the above, $T_{\mu\nu}$ is the stress-energy tensor of any external matter present.[4] Focusing on vacuum solutions, $T_{\mu\nu} = 0$, we notice that any metric producing $f(R) = F(R) = 0$ will be a solution of this theory. These conditions may constraint R but leave significant freedom in the form of the Ricci tensor $R_{\mu\nu}$.

Focusing on the simplest case which satisfies the above criteria, $f(R) = R^2$, we find that every spacetime with traceless Ricci tensor is a solution to the R^2 gravity EOM. This abundant freedom in the form of $R_{\mu\nu}$ is how Birkhoff's theorem is circumvented. In standard Einstein gravity, $R = 0$ implies $R_{\mu\nu} \propto T_{\mu\nu}$ and therefore any metric sourced by matter with traceless energy-momentum tensor will also be a solution to the vacuum of R^2 gravity. One notable example is the electromagnetic field with $\mathscr{L}_m = -\frac{1}{4}F_{\mu\nu}F^{\mu\nu}$. We will show that this new freedom found in the vacuum of R^2 gravity allows bundles of ingoing modes to evolve from converging to diverging modes in section 3.4. In ordinary Einstein gravity, such evolution would only be possible through a violation of the NEC as can be shown through the Raychaudhuri equation–an equation which describes the evolution of the bundle's divergence θ. For null geodesics with tangent null vector k^μ, the Raychaudhuri equation is

$$\frac{\mathrm{d}}{\mathrm{d}\lambda}\theta = -\frac{1}{2}\theta^2 - \sigma_{\mu\nu}\sigma^{\mu\nu} + \omega_{\mu\nu}\omega^{\mu\nu} - R_{\mu\nu}k^\mu k^\nu. \tag{3.3}$$

Here $\sigma_{\mu\nu}$ is the shear tensor and $\omega_{\mu\nu}$ the vorticity tensor. The vorticity can always be set to zero by choosing a coordinate system in which the congruences are hypersurface

[4] We use the reduced Planck mass, $M_p^2 = 1/8\pi G_N$, metric signature $(-,+,+,+)$, and $\Box \equiv \nabla^\mu\nabla_\mu$.

orthogonal. The remaining terms on the RHS are all negative in GR if the NEC is satisfied ($R_{\mu\nu}k^\mu k^\nu = M_P^{-2}T_{\mu\nu}k^\mu k^\nu \geq 0$). This implies that $\frac{\mathrm{d}}{\mathrm{d}\lambda}\theta < 0$ and hence bundles of null geodesics are always converging. In R^2 gravity, vacuum solutions can have $R_{\mu\nu}k^\mu k^\nu > 0$ so that the above conclusion need not apply.

3.2 Non-Singular Black Holes and a Traversable Wormhole

The most general static and spherically symmetric spacetime is given by

$$ds^2 = -f_1(r)dt^2 + f_2(r)dr^2 + r^2 d\Omega^2, \tag{3.4}$$

where $\mathrm{d}\Omega^2 = \mathrm{d}\theta^2 + \sin^2\theta\,\mathrm{d}\phi^2$. We make the following metric ansatz

$$f_1(r) = G(r) \quad \text{and,} \quad f_2(r) = \frac{r^2}{r^2 - k^2}\frac{1}{G(r)}. \tag{3.5}$$

Introducing a reparametrization of the radial coordinate, $l^2 = r^2 - k^2$, for some constant k, the metric becomes,

$$\mathrm{d}s^2 = -G(l)\mathrm{d}t^2 + \frac{1}{G(l)}\mathrm{d}l^2 + (l^2 + k^2)\mathrm{d}\Omega^2. \tag{3.6}$$

If $G(l) \to 1$ as $l \to \pm\infty$, this metric connects two asymptotically Minkowski spacetimes. The constant k will set the minimal wormhole throat radius as r cannot become smaller than this value.

The Ricci scalar of this spacetime is given (in terms of G) by,

$$\begin{aligned} -\frac{1}{2}(k^2+l^2)^2 R = \frac{1}{2}\Big((k^2+l^2)^2 G'\Big)' \\ +(k^2+l^2)(G-1) + Gk^2\,, \end{aligned} \tag{3.7}$$

where $' \equiv d/dl$. Requiring $R = 0$, yields a two parameter solution for G. A complicated exact solution of this second order ODE is given in Appendix 3.7. For our purposes we need

only discuss certain limiting behaviors. Taking the large l limit of Eq.(3.7), corresponding to large r, and solving the $R = 0$ ODE, we find the asymptotic solution,

$$G(l \to \pm\infty) \simeq 1 - \frac{2M_\pm}{l} + \frac{Q_\pm^2}{l^2}. \tag{3.8}$$

This resembles a Reissner–Nordström metric of mass $M_\pm$ and charge $Q_\pm$. The mass and charge need not be the same for the two different asymptotic regions. Hence we label them by a $\pm$ to denote the values measured by observers located at $l \to \pm\infty$. These parameters arises as integration constants and should not be associated with a conserved mass and charge even though we employ the nomenclature. For example, the approximate solution in equation (3.8) drops a non-analytic term, seen only in the large l limit of the exact solution, that goes as $k^2 \frac{\log(l/k)}{l^2}$. Hence $Q_\pm^2$, taken as the coefficient of the $1/l^2$ term in the series expansion, cannot be a well defined finite charge. We will discuss this point further in section 3.5.

At small l, the solution is approximately,

$$G(l \approx 0) \simeq \frac{1}{2}\left[1 + 2(G_0 - 0.5)\cos(2l/k) + k v_0 \sin(2l/k)\right] \tag{3.9}$$

where $G_0 = G(0)$ and $v_0 = G'(0)$ are the initial conditions determining the shape of the throat. The mass $M_\pm$ and charge $Q_\pm$ are expressed in terms of these parameters in section 3.5. Given appropriate choices of $G_0,\ v_0$, we ensure that G is strictly positive for all l. The solutions are shown in figure (3.1). In these cases the spacetime has no horizons even though it appears as a charged black hole to asymptotic observers.

For certain initial conditions our solutions can develop horizons, however the solutions remain free of singularities. To the asymptotic observer these solutions appear as non-singular black holes (or one-way traversable wormholes). In general there can be up to two regions where the $l = const$ slices become spacelike, whenever G becomes negative. This can be seen by noting that for $|l/k| > 1$ the ODE is similar to an overdamped oscillator with equilibrium at $G = 1$ and therefore any zero crossings must occur in the range

$l \in [-k,k]$. As $\mathcal{O}(1)$ changes in G occur on a length scale $l \sim k$, we expect G to oscillate at most once during this interval, possibly below zero, and then it will asymptote monotonically to its equilibrium value. This may occur on either side of the $l = 0$ point and there are at most two regions where G is negative. Penrose diagrams show the causal structures of the three spacetimes discussed above in Figure 3.2. In the remainder of this work we focus on the cases with no horizons, where G remains well behaved so that the $\{t, l, \theta, \phi\}$ coordinate system covers the entire spacetime manifold. In other words we will assume that G is a continuous non vanishing function of l that asymptotes to 1 as $l \to \pm\infty$.

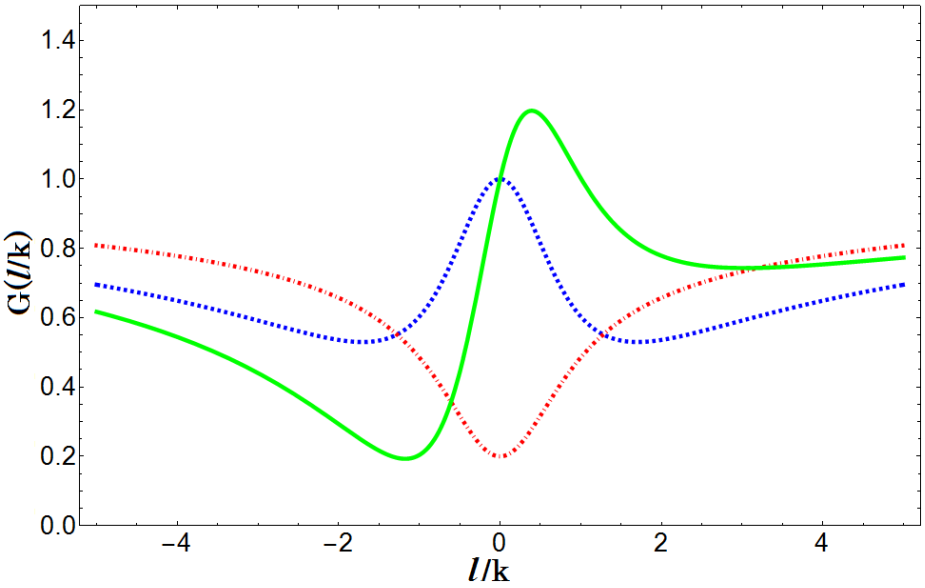

Figure 3.1: Plot of $G(l/k)$ vs l/k. The blue/dashed, red/dotted-dashed, and green/solid have initial conditions (G_0, v_0) set as $(1,0)$, $(0.2,0)$, and $(1,1/k)$ respectively.

3.3 Geodesics of Timelike and Null Observer

Here we compute the paths of null and timelike geodesics traveling in the radial direction ($d\Omega = 0$). We show that a timelike observer can, in principle, safely traverse the wormhole. We begin with a discussion of null geodesic which have $ds^2 = 0$ and are therefore parametrized by,

$$\frac{dl}{dt} = \pm G. \tag{3.10}$$

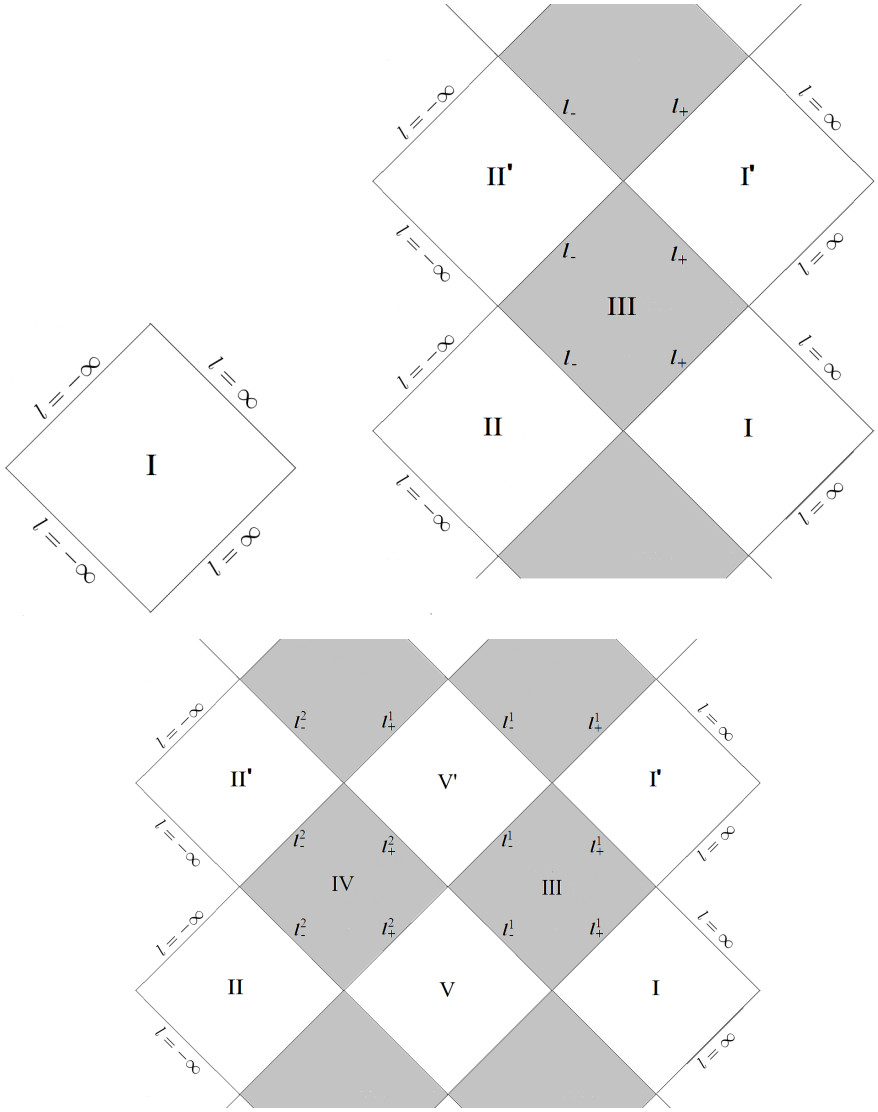

Figure 3.2: Penrose diagrams of the three possible causal structure found in the vacuum solutions of ansatz (3.6). The shaded regions have $G < 0$ and the $l = const$ slices are spacelike. **Top:** G is well behaved and no horizons exist. **Middle:** G is negative in a single region between $l \in [l_-, l_+]$. **Bottom:** G is negative in two regions between $l \in [l_-^1, l_+^1]$ and $l \in [l_-^2, l_+^2]$.

Assuming no horizons, this may be integrated to find the path $l(t)$ of radially propagating photons. In section 3.4 we shall see that the affine parameter defined by $dt/d\lambda = cG^{-1}$ for some arbitrary constant c is a monotonic boundless function of t. Hence the light rays trajectory through the throat can be described in a finite range of the affine parameter.

We now turn to timelike geodesics. Given a four velocity $u^\alpha(\tau)$ with τ being the observer's proper time the geodesic equation reads,

$$u^\alpha \nabla_\alpha u^\beta = 0. \tag{3.11}$$

The normalization of $\mathbf{u}$ for radial trajectories gives the following condition,

$$\left(\frac{dt}{d\tau}\right)^2 = \frac{1}{G^2}\left(\frac{dl}{d\tau}\right)^2 + \frac{1}{G}. \tag{3.12}$$

Eliminating $u^0 = dt/d\tau$ from the l component of the geodesic equation, one can solve for $l(\tau)$ through,

$$\frac{\mathrm{d}^2}{\mathrm{d}\tau^2} l = -\frac{G'}{2}, \tag{3.13}$$

and $t(\tau)$ is determined from Eq.(3.12). To visualize the geodesic motion, we embed the geometry in a higher dimensional space. Suppressing the θ coordinate and taking a time slice at a particular t (which looks the same for any choice of t), we embed the wormhole in a 3D space as shown in figure (3.3a). This particular solution corresponds to a $G_0 = 1$ and $v_0 = 0$ wormhole. The red line represents the radial trajectory of a timelike observer. We also show how different values of $G_0,\ v_0$ (defined and color coded in the caption of figure (3.1)) affect our courageous explorer along his journey.

Note that the solutions can have regions where gravity is attractive or repulsive towards $l = 0$. The transition occurs wherever G' switches sign. For instance, our solutions with $G_0 = 1$ have repulsive gravitational forces near the throat and incoming observers must possess sufficient velocity to traverse the throat. In figure (3.3b), our infalling explorer labelled by the solid green curve does not have sufficient speed and is repelled out of

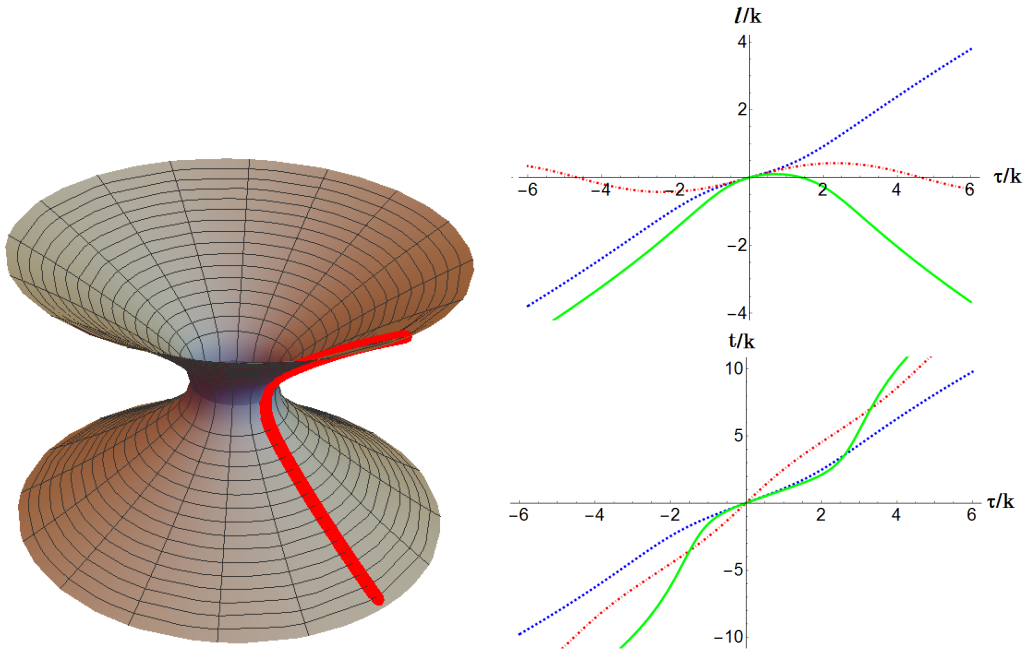

(a) Embedding of the wormhole in higher dimensions with a throat–traversing, radial trajectory traced in red. We have suppressed the θ coordinate such that every circle at some constant z is a sphere having that circle's radius.

(b) The coordinates l and t as seen by observers with identical initial speeds at $l = 0$ and attempting to cross the different throats. The observer on the green geodesic fails to traverse the wormhole and is spit back out. The observer labelled by the red dot-dashed line oscillates around the everywhere–attractive wormhole. The blue dashed observer successfully passes through the throat.

Figure 3.3: Wormhole structure.

the wormhole. However, the solution with $G_0 = 0.2$ is attractive everywhere towards the wormhole and the observer travelling in this background (designated by the red dot-dashed line in figure (3.3b)) oscillates back and forth through the wormhole. It is even easy to find solutions where G asymptotically relaxes back to 1 from above. In these cases our asymptotic observers would associate a negative mass to the wormhole and feel a repulsive force from it! This might be concerning at first sight as this definition of mass corresponds to energy in standard GR. However the situation is more complicated in R^2 gravity as we will discuss in section 3.5.

3.4 Tidal Forces Through the Wormhole

In this section we determine how bundles of geodesics evolve as they pass through the wormhole. The non-zero components of the Ricci tensor read,

$$R_{tt} = \frac{1}{2}G\Big(\frac{2lG'}{k^2+l^2} + G''\Big), \tag{3.14}$$

$$R_{rr} = -(2G)^{-1}\Big(\frac{4k^2G + 2l(k^2+l^2)G'}{(k^2+l^2)^2} + G''\Big), \tag{3.15}$$

$$R_{\theta\theta} = 1 - G - lG', \quad R_{\phi\phi} = \sin(\theta)^2 R_{\theta\theta}. \tag{3.16}$$

Taking the radial geodesics with affine parameter λ, $\mathbf{k} = \frac{\partial t}{\partial \lambda}(1, \pm G, 0, 0)$ for in(-) and out-going(+) geodesics respectively, we find

$$R_{\mu\nu}k^\mu k^\nu = -\Big(\frac{\partial t}{\partial \lambda}\Big)^2 \frac{2k^2G^2}{(k^2+l^2)^2}. \tag{3.17}$$

This is strictly negative and therefore can allow for $\frac{\mathrm{d}}{\mathrm{d}\lambda}\theta > 0$. We now compute the divergence explicitly. The divergence of a bundle of geodesics with tangent vectors k^μ is given by $\theta = \nabla_\alpha k^\alpha = \frac{1}{\sqrt{-g}}\partial_\alpha(\sqrt{-g}k^\alpha)$. To determine $k^t = \frac{\partial t}{\partial \lambda}$ one must look at the geodesic equation for the null ray. The k^t equation is,

$$k^t \frac{d}{dt}k^t + k^l \frac{d}{dl}k^t + \Gamma^t_{\alpha\beta}k^\alpha k^\beta = 0, \tag{3.18}$$

$$\implies \quad \frac{d}{dl}k^t + \frac{G'}{G}k^t = 0\,, \tag{3.19}$$

where in the second line we assumed $\frac{d}{dt}k^t = 0$, appropriate for a time independent metric. This is solved by $k^t = cG^{-1}$ for some integration constant c which denotes the arbitrary choice in the affine parameter's normalization. We take the value $c = 1$. In the cases were G is well behaved so that our coordinate system is valid everywhere, we can compute θ for any l,

$$\theta = \pm\Big(\frac{2l}{l^2+k^2}\Big). \tag{3.20}$$

The $\pm$ corresponds to in and outgoing modes respectively. As expected, θ switches sign when the light rays cross the throat at $l = 0$. Moreover, since θ gives the expansion/contraction of the cross sectional area of a bundle of light rays (it is an area, as orthogonal hypersurfaces to null geodesics are two dimensional), the radial null geodesics of the metric in Eq. (3.6) are not affected by the form of G.

A timelike observer will also feel increasingly squeezed by the tidal forces as we enters the wormhole. Unlike for null geodesics, such observers will be sensitive to G. Morris & Thorne [23] used these tidal forces to impose constraints on the wormhole spacetime by requiring that a human sized observer feels less than a g of force. We avoid imposing any such conditions here but give a brief derivation of the tidal forces below. We refer the reader to [23] for additional details.

Consider an observer $\mathscr{O}'$ at rest with respect to $\{l, \theta, \phi\}$, and proper reference frame with basis vectors,

$$\begin{aligned} \mathbf{e}_{\hat{t}} &= \frac{1}{\sqrt{G}}\mathbf{e}_t,\ \mathbf{e}_{\hat{l}} = \sqrt{G}\mathbf{e}_l, \\ \mathbf{e}_{\hat{\theta}} &= \frac{1}{\sqrt{k^2+l^2}}\mathbf{e}_\theta,\ \mathbf{e}_{\hat{\phi}} = \frac{1}{\sin\theta\sqrt{k^2+l^2}}\mathbf{e}_\phi. \end{aligned} \tag{3.21}$$

In this coordinate system the metric takes the simple form $\eta_{\hat{\alpha}\hat{\beta}} = (-1,1,1,1)$. A second observer $\mathscr{O}''$ located at the same point, but moving with a speed v in the radial direction, will also have his own reference frame whose basis can be written in terms of the coordinates of $\mathscr{O}'$ through a Lorentz boost, leaving $\eta_{\hat{\alpha}\hat{\beta}}$ unchanged,

$$\begin{aligned} \mathbf{e}_{\hat{0}} &= \gamma\mathbf{e}_{\hat{t}} \mp \gamma v\mathbf{e}_{\hat{l}}, \\ \mathbf{e}_{\hat{1}} &= \gamma v\mathbf{e}_{\hat{t}} \mp \gamma\mathbf{e}_{\hat{l}}, \\ \mathbf{e}_{\hat{2}} &= \mathbf{e}_{\hat{\theta}},\ \mathbf{e}_{\hat{3}} = \mathbf{e}_{\hat{\phi}}. \end{aligned} \tag{3.22}$$

Here the gamma factor is the usual $\gamma = (1-v^2)^{-1/2}$. In this frame the moving observer has four velocity $\tilde{\mathbf{u}} = \mathbf{e}_{\hat{0}}$. Since the four acceleration $\mathbf{a}$ is perpendicular to the four velocity, our

radially moving observer's acceleration will only have a non zero radial component in his own reference frame. In the $\{t, l, \theta, \phi\}$ coordinates one can compute $a_t = \tilde{u}^\alpha \nabla_\alpha \tilde{u}_t$ which is related to the acceleration a felt by the observer $\mathscr{O}''$ through $a_t = \mathbf{a} \cdot \mathbf{e}_t = a\mathbf{e}_{\hat{1}} \cdot \mathbf{e}_t$. We find,

$$a = -\frac{1}{\sqrt{G}}\Big[\gamma\frac{G'}{2} + G\frac{\partial\gamma}{\partial l}\Big]. \tag{3.23}$$

At $l \to \pm\infty$ and assuming $\gamma \approx 1$, the acceleration felt is $a \approx -M_\pm/l^2$. For $l \approx 0$, the term G' contains terms evolving as G_0/k and v_0. Hence one may tune these values so that the observer crossing the throat will feel a desired acceleration.

The tidal acceleration felt by the observer $\mathscr{O}''$ can also be computed in his reference frame. The relative acceleration of two nearby points separated by $\xi = (0, \vec{\xi})$ as measured by $\mathscr{O}''$ is given by,

$$\Delta a^{\hat{j}} = -R^{\hat{j}}_{\hat{\alpha}\hat{\beta}\hat{\rho}} u^{\hat{\alpha}} \xi^{\hat{\beta}} u^{\hat{\rho}} = -R_{\hat{j}\hat{0}\hat{k}\hat{0}} \xi^{\hat{k}}, \tag{3.24}$$

with,

$$\begin{aligned} R_{\hat{1}\hat{0}\hat{1}\hat{0}} &= -\frac{G''}{2}, \quad R_{\hat{2}\hat{0}\hat{2}\hat{0}} = R_{\hat{3}\hat{0}\hat{3}\hat{0}}, \\ R_{\hat{3}\hat{0}\hat{3}\hat{0}} &= \gamma^2 \frac{lG'}{l^2+k^2} - \gamma^2 v^2 \Big(\frac{l(l^2+k^2)G' + 2k^2 G}{2(l^2+k^2)^2}\Big). \end{aligned} \tag{3.25}$$

We can explicitly see how the size of the throat k influences the strength at which our traveler is squeezed in the angular directions.

3.5 The Wormhole to Asymptotic Observers

Following observers through the wormhole we see there is a lack of parity symmetry in the l component when $v_0 \neq 0$. Observers in different asymptotic regions view the wormhole with a mass $M_\pm$ and charge $Q_\pm$ where the $\pm$ designating the parameters measured by observers at $l = \pm\infty$. These are determined by $G_0,\ v_0$ from the exact solution of G and by picking out the asymptotic coefficients. Defining $u = 1/l$, we expand the solution of G around $u = 0$ and define,

$$M_{\pm} = \lim_{u\to\pm 0} \frac{-1}{2}\frac{\mathrm{d}}{\mathrm{d}u}G(u, G_0, v_0), \tag{3.26}$$

$$Q^2_{\pm} = \lim_{u\to\pm 0} \frac{\mathrm{d}^2}{\mathrm{d}u^2}G(u, G_0, v_0). \tag{3.27}$$

One finds that the mass is,

$$\frac{-2M_{\pm}}{k} = -2\frac{M_0}{k} + \cos(\sqrt{3}\pi/2)G_0 \pm \frac{\sin(\sqrt{3}\pi/2)}{\sqrt{3}}kv_0 \tag{3.28}$$

with $M_0 \approx 0.7$ being a number whose exact expression is given in section (3.7). The $\pm$ sign in front of v_0 reflects how the properties of the wormhole differ to each asymptotic observer. Even though this implies that asymptotic observers will feel different accelerations toward the wormhole, one cannot gain energy by going from one region to the other. The asymmetrical shape of the throat (as is seen by the solid green curve in Fig.3.1) will prohibit this as can be shown by Eq.(3.13) which implies $(dl/d\tau)^2 + G$ is a conserved quantity and so $\Delta v = [dl/d\tau]_{l=\pm\infty} = 0$.

The coefficent $Q^2_{\pm}$ is found to be,

$$\frac{Q^2_{\pm}}{k^2} = \frac{Q^2_0}{k^2} \pm \sqrt{3}\sin(\sqrt{3}\pi/2)G_0 - \cos(\sqrt{3}\pi/2)kv_0 - 2\log(u\mathrm{k}). \tag{3.29}$$

The very last term has a logarithmic dependence so that, not only is $Q^2_{\pm}$ not a constant, it diverges as $u \to 0$. In the case of GR with electromagnetism, the conserved charge of a Reissner–Nordström spacetime is defined by the conserved current $j^{\mu} = \frac{1}{4\pi}\nabla_{\nu}F^{\mu\nu}$ integrated over a spacelike hypersurface. Here no such analogue electromagnetic field is present. The logarithm found is just a feature of our particular wormhole solution. Choosing a different ansatz, such as simply replacing the angular part of Eq. (3.6) by,

$$g_{\Omega}\mathrm{d}\Omega^2 = \left(l^2 + \frac{k^2}{l^2+k^2}\right)\mathrm{d}\Omega^2, \tag{3.30}$$

allows us to obtain wormhole solutions that asymptotically approach the Reissner–Nordström metric without logarithmic contribution.

Conserved charges are tightly linked with symmetries of the theory. In our case, we have a timelike killing vector $\mathbf{e}_t = \frac{\partial}{\partial t}$ with which we can construct a conserved current and find the corresponding charge; however, the interpretation of charges in R^2 gravity is tricky. Previous attempts [38, 39] by Deser & Tekin, to define an energy for higher curvature gravity in analogy with GR have shown that every asymptotically flat solution of R^2 gravity has vanishing energy. An alternative definition was proposed by the same authors and relied instead on the corresponding Poisson equation of higher curvature gravity [40]. In terms of this second definition, the leading term of the source in the Poisson equation defines the energy and allows for a less degenerate classification of spacetimes but still yields a vanishing energy for solutions with everywhere vanishing Ricci scalar. Therefore even though an asymptotic observer will feel that the wormhole is exerting a gravitational force (just as if it were a spherical object of mass $M_{\pm}$ in ordinary GR) he shouldn't associate this value with a conserved charge such as the energy. Hence one might wonder if these quantities can evolve upon the introduction of small perturbations.

3.6 Final Remarks

In this chapter we have presented new static wormhole and (non-singular) black hole solutions found in the vacuum of R^2 gravity. Of particular interest are the perfectly healthy wormhole solutions supported without any NEC violating matter. Their existence could prove important as it is argued in [20] that the new $R = 0$ solutions might be part of the strong coupling limit ($M_p \to 0$) of General Relativity. It would be interesting to study the role of such spacetimes in this limit using other tools. For instance it was shown recently that in the context of AdS/CFT, the strong subadditivity condition of entanglement entropy

imposes constraints on the bulk geometry of certain spacetimes [41]. One would require a dual CFT to asymptotically $R = 0$ solutions to apply similar results.

In the context of our particular solution, we have shown that asymptotic observers view the wormhole as a Reissner–Nordström black hole with "mass" $M_{\pm}$ and "charge" $Q_{\pm}$. We have stressed that one should not be associating these values as conserved charge. They are taken as coefficients of the $1/r$ and $1/r^2$ terms in the metric expansion and do not correspond to some conserved quantity as was the case in GR. This raises the question of whether $M_{\pm}$ and $Q_{\pm}$, along with the whole wormhole itself, are dynamical once small perturbations are introduced. It would also be interesting to look for further exotic solutions to general $f(R)$ theories which cannot be captured by Einstein gravity coupled to a scalar field.

3.7 Explicit Form of the Asymptotic Coefficients of G

The general solution to G is given by

$$\begin{aligned}
G(l) = 1 &+ \frac{k\cos\left(\sqrt{3}\arctan(l/k)\right)}{\sqrt{k^2+l^2}}G_0 + \frac{k\sin\left(\sqrt{3}\arctan(l/k)\right)}{\sqrt{3}\sqrt{k^2+l^2}}kv_0 \\
&- \frac{k}{6\sqrt{k^2+l^2}}\Big[\sqrt{3}\big(H_{-\frac{1}{4}(1+\sqrt{3})} - H_{\frac{1}{4}(-5+\sqrt{3})} - 2 - \sqrt{3} + \pi\tan\left((1+\sqrt{3})\pi/4\right)\big)e^{i\sqrt{3}\arctan(l/k)} \\
&\qquad + \big(\sqrt{3}H_{\frac{1}{4}(-3+\sqrt{3})} - \sqrt{3}H_{\frac{1}{4}(-1+\sqrt{3})} + 3\big)e^{-i\sqrt{3}\arctan(l/k)}\Big] \\
&- \frac{2k}{(3+\sqrt{3})(k-il)}\Big[(2+\sqrt{3})\,{}_2F_1\big(1,\frac{1}{2}(1-\sqrt{3});\frac{1}{2}(3-\sqrt{3});1-\frac{2k}{k-il}\big) \\
&\qquad + {}_2F_1\big(1,\frac{1}{2}(1+\sqrt{3});\frac{1}{2}(3+\sqrt{3});1-\frac{2k}{k-il}\big)\Big]. \quad (3.31)
\end{aligned}$$

Here ${}_2F_1(a,b;c;z)$ is the ordinary hypergeometric function. The mass $M_\pm$ and charge $Q_\pm$ can be read as the coefficients of the series expansion of G at large l as written in Eq. (3.26, 3.27). The result is,

$$\begin{aligned}
\frac{-2M_\pm}{k} =& \cos(\sqrt{3}\pi/2)G_0 \pm \frac{\sin(\sqrt{3}\pi/2)}{\sqrt{3}}kv_0 \\
&+ \frac{1}{2\sqrt{3}}\cos(\sqrt{3}\pi/2)\big[-H_{-\frac{1}{4}(1+\sqrt{3})} + 2H_{\frac{1}{4}(-5+\sqrt{3})} - H_{-\frac{1}{4}(3-\sqrt{3})} \\
&+ 2\sqrt{3} + 4 - \pi\tan\left((1+\sqrt{3})\pi/4\right)\big], \quad (3.32) \\
\frac{Q^2}{k^2} =& \pm\sqrt{3}\sin(\sqrt{3}\pi/2)G_0 - \cos(\sqrt{3}\pi/2)kv_0 \\
&+ \frac{1}{2}\sin(\sqrt{3}\pi/2)\big[-H_{-\frac{1}{4}(1+\sqrt{3})} + 2H_{\frac{1}{4}(-5+\sqrt{3})} - H_{-\frac{1}{4}(3-\sqrt{3})} \\
&\qquad + 2\sqrt{3} + 4 - \pi\tan\left((1+\sqrt{3})\pi/4\right)\big] \\
&- 2\log(2u\mathrm{k}) - 2(1-\gamma_{E-M}) - \psi^{(0)}\left((1-\sqrt{3})/2\right) - \psi^{(0)}\left((1+\sqrt{3})/2\right) \\
& \quad (3.33)
\end{aligned}$$

Here γ_{E-M} is the Euler-Mascheroni constant. The functions H_n and $\psi^{(0)}(z)$ are Harmonic numbers and polygamma functions respectively, both are defined from the Gamma function

through,

$$H_n = \gamma_{E-M} + \frac{\Gamma'(n+1)}{\Gamma(n+1)}, \tag{3.34}$$

$$\psi^{(0)}(z) = \Gamma'(z)/\Gamma(z). \tag{3.35}$$

CHAPTER 4

A COMPARISON BETWEEN INFLATION AND THE MATTER BOUNCE

In this section, we give a comparison between two models of the very early Universe: Inflation and the Matter Bounce. We first review the standard picture of Big Bang Cosmology and comment on its peculiar features. This leads us to explore how these can be explained through the two models. Inflation has been proposed around 1980 and has since found strong support from nearly every cosmologist. Nevertheless, determining exactly what occurred in the early Universe is a hard task. Testing out the scenario is difficult as it involves physics at energies far beyond which can be probed and hence any evidence comes from cosmological measurements of the late universe. This has motivated the search to determine if there could be other alternatives and it eventually lead to the development of the Matter bounce.

4.1 Big Bang Cosmology

The Big Bang picture is based on the assumption of a universe which is spatially homogeneous and isotropic on very large scales. A universe with these features is easily described in general relativity by considering the most general metric obeying those symmetries,

$$ds^2 = -dt^2 + a(t)^2 d\mathbf{x}^2 = -dt^2 + a(t)^2 \Big[\frac{dx^2}{1-kx^2} + x^2 d\Omega^2 \Big]. \tag{4.1}$$

where $d\Omega^2 = d\theta^2 + \sin^2\theta d\phi^2$, and $k \in \{0, 1, -1\}$ is a dimensionless value representing the curvature of the universe. The metric (4.1) is known as the Friedmann-Lemaitre-Robertson-Walker (FLRW) metric. The scale factor a sets the distance between objects on a constant t hypersurface at fixed comoving positions. As observations constrains our universe to have little curvature [58], we will assume a flat case ($k = 0$) in the rest of this manuscript in order

to simplify the equations.

It is also important to discuss the matter content as it determines the behavior of the metric (4.1). We approximate matter by a perfect fluid and spatial homogeneity and isotropy then restricts the stress-energy tensor to be of the form,

$$T^{\mu}_{\nu} = diag(-\rho, p, p, p). \tag{4.2}$$

We can obtain a dynamical equation of this fluid by employing the conservation of the stress-energy tensor $\nabla_{\mu} T^{\mu\nu} = 0$. Its $\nu = 0$ component yields the continuity equation,

$$\dot{\rho} + 3\left(\frac{\dot{a}}{a}\right)(\rho + p) = 0. \tag{4.3}$$

The Einstein equations characterizes the dynamics of the metric and its relation to the energy and matter densities, $G_{\mu\nu} = \frac{1}{M_p^2} T_{\mu\nu}$ where $M_p^2 = (8\pi G)^{-1}$ is the reduced Planck mass. Using the metric ansatz of Eq. (4.1), the 00 component and the trace of the Einstein equations give rise to what are known as the two Friedmann equations,

$$\left(\frac{\dot{a}}{a}\right)^2 = \frac{1}{3M_p^2}\rho \tag{4.4}$$

$$\left(\frac{\ddot{a}}{a}\right) = -\frac{1}{6M_p^2}(\rho + 3p). \tag{4.5}$$

Once an equation of state (EoS) for matter is specified, usually of the form $w\rho = p$ with w constant. One can use the Friedmann equations to obtain an explicit expression for $a(t)$. Whichever fluid dominates the energy density will determine the dynamics in the evolution of $a(t)$. For instance, a fluid with $w = 1/3, 0 or -1$ corresponds to a radiation (r), non-relativistic matter (m) or vacuum energy (Λ) dominated universe respectively. Note that we label a gas of relativistic particles as radiation since its equation of state has $w = 1/3$, when we speak of "matter" we shall specifically refer to the kind that has an equation of state satisfying $w = 0$ which would be obeyed by a non-relativistic gas. Combining the EoS

with equations 4.3 and 4.4 we find for the specific examples,

$$\begin{aligned} a(t) &\propto t^{1/2} \quad \text{for radiation } (r), \\ a(t) &\propto t^{2/3} \quad \text{for matter } (m), \\ a(t) &\propto e^{Ht} \quad \text{for vacuum/dark energy } (\Lambda), \\ a(t) &\propto a^{\frac{2}{3(1+w)}} \quad \text{for a general } w. \end{aligned} \tag{4.6}$$

Here we defined the Hubble parameter as $H = \frac{\dot{a}}{a}$. Its inverse, $1/H$, sets the Hubble time and radius which are the characteristic time and distance scales of the Universe's description. By defining $\rho_c = 3M_p^2 H_0^2$ and $\Omega_i = \rho_i/\rho_c$ one rewrites the Friedmann equation 4.4 in a form that makes the dominant energy density of the universe apparent,

$$\frac{H(t)}{H_0} = \left[\frac{\Omega_m}{a^3} + \Omega_\Lambda + \frac{\Omega_r}{a^4}\right]^{1/2} \tag{4.7}$$

with $H_0 \approx 67.27 \pm 0.66 \text{km} \cdot \text{s}^{-1} \cdot \text{Mpc}^{-1}$, $\Omega_m = \Omega_b + \Omega_{dm}$, $\Omega_{dm}h^2 \approx 0.1198 \pm 0.0015$, $\Omega_b h^2 = 0.02225 \pm 0.00016$ and $h = H_0/(100\text{km} \cdot \text{s}^{-1} \cdot \text{Mpc}^{-1})$ [58] are the Planck's measured present day value of each quantity after choosing the normalization scale $a(t_0) = 1$. The quantity $\Omega_r h^2 \approx 10^{-5}$ can be obtained from today's neutrino/photon density based on the CMB temperature while $\Omega_\Lambda h^2 \approx 0.3$ balances out Eq. (4.7). Written in this form, the Friedmann equation makes it easy to determine the matter type which dominates at different epochs. It is now obvious that an expanding universe will eventually be dominated by the non zero Ω_Λ.

As the time coordinate t is somewhat arbitrary, it is important to find a physical way to measure the time elapsed. Consider the wavelength λ of some photon. This quantity will be affected by the evolution of the scale factor, getting stretched(squeezed) by the expansion(contraction) of the universe as $\lambda(t) = \frac{a}{a(t_*)}\lambda(t_*)$ for some reference time t_*. In the Standard Model the scale factor is monotonically increasing. Therefore in this case, a photon's wavelength allows us to determine how long ago and how far away a photon was

emitted, provided we know its original value. This leads to the concept of redshift. Let t_0 be the current age of the universe, the redshift z is defined as,

$$1 + z(t) = \frac{a(t_0)}{a(t)} = \frac{1}{a(t)}, \tag{4.8}$$

where in the second equality we have set that $a(t_0) = 1$. The Cosmic Microwave Background (CMB) was emitted when the temperature dropped below ~ 3000 Kelvin through hydrogen recombination. The detection of the CMB light today allows us determine that the redshift of recombination must have been $z_{rec} \simeq 1100$. Another important time was when matter overtook radiation as the dominant contributor to the energy density budget. This transition occurred at a redshift of $z_{eq} \approx 3300$ which is named the redshift at matter-radiation energy density equality. It was only around redshift $z \sim 1$ that the dark energy became a very important contributor to the energy density.

4.2 Success and Failures of the Standard Model

The description offered by the Standard Model of Big Bang Cosmology (BBC) has gathered a great amount of success (see [59, 60] for a more detailed review). By assuming a young universe that was hot, dense, isotropic and homogeneous up to tiny scale invariant fluctuations, the Big Bang theory was able to predict the following observations,

- The abundance of elements through Big Bang Nucleosynthesis (BBN)
- The CMB and various of its statistical properties
- The formation and distribution of the Large Scale Structure (LSS)
- Hubble's Law

However over the past few decades, many observations have been left unanswered by the theory. To name a few,

- Baryon Asymmetry
- What is dark energy and dark matter?
- The Big Bang Singularity
- Monopole Problem
- Horizon Problem
- Flatness Problem
- Initial Inhomogeneities

It is possible that some of these problems will be solved without having recourse to extensions of the BBC. For example, the nature of the baryon asymmetry and the dark sector properties are likely to be resolved from theories beyond the standard model (of particle physics). This statement is based on the fact that the current zoo of cosmological scenarios seems unsuited to produce new phenomenology that can address these two questions; for example one must work really hard to tie inflation with dark matter. This is in contrast to the 5 other problems of which we will review here.

- The Singularity Problem

  A well known issue with the Big Bang Cosmology is that it offers no explanation regarding what occurs at the ”Big Bang”. As the scale factor is a monotonically increasing function of t, the past seems to have originated from a region where $a = 0$ in which physical quantities become divergent. Of course this just shows that the description outlined by the Big Bang theory is not adequate to tackle this epoch, but then what kind of extensions could offer answers? Possibilities have been put forward by invoking exotic matter and/or modification of GR, but it is possible one will require

an understanding of quantum gravity to discuss this apparent singularity. Nevertheless, the issue forces us to conjure some initial state at some finite $a > 0$. With such freedom, the problems faced by the BBC can all be resolved through fine tuning these initial conditions. In practice, one would desire more satisfactory resolutions that are somewhat independent of the initial state.

- Monopole Problem

  In the 1970s a lot of attention was placed on finding a Grand Unified Theory (GUT). The efforts attempted to find a group with a single coupling constants from which the Standard model of particle physics would emerge after symmetry breaking. A very common feature of these models was the existence of monopoles: very heavy stable topological defects that were created during the GUT symmetry breaking epoch. The view offered by the Big Bang theory had trouble with this picture. The reason was tied to the decreasing temperature in an expanding universe of relativistic matter ($T \sim 1/a$). At early times we expect the GUT symmetry to be intact as the temperatures are high, however the expansion will eventually force T to drop below the GUT scale - triggering symmetry breaking - a proliferation of GUT monopoles should therefore have been created. Being very heavy, their energy density dilutes as pressureless matter and hence quickly dominates the energy budget shown in Eq. (4.7). Observations suggest otherwise, it shows matter only overtook radiation at a redshift of $z \approx 3300$.

  So where are the monopoles? A possible resolution comes from arguing that they simply do not exist. However many theoretical considerations (not only GUTs) that are beyond the scope of this work strongly suggest their inevitability. We will introduce in section 4.3 some examples of cosmological scenarios which allows the Big Bang picture and the existence of monopoles to coexist.

- Horizon Problem

The CMB shows that the universe was nearly homogeneous and correlated on very large scales. However a quick calculation shows that these correlation scales are larger than what would seem possible by causality. The comoving particle horizon is defined as the maximum distance a particle could travel in a given time,

$$\ell(t_1,t_2) = \int_{t_1}^{t_2} \frac{\mathrm{d}t}{a(t)} = \int_{a_1}^{a_2} \frac{\mathrm{d}(\ln a)}{aH}. \tag{4.9}$$

We see a homogeneous CMB over distances of $\ell(t_{rec},t_0)$, with t_{rec},t_0 being the time of recombination and today respectively. This is to be compared to $\ell(0,t_{rec})$ which gives the size of the causal regions at recombination. The issue comes when one uses today's value of the energy budget and works backwards with the forms of $a(t)$ given in Eq. (4.6), we find that $\ell(t_{rec},t_0) \gg \ell(0,t_{rec})$. Hence it seems that the CMB has correlations beyond what is causally acceptable. The main culprit of this result is the comoving Hubble radius, $(aH)^{-1}$, which is monotonically decreasing when radiation or matter is the dominating form of energy. Note that we've also glossed over the fact that one integral runs all the day down to $t = 0$ which is likely beyond the regime of validity of our assumptions. The resolutions explored in this document will use this fact to justify changing the picture at early times.

- Flatness Problem

  In the introduction we've decided to set $k = 0$ as this was consistent with observations. However why would the Universe be so flat? A flat universe is unstable. It is easy to see this instability by considering the continuity equation (4.3) with the EOS $p = w\rho$ and the Friedmann equation with non-zero k,

$$H^2 - \frac{k}{a^2} = \frac{1}{3M_p^2}\rho. \tag{4.10}$$

  Defining a time dependent critical density $\rho_c = 3M_p^2H^2$ we look at the quantity $\Omega = \rho/\rho_c$, satisfying $1-\Omega = -k/(aH)^2$. In terms of these variables, the continuity

equation turns into,

$$\frac{d\Omega}{d\ \ln a} = (1+3w)\Omega(\Omega-1)$$

and so assuming $w > -1/3$ as suggested by the BBC, $\Omega > 1$ implies $\frac{d\Omega}{d\ \ln a} > 0$ while $\Omega < 1$ implies $\frac{d\Omega}{d\ \ln a} < 0$. Therefore $\Omega = 1$, corresponding to $k = 0$, is an unstable fixed point. The universe must have started out incredibly flat ($\frac{\rho-\rho_c}{\rho_c} \sim 10^{-50}$ at $T = 10^{15}$ GeV) in order to account for the current observations of the lack of any curvature. The flatness problem deals with trying to justify this fine tuned initial condition.

- Initial Inhomogeneities

  The last problem we will discuss is the origin of the inhomogeneities. The CMB is not perfectly homogeneous, its temperature maps show fluctuations of one part per 10^5. These originated from perturbations of the energy density which initially possessed a nearly scale invariant spectrum. Those seeds were also responsible for the formation of structure. How did these perturbations appear?

4.3 Beyond Big Bang Cosmology

In this section we introduce two cosmological scenarios and discuss what they bring to the resolutions of the BBC problems outlined above. The first scenario we shall review is the theory of cosmological inflation. This paradigm is by far the most famous and almost universally taken as the correct extension to the standard model of cosmology. However probing the inflationary epoch can be quite challenging and finding unambiguous support of its existence could prove impossible, hence one might wonder if there are other possibilities. This motivated some researchers to devote some of their time to finding alternatives, one of these being bouncing cosmologies and more precisely the matter bounce. This scenario will be our second paradigm to be reviewed.

4.3.1 Cosmological Inflation

Cosmological inflation refers to an epoch at very early time where the universe underwent a rapid expansion. More precisely, inflation requires that the comoving Hubble scale decreases with time, $\frac{d}{dt}(aH)^{-1} < 0$. This places restrictions on the type of energy that dominates, a fluid with EOS w will have a Hubble radius evolving as

$$(aH)^{-1} \sim t^{\frac{1}{3(1+w)}(1+3w)}, \tag{4.11}$$

therefore inflation will take place whenever $w < -1/3$ is satisfied.[5] The usual descriptions of matter and radiation obviously do not have the right requirement to drive an accelerated expansion. However we would be naive to expect matter to behave as a perfect fluid at the very high energy where the inflationary epoch occurs. Seeking guidance from the current state of the art tools to study high energy physics, namely Quantum Field Theory (QFT), we turn our attention to fields. Interestingly a simple scalar field allows us to obtain an inflationary phase.

Consider the matter action,

$$S_m = \int d^4x\sqrt{-g}(L)_\phi = \int d^4x\sqrt{-g}\big(\frac{1}{2}\partial_\mu\phi\partial^\mu\phi - V(\phi)\big), \tag{4.12}$$

Using a flat FLRW metric, we find the EOM for a homogeneous ϕ to be,

$$\ddot{\phi} + 3H\dot{\phi} + \frac{\partial V}{\partial\phi} = 0. \tag{4.13}$$

While the stress-energy tensor,

$$T_{\mu\nu} = 2\frac{\delta\mathscr{L}_\phi}{\delta g^{\mu\nu}} + g_{\mu\nu}\mathscr{L}_\phi, \tag{4.14}$$

[5] We will restrict ourselves to the $w \geq -1$ case, see [61] for discussions considering $w < -1$.

has the form $T_{\mu\nu} = \text{diag}(\rho, p, p, p)$ with,

$$\rho = \frac{1}{2}\dot{\phi} + V(\phi) \tag{4.15}$$

$$p = \frac{1}{2}\dot{\phi} - V(\phi). \tag{4.16}$$

The EoS $w = p/\rho$ can be as close to -1 as one wants by specifying a situation where $V(\phi) \gg \dot{\phi}^2$. This condition is called the slow-roll condition. If satisfied and $w \approx -1$ we are in regime where the Hubble parameter is mainly fixed by the potential $H^2 = V(\phi)/(3M_p^2)$ and as ϕ varies slowly, we can approximate H as constant on short timescales. This puts us in a (quasi) de Sitter geometry as the scale factor will now grow as $a(t) \sim \mathrm{e}^{Ht}$. The slow-roll parameter $\varepsilon = -\frac{\dot{H}}{H^2}$ characterizes the deviation from a de Sitter phase. In order for $\dot{\phi}$ to stay small and therefore have a sustained period of inflation, it is important that

$$|\ddot{\phi}| \ll |3H\dot{\phi}| + |V_{,\phi}| \tag{4.17}$$

which leads to a second condition on the so called η-parameter,

$$\eta = -\frac{\ddot{\phi}}{H\dot{\phi}} \ll 1. \tag{4.18}$$

A specific realization of inflation is easily obtained with $V(\phi) = \frac{1}{2}m^2\phi^2$. Whenever $\phi \gg \phi_e \simeq M_p$, the slow-roll conditions are satisfied and can be shown to be approximatively,

$$\varepsilon(\phi) \simeq \eta(\phi) \simeq 2\left(\frac{M_p}{\phi}\right)^2 \ll 1. \tag{4.19}$$

So how does inflation solve the BBC problems?

- The Singularity Problem

  Unfortunately this problem is still present. Although the exponential form of the scale factor seems to allow for $t \to -\infty$ and not cause any divergence, this is simply a coordinate artifact. One can show that caustics develops at finite proper time in the past of any geodesics, a feature that arises in all scenarios with which the average

expansion rate in the past satisfies $H_{avg} > 0$ [62]. Therefore inflation still requires one to input initial conditions by hand. However these do not have to be homogeneous over seemingly acausal scales. If our scalar field starts high enough on its potential Eq. (4.4) insures that the expansion will quickly redshift away any gradient energy density. However as potential energy does not get diluted by the expansion of space it creates a region with a near homogeneous ϕ that seeds an inflationary phase.

- Monopole Problem

  This issue was the motivation that drove Alan Guth to develop one of the first prototypes of inflation. The original idea discussed the supercooling of the Universe, it accomplished that by trapping the scalar field in a false vacuum and thereby obeying all the slow roll conditions. If GUT monopoles were only created before this event, they would then be diluted away at an exponential pace and rendered very rare.

- Horizon Problem

  As stated previously, the Horizon problem came about because the Hubble radius $(aH)^{-1}$ was an increasing function of time in BBC. This is obviously not the case when a is exponentially increasing and H is constant. Moreover we can now push our time variable to $-\infty$. Therefore now one should be considering $\ell(t_i, t_{rec}) = \ell(t_i, t_e) + \ell(t_e, t_{rec})$ with $t_i,\ t_e$ the time at the start and end of inflation respectively. Looking at $\ell(-t_i, t_e)$,

  $$\ell(t_i, t_e) = \int_{t_i}^{t_e} \frac{dt}{a_0 \mathrm{e}^{Ht}} = \frac{1}{a_0 H}(\mathrm{e}^{-Ht_i} - \mathrm{e}^{Ht_e}) \tag{4.20}$$

  can be made arbitrary large by having an arbitrary long period of inflation.

- Flatness Problem

  We saw previously that $\Omega = 1$ was an unstable fixed point in BBC. This is in contrast to inflation in which it is an attractor. As $aH \sim He^{Ht}$ is now exponentially increasing, an inflationary period drives Ω towards unity because $1 - \Omega = -k/(aH)^2$. In terms of

efolding number $N = \int_{t_i}^{t_e} H dt = \ln(a_{end}/a_{start})$, inflation must last for about $N \sim 40-60$ to solve the flatness and horizon problems. The exact efolding number depends on the reheating mechanism, but we defer the interested reader to the review [60] on inflationary cosmology for these additional details.

- Initial Inhomogeneities

  Likely the most impressive feat of the inflationary scenario is its ability to give an elegant explanation to the existence of the initial density perturbations. As the Universe grows exponentially, all energy gets redshifted away except for the vacuum energy supplied by the potential $V(\phi)$. This energy is eventually dumped into radiation by a process known as reheating. However quantum mechanics forbid us to know the exact value of ϕ. Studying the vacuum fluctuations of the field $\delta\phi(\vec{x},t) = \phi(\vec{x},t) - \phi_0(t)$ for some $\phi_0(t)$ being the background value, we find that these evolve to a nearly scale invariant spectrum on large scales which is exactly what is measured by the CMB. The near scale invariance of these fluctuations are a consequence of being in a quasi de Sitter background geometry. We will explore these details in section 4.4 when outlining the mathematical framework of cosmological perturbations.

Inflation is a beautiful explanation to many mysteries facing the BBC. However it does have its issues such as the singularity problem. In recent years, new bounds on the tensor-to-scalar ratio r have been set by BICEP/Keck Array [63] which improves on their previous joint analysis with Planck [64] and now bounds $r < 0.07$ at 95% CL at a pivot scale of $k = 0.05\text{Mpc}^{-1}$. Such bounds are hard to obtain from models in which the scalar field takes super planckian values. The simplest large field models such as our $V = m^2\phi^2$ example are excluded or under heavy stress. From an Effective Field Theory (EFT) point of view, these models were already questionable, however the small field models require some big fine tuning to generate inflationary epochs that last long enough to tackle the

problems it intended to solve. If the trend continues and the acceptable inflation models get too complex, one might start to seriously question the whole paradigm and look for potential alternatives.

4.3.2 Bouncing Cosmologies and the Matter Bounce

Amongst these alternatives are bouncing scenarios. Bouncing cosmologies assumes that the Universe was originally contracting and underwent a bounce to set the stage for its current expanding phase. We will focus on one specific realization of the bounce, one dubbed the Matter Bounce. Unfortunately, in similar fashion than what occurred with inflation, simple models of the Matter Bounce have been ruled out. This does not make them a very attractive contender at the moment. Nevertheless the scenario approaches the BBC problems in interesting ways and so is worth exploring. We introduce it in two parts, the first will survey the contracting phase while the second will deal with the bounce event.

Let us first discuss the contracting phase. The beginning of the bounce scenario assumes a large contracting universe. The physics is still described by the Friedmann equation which we present once more but with additional explicit energy components on the right hand side.

$$3M_p^2H^2 = \frac{\rho_\Lambda^*}{a^0} + \frac{\rho_m^*}{a^3} + \frac{\rho_r^*}{a^4} + \frac{\rho_a^*}{a^6} + \frac{\rho_\phi^*}{a^{3(w+1)}} + ..., \tag{4.21}$$

with ρ^* being the energy density of each component when $a = 1$, which we will fix to be the scale factor at the present time. The components that we chose to list in Eq. (4.21) are: a cosmological constant, matter, radiation, the anisotropy, and a scalar field ϕ with an EoS of w respectively. We see that as the scale factor gets progressively smaller, energy densities with larger EoS tends to eventually drive the Hubble expansion for a period of time. When discussing the creation of the energy density fluctuations in section 4.4 it will become clear

that the different epochs will tend to produce perturbations with different spectrum. As the name suggest, the Matter Bounce scenario assumes that the fluctuations seen in the CMB were created (or frozen out) during the period of matter contraction. The motivation is that it is in this epoch that a massless scalar field's vacuum fluctuations will acquire a scale-invariant spectrum.

A major obstacle in any bouncing universe is the anisotropy problem which leads to a so called Mixmaster universe [65]. If one breaks the isotropy symmetry of the FLRW metric we can write,

$$ds^2 = -dt^2 + a^2 \sum_i \mathrm{e}^{\beta_i} dx^i, \tag{4.22}$$

with the β_i characterizing the anisotropy and obey $\sum_i \beta_i = 0$. Rederiving the corresponding FLRW equation shows that these fields enters as having an energy density who scales as a^{-6}. This scaling implies that, in a contracting phase, anisotropy will eventually dominate over all the form of known energy listed in Eq. 4.21. The universe becomes increasingly anisotropic and the dynamics of the β's become controlled by the potential shown in fig 4.1. Misner showed [65] that this potential creates a chaotic behavior and causes one to lose track of the background evolution. The common way to bypass this problem is to postulate the existence of a stiff fluid with $w \gg 1$. Such an EoS insures that the fluid eventually dominates over anisotropies. This has the effect of driving the β's to a constant value as one approaches the bounce, thus evading the chaotic behavior and driving the universe towards an isotropic state [66]. The epoch driven by the stiff fluid is known as an Ekpyrotic phase and is the only relevant pre-bounce epoch in the *Ekpyrotic scenario* [67] which was first introduced as an alternative to inflation.

We are now ready to takle the bounce phase. The condition $H = 0$ must hold at the bounce point if the Einstein equations are still valid. This requires a fluid whose en-

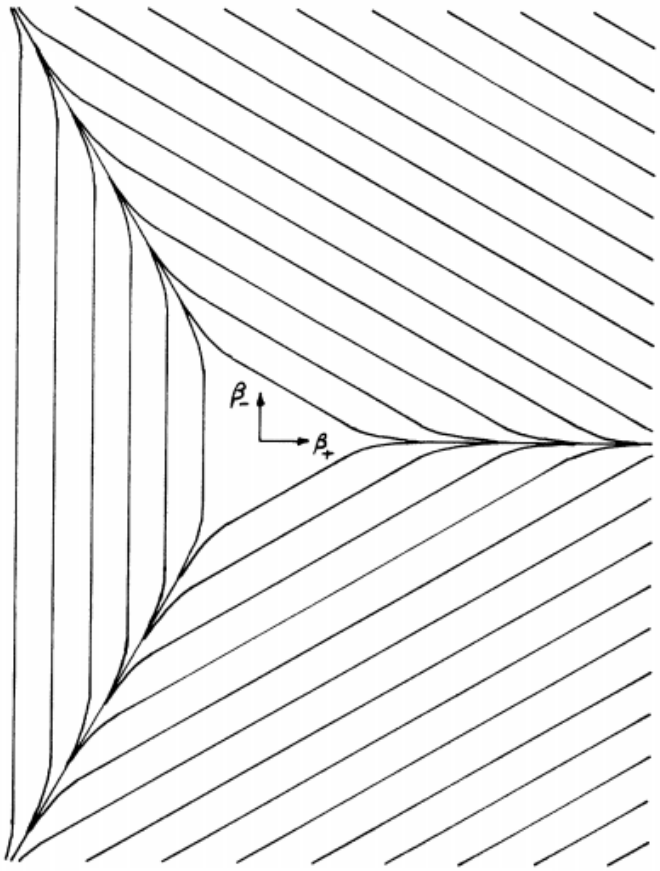

Figure 4.1: Equipotential lines of the effective potential $V(\beta)$, taken from [65]. The fields are $\beta_+ = \beta_1 + \beta_2$ and $\beta_- = \frac{1}{\sqrt{3}}(\beta_1 - \beta_2)$.

ergy density is effectively negative in order to cancel the large contribution from the other components we've been discussing. Such scenarios are called non-singular bounces as it evades singularity theorems. These give us the opportunity to track every instance of the bounce analytically (see [68]& [69] for examples). On the other hand, singular bounces invoke unknown quantum gravity effects that are said to resolve the timelike singularity. If these quantum gravity effect occurs for a very short time, one then treats the bounce phase as a singular surface and then attempt to

(ambiguously) apply matching conditions to follow the evolution across the bounce. Notable recent development in [71] introduces some machinery which allows them to tracks the classical paths of perturbations in the complex plane and subsequently argue that this of-

fers a rigorous way to compute the behavior of the perturbations through a singular bounce. For more details on the bounce phase and for explicit examples, the interested reader is encouraged to consult the review [72].

Here is how the contracting phase helps in explaining some of the mysteries of BBC.

- Singularity Problem

  Unlike in the inflationary case, the Universe starts in a region with $H < 0$ but ends up in a region with $H > 0$. Therefore this evades the condition outlined in [62]. However new ideas needs to be introduced in order for the Hubble parameter to switch signs. This is quite hard to achieve and involves violating the Null Energy Condition (NEC) in the context of GR. There has been debates on whether this is possible without introducing pathologies [73, 74, 70].

- Monopole Problem

  Monopole creation occurs when the Universe's temperature drops below a certain threshold that force some symmetry to spontaneously break. In a bouncing scenario, the Universe does not have to contract indefinitely. A bounce can occur at a finite scale factor, insuring that the temperature never reaches high enough value to restore the symmetry that, once rebroken, would generate monopoles.

- Horizon Problem

  In a way similar to what inflation enables us to do, the contraction phase allow the initial time t_1 of the integral $\ell(t_1,t_2) = \int_{t_1}^{t_2} \frac{\mathrm{d}t}{a(t)}$ to be pushed to negative values. This allow us to go around the argument we've previously encountered.

  A nice cartoon that summarizes the horizon problem is shown in fig (4.2). A length scale $\lambda(t) = a(t)\lambda_0$ is inside the Hubble radius if it is smaller than H^{-1}. The horizon problem deals with the fact that modes enters the Hubble radius today implies correlations that couldn't have been set by causal physics in the BBC. Inflation solves

this by stretching these modes beyond H^{-1} while bouncing cosmologies shrinks H^{-1} below $\lambda(t)$.

- Flatness Problem

  The peculiarity regarding the Universe's flatness does not get completely answered in bouncing scenarios. However the problem is not as stout as in BBC. Being in some way the reverse situation than the expanding phase, the contracting phase has a flat universe as an attractor. Hence during contraction Ω approaches unity. Therefore a small initial flatness is not necessarily a fine tuned parameter in this model. Nevertheless this initial small flatness obtained from the contraction is undone just as quickly in the expanding phase.

- Initial Homogeneities To explain the density perturbations that we observe today, bouncing scenarios also rely on vacuum fluctuations. Unfortunately they do not possess any glaring symmetries that justifies the appearance of a scale-invariant spectrum. We will discuss this detail in this next section.

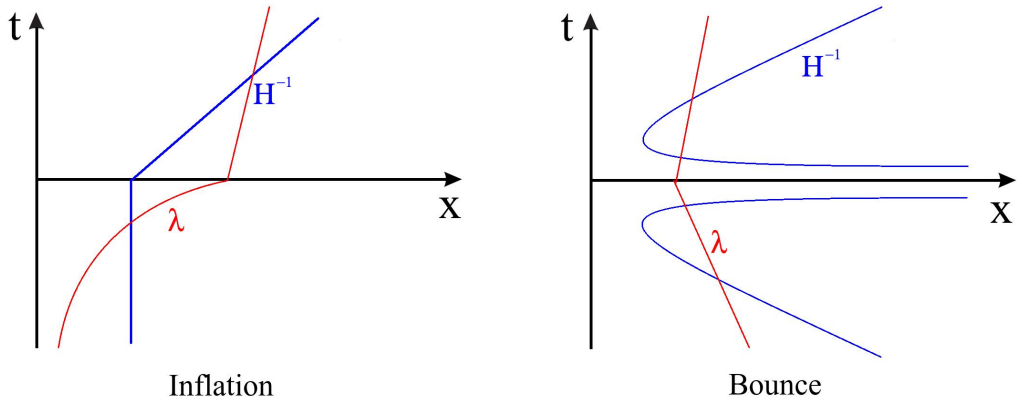

Figure 4.2: Cartoon of the Inflationary and (non-singular) Bounce resolutions of the horizon problem. A region of length λ initially starts inside the Hubble radius but eventually becomes larger. The $x-axis$ delimits the end of inflation or the bounce point. The Hubble radius must diverge for a short period of time in a non-singular bounce as it requires $H=0$ at the bounce point.

4.4 Cosmological Perturbations

Computing the predicted initial inhomogeneities of each scenario will require us to analyze their perturbations. Doing so forces us to chose a more specific realization of each paradigm. We will assume that a scalar field exists in both cases and is ultimately responsible for the inhomogeneities, to be more exact the field needs to eventually dump its energy density into radiation and hence imprint the statistical properties of its perturbations unto the primordial plasma. Note that the background in a Matter Bounce scenario can be driven by typical matter, hence the inclusion of the scalar field is an extra ingredient that is required. This scenario produces the inhomogeneities by what is called *isocurvature* fluctuations. The name comes from the fact that they are fluctuation in variables which cannot be absorbed by a time translation as they are "orthogonal" to the background evolution. These must seed energy density fluctuations in the primordial plasma through detailed mechanisms that are beyond the basic scope of this review [6]. In inflation, the scalar field's position is responsible for the cosmological expansion and so perturbations in ϕ can easily be transfered to density fluctuations in the primordial plasma through reheating [75].

We denote by ϕ the scalar field present in each scenario and assume its dynamics are described by the action,

$$S_\phi = \int d^4x\sqrt{-g}\big(\frac{1}{2}\partial_\mu\phi\,\partial^\mu\phi - V(\phi)\big). \tag{4.23}$$

We can expand this to second order in perturbations to read off the EOM for $\delta\phi = \phi - \phi_0$. For our purposes we will use a rescaled field $u = a\delta\phi$ to simplifies the EOM. In Fourier space and with conformal time ($' = \mathrm{d}/\mathrm{d}\tau$ with $\mathrm{d}\tau = \mathrm{d}t/a$) we find [77],

[6] Using precisely, we are referring to mechanisms seeding an adiabatic mode from an entropic one.

$$\left(u_k\right)'' + \left(k^2 - \frac{a''}{a} + a^2 V_{,\phi\phi}\right) u_k = 0. \tag{4.24}$$

In the inflationary (de Sitter) case, $a \sim \mathrm{e}^{Ht} \sim \frac{1}{H\tau}$ which gives $a''/a \sim 2/\tau^2$. On the other hand, a Matter contraction has $a \sim (-t)^{2/3}$ with t negative and increasing towards 0 (the bounce point). In conformal time we then have, $a \sim \tau^2$ which also yields $a''/a \sim 2/\tau^2$. One immediately notices that the EOM term involving the scale factor ends up being equal for either an inflationary phase or a matter contraction. This is an example of Wands' duality, Wands showed that for every expanding background there existed a corresponding contracting one in which a scalar field had the same dynamics [78]. The duality is one of the main reason that the Matter Bounce has gathered interest.

To further solve the EOM, we will assume the potential term can be neglected, this is done by considering a massless scalar field in the Matter Bounce case, and impose that $a^2 V_{,\phi\phi} \ll k^2$ on the inflationary potential.

With these assumptions the EOM is solved by the two solutions,

$$u_k = \frac{A}{\sqrt{2k}} \mathrm{e}^{-ik\tau}\left(1 - \frac{1}{k\tau}\right) + \frac{B}{\sqrt{2k}} \mathrm{e}^{ik\tau}\left(1 + \frac{1}{k\tau}\right). \tag{4.25}$$

We will have to chose an initial condition, this is done by requiring that the fluctuations start off in their quantum vacuum. At very early time, when $k\tau \gg 1$, the modes are much smaller than the Hubble radius and therefore evolves as if they were in Minkowski space. Imposing such Minkowski vacuum state,

$$\lim_{\tau \to -\infty} u_k = \frac{1}{\sqrt{2k}} \mathrm{e}^{-ik\tau}, \tag{4.26}$$

picks out the $A = 1,\ B = 0$ solution. In inflation, one can also justify this choice by picking the vacuum which is invariant under de Sitter isometries, this is known as the Bunch-Davies vacuum (see [79]). At late time when $\tau k \ll 1$ the modes effectively becomes "frozen" as the solutions stop having oscillatory behavior and start behaving as if it were a background

mode with $k = 0$. Its relative amplitude when compared to a second mode k' is therefore set at Hubble crossing and hence so are the statistical properties of these perturbations.

We can now compute the power spectrum of ϕ ([75, 76]),

$$P_k^{(\phi)} = \frac{4\pi k^3}{(2\pi)^3}\left|\delta\phi_k\right|^2 = \frac{4\pi k^3}{(2\pi)^3}\left|\frac{u_k}{a}\right|^2 \approx \begin{cases} \left(\frac{H}{2\pi}\right)^2, & \text{Inflation} \\ \left(\frac{1}{4\pi a(\tau)\tau}\right)^2, & \text{Matter Bounce.} \end{cases} \tag{4.27}$$

We took the large scale limit in the final equality, showing that the scalar field eventually acquires a scale invariant power spectrum in either cases. However there exist a glaring difference between the two computed quantities, unlike for the matter bounce, the inflationary power spectrum is time independent. This difference in behavior can be traced to the zero mode of each quantities[7]. In inflation, one has slow-roll and $\dot{\phi} \simeq 0$ to first order, while in the matter bounce our massless field has an EoS of $w = 1$ and evolves as $\phi \simeq a^{-3}$.

The departure from scale invariance is characterized by the spectral index n_s defined by,

$$n_s - 1 = \frac{\mathrm{d}\ln P}{\mathrm{d}\ln k}. \tag{4.28}$$

A scale invariant spectrum has $n_s = 1$ and hence a P that is independent of k. CMB measurements from Planck shows that the initial conditions of BBC had to possess a nearly scale invariant power spectrum with $n_s = 0.968 \pm 0.006$ [58]. We say the power spectrum has a red tilt as larger wavelength possesses more power. Inflationary models naturally give rise to such departure when one takes into account slow roll corrections which we've so far neglected. The matter bounce does not have this luxury and more complexity must be added to obtain a red tilt, for instance a bounce model with interacting dark energy and dark matter would work and such model is introduced in the next Chapter.

[7]The perturbations dynamic is the same as the background on super Hubble scales. This is essentially because the effective local background in each scenario changes with time as $\phi_0^{new} = \phi_0 + \sum_{k|k>(aH)} \delta\phi_k$, see [80]

The overall amplitude of these perturbations can be related to the value of the Hubble constant and the slow-roll parameters in simple single field inflationary models. When multiple fields are present, such as in the curvaton mechanism (for inflation) and our example of a Matter Bounce, this parameter becomes dependent on the mechanism responsible for transferring the isocurvature fluctuations unto the energy density of the primordial plasma.

4.5 Summary

The inflationary scenario enjoys tremendous successes without any glaring problems, hence attempts to find simple alternatives has been the focus of only a small portion of cosmologists. Nevertheless the question is a cheap but important one to investigate. Failure will further solidify our confidence in the paradigm offered by inflation, but a success would yield a big overhaul of the current topics discussed in early universe cosmology. Bouncing scenarios have been one of the most popular contenders, but they still require a lot of work to elucidate their many details. However, as new data piles up, recent acceptable bounce models seem to be increasing in complexity at a faster rate than the inflationary ones. It might be that this alternative is simply not adequate, or that we don't understand all of its ramifications yet. The future could hold surprises.

CHAPTER 5

SEARCHING FOR A MATTER BOUNCE COSMOLOGY WITH LOW REDSHIFT OBSERVATIONS

The Matter Bounce scenario allows for a sizable parameter space where cosmological fluctuations originally exit the Hubble radius when the background energy density was small. In this scenario and its extended versions, the low energy degrees of freedom are likely responsible for the statistical properties of the cosmic microwave background (CMB) power spectrum at large length scales. An interesting consequence is that these modes might be observable only at relatively late times. Therefore low redshift observations could provide evidence for, or even falsify, various bouncing models. We provide an example where a recently hinted potential deviation from Λ-Cold-Dark-Matter (ΛCDM) cosmology results from a dark matter (DM) and dark energy (DE) interaction. The same interaction allows Matter Bounce models to generate a red tilt for the primordial curvature perturbations in corroboration with CMB experiments.

5.1 Introduction

The recently released CMB data from the Planck collaboration has constrained the value of the spectral index to be $n_s = 0.968 \pm 0.006$ [58], verifying at high precision a nearly scale invariant power spectrum of primordial curvature perturbation with a slightly red tilt. These properties are naturally achieved in inflationary cosmology where a nearly scale invariant power spectrum is associated with an almost constant Hubble scale during inflation as described by cosmological perturbation theory [81]. Despite the many successes of the inflationary universe paradigm, recent precision observations are beginning to statistically disfavor many of the simplest (polynomial field potential) models (see, e.g. Planck [58], and BICEP2/Keck Array [63]). In light of the latest observations it is worthwhile to continue to

search for potential alternative theories of the early universe. The study and interpretation of primordial cosmological perturbation theory may also be performed in alternative early universe paradigms, such as bouncing cosmology [82, 83, 72], ekpyrotic cosmology [67, 84], the pre-big bang model [85, 86], and string gas cosmology [87, 88, 89]. Amongst some of these scenarios, it was pointed out in [78, 90] that a massless scalar field will acquire a scale invariant power spectrum when its vacuum fluctuations are allowed to exit the Hubble radius during a matter-like (background equation-of-state parameter $w = 0$) contracting phase.

The aforementioned scenario, known as *matter bounce* cosmology, has been extensively studied in the literature. A challenge matter bounce cosmology has to address is whether the scale invariant primordial power spectrum can survive the bouncing phase. This issue has been studied in several models, for example, the quintom bounce [91, 92], the Lee-Wick bounce [93], the Horava-Lifshitz gravity bounce [94, 95, 96], the $f(T)$ teleparallel bounce [97, 98, 99], the ghost condensate bounce [100], the Galileon bounce [101, 68], the matter-ekpyrotic bounce [69, 102, 103], the fermionic bounce [104, 105], etc. (see, e.g. [106, 76] for recent reviews). It was found in general, that on length scales larger than the time scale of the nonsingular bounce phase, both the amplitude and the shape of the power spectrum remain unchanged through the bounce due to a no-go theorem [107, 141].

In addition, successful models of a nonsingular bounce must satisfy various observational constraint from CMB measurements. In particular, successful models must yield a red tilted spectral index, as well as satisfy observational non-gaussianity constraints [108] . These considerations resulted in various extensions of the original matter bounce paradigm. For instance, one may realize a small deviation from the exact matter contracting phase to obtain the red tilt, as achieved in the quasi-matter bounce cosmology [109, 110]. In this case, however, a specific, tuned form of the scalar field potential was introduced, making the model seemingly unnatural.

Recently, it was proposed that a ΛCDM bounce scenario could solve some of the aforementioned challenges by simply considering a cosmological constant plus an almost pressureless dark matter fluid during the contracting phase [111]. However this natural sounding scenario produces too much running of the spectral index, we will discuss this in section 5.4.

The goal of this chapter is to determine whether viable models of the matter bounce can be constructed using low energy DOF that can be seen with low redshift observations. The ΛCDM bounce scenario would have been an example but does not agree with the CMB data. Dark energy and dark matter are the two dominant components governing the evolution of the universe today and in the ΛCDM model, those two sectors are decoupled and probed indirectly through their gravitational effects. However there exists the possibility of a small, but non zero, interaction between the dark sector. This scenario is dubbed the interactive DE model (see [112, 113, 114] for earlier literature and [115, 116, 117] for comprehensive reviews on DE dynamics). The interaction term between DE and DM could give rise to new features in the formation of LSS, and the corresponding constraints were studied extensively in the past (for example, see[118, 120, 121, 122, 119, 123, 124] and references therein). In particular, the recent BOSS experiment of the SDSS collaboration [125] indicates a slight deviation (at 2σ CL) in the expected ΛCDM value of the Hubble parameter and the angular distance at an average redshift of $z = 2.34$. These observational hints could be modeled by wCDM [126, 127] and interactive DE [128, 129, 130] models. A statistical analysis of these models using the BOSS data was done in [131].

Here we consider the influence of the DE and DM interaction during the contracting phase assuming that primordial cosmological perturbations were mainly generated by the vacuum fluctuations of a massless scalar field. In our model, the dark interaction modulates the background evolution to yield a small deviation from the exact matter contraction phase when the universe was dominated by DM before the bounce. We find it is possible to obtain

a red tilt for the primordial isocurvature perturbations which can then be transfered into the adiabatic mode. In addition, because the dark sector interaction term may survive the bounce and influence late time dynamics [8], this physical interpretation of the CMB red tilted power spectrum would be connected to the essence of DE and DM dynamics measured by astronomical surveys in the late time universe.

The interaction would produce observable signatures in the LSS of which we may already have discovered hints [133]. This would provide a testable mechanism that explains the CMB measurement of the spectral index in the context of the Matter Bounce scenario.

The chapter is organized as follows. We begin by a review of perturbation theory of a matter bounce cosmology in Section 5.2 (here we cover additional important details that were omitted in Chapter 1) along with the shortcomings of the original scenario. In section 5.3 we perform the analysis of the energy scales that was present at the time the primordial perturbation modes associated with the CMB window were initially exiting the Hubble radius. From this study, we show that a sizable parameter space allows for a very low energy density at that epoch, and hence could be probed with the late-time observations. In Section 5.4, we first revisit the possibility of generating a red tilt for the power spectrum of primordial perturbations within the ΛCDM bounce and describe why it fails. Afterwards, we show that a tilt can be achieved after assuming an existence of the interaction term between DE and DM. We conclude with a discussion in Section 5.5.

5.2 Generation of Perturbations in a Bouncing Model - Part Deux

Figure 5.1 shows the cartoon of a bouncing scenario in conformal time. One notable feature is how certain of the comoving modes become larger than the Hubble radius as it decreases

[8] However, as discussed in Ref. [132], undergoing a bounce at very high energies could result in the variation of the physical constants to random values, and thus in this case the pre-bounce coupling wouldn't "survive". We will assume that such situation does not occur.

during the contraction. [9] It is during horizon crossing that the statistical properties of the fluctuations are partially determined (i.e. quantities such as the spectral index of a given field's power spectrum).

As discussed at the beginning of the chapter, fluctuations in the adiabatic direction of known bouncing models will generically yield a scalar power spectrum whose tilt is irreconcilable with CMB measurements. Hence one has to resort to an entropic mode which must eventually seed the fluctuations seen today. Here we briefly review the details behind those statements. Our scenario requires two key ingredients. The first is some matter to produce the correct contraction while the second is a homogeneous massless scalar field φ.

The scalar fluctuations can be characterized by the comoving curvature perturbation whose Fourier mode k is given by, [75, 77],

$$\mathscr{R}_k = \psi_k - \frac{H}{\rho + p}\delta q_k \,, \tag{5.1}$$

where ψ_k is the curvature perturbation, ρ is the energy density, p is the pressure density and δq_k is the scalar part of the 3-momentum. We can rewrite $\mathscr{R}_k$ in terms of gauge-invariant variables of the individual fluid components as the quantities ρ, p and δq_k are simply the sum of the individual quantities of each component. Namely, defining $Q_k^{(i)} = -\delta q_k^{(i)} + \frac{\rho^{(i)}+p^{(i)}}{H}\psi_k$ we have,

$$\mathscr{R}_k = \frac{H}{\rho + p}\sum_i Q_k^{(i)}. \tag{5.2}$$

For instance a massive scalar field χ with potential $V(\chi) = m^2\chi^2/2$ will have an EoS that oscillates around 0. This field can drive a matter contraction provided these oscillations occur on a time scale much shorter than a Hubble time. Throwing a massless scalar

[9] Note that the small scale modes in the CMB entered the Hubble radius during a radiation dominated period. As the Matter Bounce scenario requires these same modes to exit the Hubble radius during a matter dominated epoch, it implies that a perfectly symmetric bounce cannot occur. The cosmological history must therefore be asymmetric. This can be obtained by having a period of "reheating" in which some of the energy density is transformed into radiation [139] allowing for a longer period of radiation domination after the bounce.

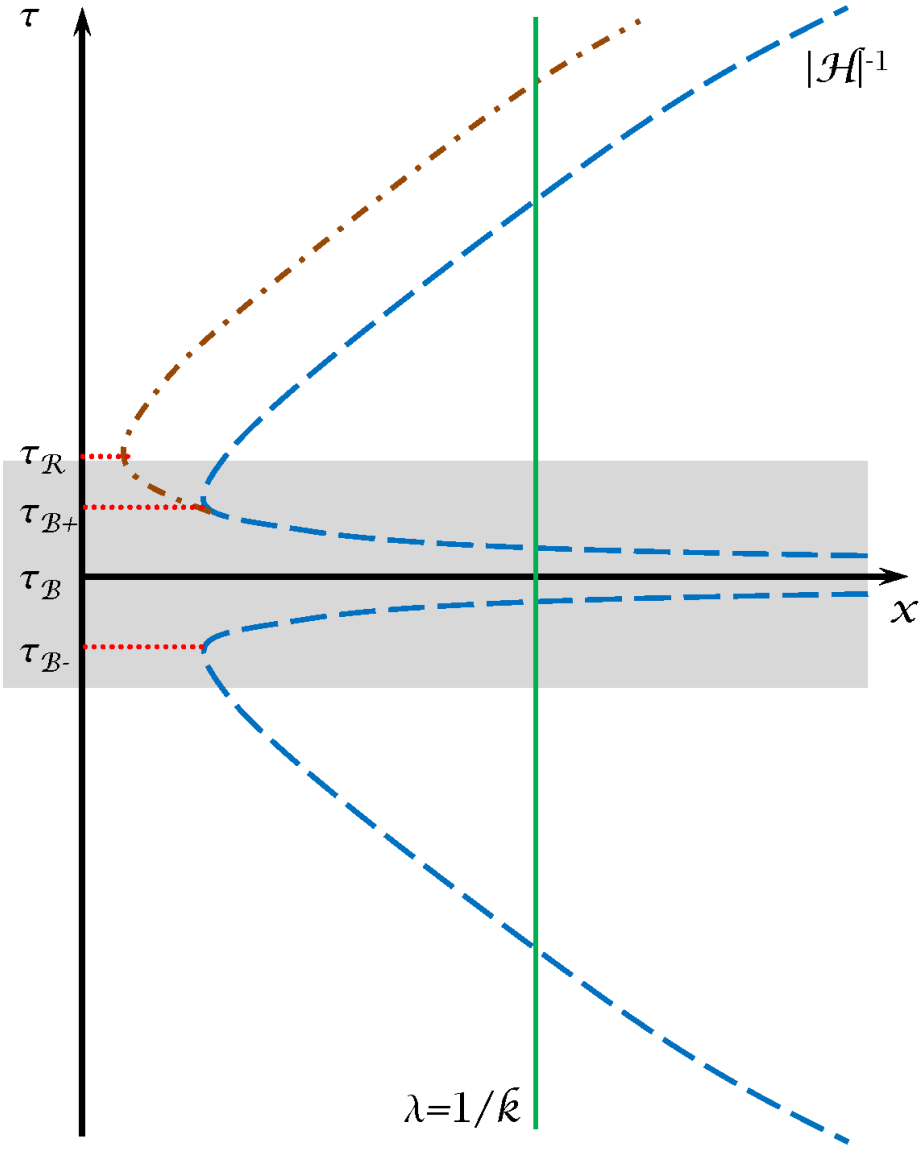

Figure 5.1: A potential depiction of a non-singular bounce in conformal time. A mode λ first exits the Hubble horizon prior to the bounce and reenters thereafter. The different times label different epochs: a non-singular bounce phase starts at τ_{B-}, ends at τ_{B+} and then a reheating phase occurs until τ_{reh}. The blue-dashed conformal Hubble radius represents only one particular model where the background EoS is $w > 0$ except during the bounce. The brown dot-dashed line is another possible evolution if some energy density with EoS having $w < -1/3$ dominates the evolution between the bounce and reheating. We will remain agnostic about what happens in the shaded bouncing region and focus on studying the contracting phase beforehand and assume a standard radiation dominated Big Bang cosmology afterwards. When discussing the energy scale of the Matter Bounce in section 5.3, we will make the assumption that the uncertain shaded region, encompassing the start of the bouncing phase until the end of reheating, occurs quick enough that it can be well approximated by a singular bounce where the scale factor is continuous but the Hubble parameter might not.

field φ in the mix, we have a two field model which was studied in [102] and allows us to write,

$$\mathscr{R}_k = H\Big(\frac{\dot{\varphi}Q_k^{(\varphi)} + \dot{\chi}Q_k^{(\chi)}}{\dot{\varphi}^2 + \dot{\chi}^2}\Big), \tag{5.3}$$

with $Q_k^{(\varphi)} = \delta\varphi_k + \frac{\dot{\varphi}}{H}\psi_k$ being the gauge invariant Mukhanov-Sasaki variable of φ (and $Q_k^{(\chi)}$ is the corresponding one for χ). Hence, as long as χ dominates the energy density $\rho \sim \dot{\chi}^2 + m^2\chi^2$ we have $\dot{\chi} \gg \dot{\varphi}$ and the spectrum of $\mathscr{R}_k$ is set by $Q_k^{(\chi)}$. This can change if φ becomes the dominant field and reflects some of the time dependence of $\mathscr{R}_k$ if there is a significant non-adiabatic pressure component.

We define $u_k^{(\chi)} = aQ_k^{(\chi)}$ and $u_k^{(\varphi)} = aQ_k^{(\varphi)}$ as these variables have equations of motion that can be written as [77],

$$\big(u_k^{(\chi)}\big)'' + \Big(k^2 + m^2a^2 - \frac{a''}{a}\Big)u_k^{(\chi)} = 0, \tag{5.4}$$

$$\big(u_k^{(\varphi)}\big)'' + \Big(k^2 - \frac{a''}{a}\Big)u_k^{(\varphi)} = 0. \tag{5.5}$$

For the massless scalar field this is solved by the two solutions,

$$u_k^{(\varphi)} = \frac{A}{\sqrt{2k}}\mathrm{e}^{-ik\tau}\Big(1 - \frac{1}{k\tau}\Big) + \frac{B}{\sqrt{2k}}\mathrm{e}^{ik\tau}\Big(1 + \frac{1}{k\tau}\Big). \tag{5.6}$$

At very early times, when $k\tau \gg 1$, imposing the Minkowski vacuum state picks out the $A = 1,\ B = 0$ solution. At late time when $\tau k \ll 1$ this initial condition evolves to yield a scale invariant spectrum

$$P_k^{(\varphi)} \sim k^3\Big|\frac{u_k^{(\varphi)}}{a}\Big|^2 \sim \frac{1}{\tau^6}. \tag{5.7}$$

The situation is more complicated for the massive field due to the a^2m^2 term. If the field is to mimic matter we require that $m^2a^2 \gg k^2$. Then at small scale we can impose initial conditions using the WKB approximation,

$$u_k^{(\chi)} = \frac{1}{\sqrt{2am}}\mathrm{e}^{-i\int^\tau am\mathrm{d}\tau}, \tag{5.8}$$

which is valid if $m \gg 2/\tau$. This approximation turns out to fail when $m^2a^2 \sim a''/a$ and transition to a solution of the form $u_k^{(\chi)} \sim A\tau^2 + B/\tau$ with both coefficients A and B set by the initial conditions which are independent of k. Therefore we can conclude that the amplitudes of the modes $u_k^{(\chi)}$ have no k dependence and the spectrum is deeply blue as it goes like $P_k^{(\chi)} \sim k^3$.

One can note that the initial spectrum of perturbations will depend on the details of the component responsible for the matter contraction. To see this in more detail let us assume for simplicity that no entropy perturbation exists. The only energy component will be an unknown matter-like fluid described by its EoS $w = p/\rho \simeq 0$ and its speed of sound $c_s^2 = (\partial p/\partial\rho)|_s = \dot{p}/\dot{\rho}$. An equation of motion can then be written for $u_k = z\mathscr{R}_k$ where $z = a\frac{\sqrt{\rho+p}}{Hc_s}$ [140],

$$u_k'' + \left(c_s^2k^2 - \frac{z''}{z}\right)u_k = 0. \tag{5.9}$$

The properties of the fluid on the evolution of u_k are captured by z and the speed of sound. This would generate a scale invariant spectrum provided that $z \propto a$ and $\dot{c_s}/c_s \ll H$. A scalar field with exponential potential can fulfill these properties [109, 110], but in our previous example we had time varying EoS for χ which made z not proportional to a. More realistically we would expect the matter contraction to be due to some non relativistic perfect fluid composed of dust particles. In this case the speed of sound grow as $c_s \propto a^{-1}$ hence $z \propto a^2$, giving a blue spectrum.

Nevertheless, even with an entropic mechanism the above models does not generate a slight red tilt. To obtain such feature, consider a background evolving as $a \sim \tau^p$ so that $a''/a = p(p-1)/\tau^2$. A slight deviation from perfect matter contraction, parametrized by $\varepsilon \ll 1$ through $p = 2(1+\varepsilon)$, gives $a''/a \approx \frac{(3/2+2\varepsilon)^2-1/4}{\tau^2} = \frac{\nu_s^2-1/4}{\tau^2}$. This allows the spectral index of the massless scalar field to be red as it is given by $n_s - 1 = 3 - 2\nu_s = -4\varepsilon$. The measurement of $n_s \sim 0.968 \pm 0.006$ provided by the latest Planck data[58] determines the

needed value of ε. A mechanism converting this entropic perturbation to an adiabatic one, such as presented in [102], would provide $\mathscr{R}_k$ with the correct spectrum.

The hope we'd like to convey in this chapter is that such deviation from perfect matter contraction should be due to physics that still impacts the cosmological evolution after the bounce and hence be tested. The logic behind the statement stems from an EFT point of view: if the matter bounce occurs at low energy scales - a question that will be explored in section 5.3 - only the low energy degree of freedoms will be important to describe the dynamics. Such low energy DoF might only become observable again at late times, the cosmological constant being an example. If future observations could detect a departure from the expected ΛCDM expansion, it could be a nice hint for the validity of a matter bounce if the same departure during the contraction allows for a red tilt to be generated. This point of view naturally raises questions about the nature of the required massless isocurvature mode. For instance where is it today? In the current chapter we do not attempt to give a satisfying answer to this question. It could be something along the line of a quintessence field responsible for dark energy, a natural candidate in the context of section 5.4.2 where we will consider an explicit model that realizes the red tilt.

5.3 The Energy Scale During Contraction

In this section we argue that Matter Bounce models can generically have small energy density at the time the CMB modes exited the horizon. We will make the assumption that the background evolves with an EoS $w(t) \geq 0$ that is increasing (decreasing) towards (away from) the bounce. This insures that the comoving Hubble radius $\mathscr{H}^{-1}$ shrinks and grows in a way similar to what is shown by the blue-dashed curve on the plot of Figure 5.1. This would be false if the bounce itself was triggered by a NEC violating fluid as it would have

$w < -1$ which is smaller than $w = 0$ during matter contraction (and seen around the bounce point of of Figure 5.1). This assumption can also break down if a phase transition - which one could expect to happen - occurred at very early time. In that case, parts of the universe can be trapped in a false vacuum leading to topological defects. These defects can cause an inflationary stage to occur which then makes it impossible to meaningfully estimate the energy scales involved before the bounce. As such, we want to focus on scenarios which does not have (or have an expansion close to) an inflationary period between the matter contracting phase and today. We also haven't found evidence for any type of matter (other than the CC) with $w < 0$ and it is reasonable to consider bouncing models that does not have such ingredients dominating the background for long period of times. This implies that our conclusions, and assumption, will be approximately correct provided the scale factor does not evolve appreciably during any times some energy component with negative EoS dominates. For instance, we assume the bounce occurs in such a way that the scale factor is of similar size across the bounce, i.e. $a(\tau_{B-}) \simeq a(\tau_{B+})$ using the notation in Figure (5.1).

The smallest length seen in the CMB by Planck is about 100 times smaller than the BAO scale of about 150Mpc today, denote the comoving wavenumber of this mode by k_s. It crosses the horizon twice at $k_s = a_- H_- = a_+ H_+$ when it is exiting(entering) at $-(+)$. The largest scale in the CMB is about 10^3 times bigger and labeled by $k_L = 10^{-3} k_s$. We parametrize our ignorance of the background between the time of the bounce and the time k_s exits the Hubble radius by an effective EoS by w_-. With this we can write,

$$k_s = a_- H_B \Big(\frac{a_B}{a_-}\Big)^{\frac{3}{2}(w_-+1)}, \tag{5.10}$$

which implies,

$$\frac{a_B}{a_-} = \Big(\frac{k_s}{H_B a_B}\Big)^{\frac{2}{1+3w_-}}. \tag{5.11}$$

The energy density when $k_s = a_- H_-$ is

$$\rho_-^s \simeq M_p^2 H_-^2 \simeq M_p^2 H_B^2 \Big(\frac{a_B}{a_-}\Big)^{3(w_-+1)}$$

$$\simeq M_p^2 H_B^2 \Big(\frac{k_s}{H_B a_B}\Big)^{6\frac{(1+w_-)}{1+3w_-}}. \tag{5.12}$$

We similarly parametrize the EoS after the bounce but before BBN by w_+ in order to write,

$$H_{B+}\Big(\frac{a_B}{a_{BBN}}\Big)^{3(1+w_+)/2} = H_{BBN}\,. \tag{5.13}$$

This allows us to express a_B in terms of the Hubble scale right after the bounce H_{B+} and at BBN H_{BBN}.

Moreover the energy scale after reheating must be higher than $\rho_{BBN} \simeq \mathrm{MeV}^4$ but must be below the energy scale of the bounce, therefore $H_B \geq H_{B+} \geq H_{BBN}$. As assuming $w_+ \geq 0$ implies ρ_-^s is maximized by having H_{B+} as large as possible, we set $H_{B+} = H_B$ to get an upper bound. With this we find,

$$\begin{aligned}\rho_-^s &\lesssim M_p^2 H_B^{\frac{4(w_- - w_+)}{(1+3w_-)(1+w_+)}} H_{BBN}^{\frac{-4(1+w_-)}{(1+3w_-)(1+w_+)}} \Big(\frac{k_s}{a_{BBN}}\Big)^{6\frac{(1+w_-)}{1+3w_-}} \\ &\simeq \Big(\frac{M_p k_s}{a_{BBN}}\Big)^{6\frac{(1+w_-)}{1+3w_-}} \big(E_{BBN}^{-1-w_-} E_B^{w_- - w_+}\big)^{\frac{8}{(1+w_+)(1+3w_-)}},\end{aligned} \tag{5.14}$$

where in the second line we have rewritten H_B and H_{BBN} in terms of the energy scale using $M_p^2 H^2 \simeq E^4$. We can now plug in some numbers to see what we could expect from different types of bounce models. With a_0 being the scale factor today, we have the following known values for the parameters in Eq. (5.14),

$$\begin{aligned}&k_s/a_0 \sim \mathrm{Mpc} \sim 10^{-38}\mathrm{GeV}, \quad a_{BBN}/a_0 \sim 10^{-8}, \\ &E_{BBN} \sim 10^{-3}\mathrm{GeV}, \quad M_p \sim 2.4 \times 10^{18}\mathrm{GeV}.\end{aligned} \tag{5.15}$$

Three numbers remain unknown: w_-, w_+ and E_B. As k_s re-enters the Hubble radius during the radiation epoch we might expect w_+ to be close to $1/3$. We will then consider two cases to represent Eq.(5.14) : one with $w_+ = 0$ and the other with $w_+ = 1/3$. Note

that the upper bound becomes smaller as w_+ increases. As a function of the energy scale of the bounce E_B, figure (5.2) shows the upper bound on the energy scale during first horizon crossing $E_k = (\rho_-(k))^{1/4}$ for various modes k and effective EoS w_-. The solid black line represents the energy scale at the time k_s exits the horizon if $w_- \gg 1$, i.e. an Ekpyrotic phase takes place between the bounce and τ_- when $k_s = a_- H_-$. If the CMB scales leave the horizon solely during an Ekpyrotic phase (i.e. we do not have a Matter Bounce scenario) we still can compute E_{k_L} which is shown by the dashed blue line. We see that large numbers such as $E_{k_s} \sim 10^5$GeV can be achieved if ρ_B occurs near the planck scale. On the other hand a Matter Bounce model would require a matter dominated contraction prior to τ_-. This would yield a E_{k_L} given by the dotted black line which is at most on the order of a GeV. Therefore, in models with a very long Ekpyrotic phase we expect E_k to be quite large and independent of w_+. Of course it is sensible to expect the matter dominated phase to last for some time after τ_-, hence at the other extreme we can have models with a matter domination epoch for most of the contracting phase with $w_- \simeq 0$. This yields a $E_{k_s}(E_{k_L})$ shown by the solid(dotted) red line. The energy scales are much lower and take values as low as 10^{-28} GeV for $w_+ = 1/3$ and 10^{-18} GeV for $w_+ = 0$. Interpolating between the two extremes of w_- we will find that any specific model should lie in the green region. Nevertheless, this identifies the existence of a large parameter space which has Matter Bounce models which generate the statistical properties of the CMB fluctuations at very low energies. These numbers should be compared to the current energy density today, $\rho_0 \simeq (10^{-12}\text{GeV})^4$.

What happens if w_+ is negative? The power of E_B is given by $\frac{8(w_- - w_+)}{(1+w_+)(1+3w_-)}$ and so lowering w_+ will increase the bound on ρ_-^s to render it meaningless. Models that have such features push ρ_-^s to large values. However, as no topological defects have been detected, if they where produced they must have decayed into radiation at very early times. Additionally, the monopole problem could impose bounds on the bounce scale which could further reduce the parameter space of Figure 5.2. Hence we restate that such components

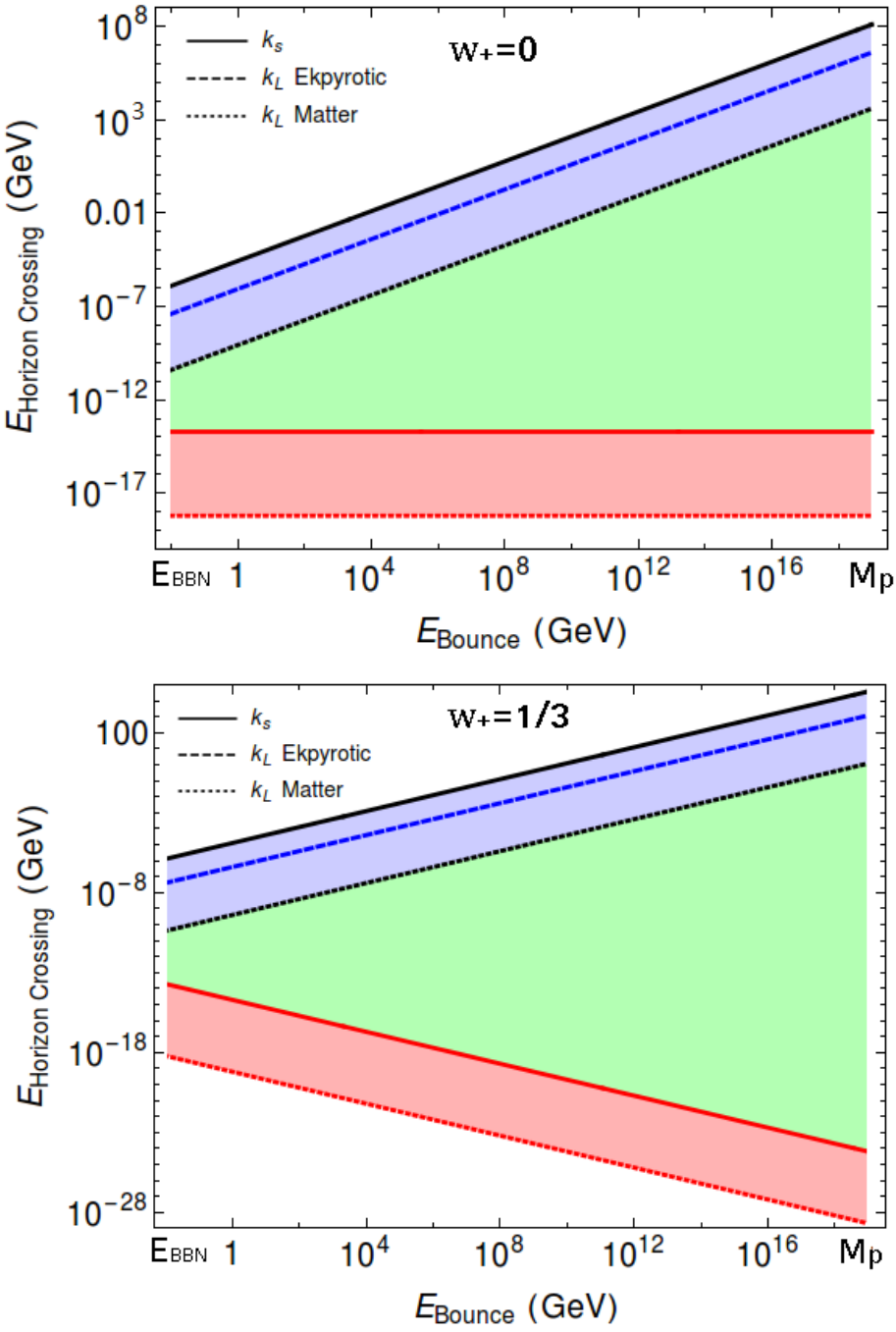

Figure 5.2: A plot of an upper bound on the energy scale during Hubble crossing of the CMB modes in the contracting phase as a function of the energy scale at the bounce. The solid lines represents the smallest mode k_s while the dotted ones represents the largest mode k_L. The shaded region characterize our ignorance on the effective background EoS w_- from the time k_s crosses the horizon until the bounce. The top solid line occurs when $w_- \gg 1$ while the bottom solid line is when $w_- = 0$. We expect any Matter Bounce models to fall in the green region that interpolates between these two extremes. These plots do depend on the effective EoS after the bounce and BBN which we denote by w_+. See the text for additional details.

can exist and yet still impose a strong lower upper bound on ρ^s_- as long as the defects do not dominate the evolution for a significant amount of time. It would be interesting to see how these conclusions are affected when analyzing models with such features.

5.4 The CMB Red Tilt

We've mentioned earlier that a slight deviation from matter contraction can produce a small tilt in the power spectrum of a massless scalar field. A red tilt is generated if an energy density with $w < 0$ dominates during the contracting phase. To produce a slight red tilt, one might consider pressureless matter $w = 0$ to be the dominant contribution and some subdominant energy component with $w < 0$ so that the effective w is slightly less than, but still very close to, zero. Some possibilities with this behavior include the CC with $w = -1$, defects, such as domain walls with $w = -2/3$ and cosmic strings with $w = -1/3$. The last two examples might create additional difficulties for the homogeneity of the background if they become significant when approaching the bounce, for instance a network of intersecting strings would eventually evolve as an inhomogeneous radiation fluid [142]. It has been argued that a cosmological constant could give rise to the desired tilt [111]; however, we demonstrated in section 5.4.1 that the desired tilt cannot be maintained for a wide enough range of k as there will be significant running. This issue can be avoided by using an interacting dark energy model which we explore in section 5.4.2.

5.4.1 Matter Contraction with Non-Interacting Dark Energy (the ΛCDM Bounce Scenario)

Assuming the EoS of dark energy is $p_d = w\rho_d$, the Friedmann equation is

$$H^2 = \frac{1}{3M_p^2}\left(\rho_m + \rho_d\right) \ , \tag{5.16}$$

with $\rho_m = \rho_{m0} a^{-3}$ and $\rho_d = \rho_{d0} a^{-3(1+w)}$. For $w = -1$ we return to the ΛCDM bounce scenario discussed in Ref. [111]. We introduce the ratio of DM and DE energy density $\rho \equiv \rho_m/\rho_d$ and define $\rho_0 \equiv \rho_{m0}/\rho_{d0}$, so that $\rho = \rho_0 a^{3w}$. In conformal time, Eq.(5.16) can be expressed as

$$a'(\tau) = \frac{1}{\sqrt{3}M_p}\sqrt{a\rho_{m0}\left(1+\frac{1}{\rho}\right)}\,. \tag{5.17}$$

Taking a derivative with respect to τ,

$$a''(\tau) = \frac{1}{6M_p^2}\rho_{m0}\left(1+\frac{1-3w}{\rho}\right)\,. \tag{5.18}$$

As $\rho \gg 1$ in the matter dominated stage, we can solve for a to first order in $1/\rho$,

$$a \simeq \frac{\rho_{m0}}{12M_p^2}\tau^2(1+(1-3w)/\rho)\,, \tag{5.19}$$

which leads to the following expression for the ratio a''/a,

$$\frac{a''}{a} \simeq \frac{2}{\tau^2}\Big(1+\frac{2(1-3w)^2-1}{2(1-3w)\rho}+\mathscr{O}(1/\rho^2)\Big) \simeq \frac{v_s^2-\frac{1}{4}}{\tau^2}\,, \tag{5.20}$$

with $v_s \simeq \frac{3}{2}+\frac{2(1-3w)^2-1}{3(1-3w)\rho}$. Therefore, as shown in section 5.2, the spectral index of our massless field is estimated to be,

$$n_s - 1 = 3 - 2v_s = -\frac{4(1-3w)^2-1}{3(1-3w)\rho}. \tag{5.21}$$

For $w < 0$, this gives the desired red tilt. Note that because $\rho = \rho_0 a_0^{3w}\tau^{6w}$ is time dependent, the spectral index should be calculated at the time of horizon exit $|\tau_k| \sim 1/k$ of each mode. Thus we find

$$n_s - 1 \sim -\frac{4(1-3w)^2-1}{3(1-3w)\rho_0 a_0^{3w}}k^{6w}, \tag{5.22}$$

which is heavily dependent on k for $w \simeq -1$. In this case, the spectral running is

$$\alpha_s = \frac{dn_s}{d\ln k} = -6(n_s-1), \tag{5.23}$$

and is larger than the absolute value of $n_s - 1$ by a factor of 6. The current observational bounds on α_s are smaller than $n_s - 1$ by about one order of magnitude [58]; therefore, the ΛCDM bounce scenario cannot generate the observed cosmological perturbations.

5.4.2 Matter Contraction with Interacting Dark Energy

We now present a mechanism to generate a red power spectrum with little running. The mechanism relies on the introduction of a dark matter and dark energy interaction. Such interactions in the dark sector have been considered previously in the literature [144, 145, 113, 146, 147, 148] as an attempt to explain the coincidence problem and are precisely of the form needed to generate a slight red tilt with little running in a contracting universe.

Consider a phenomenological model with dark energy and matter being two fluids having energy-momentum tensor $T_d^{\mu\nu}$ and $T_m^{\mu\nu}$ respectively. By Einstein equations and the Bianchi identity, the total energy-momentum tensor is conserved,

$$0 = \nabla_\mu T^{\mu\nu} = \nabla_\mu T_d^{\mu\nu} + \nabla_\mu T_m^{\mu\nu} = Q_d^\nu + Q_m^\nu \,. \tag{5.24}$$

Here $\nabla_\mu T_i^{\mu\nu} = Q_i^\nu$ is non zero whenever interactions are present. Thus the energy transfer satisfies $Q_m^0 = -Q_d^0 \equiv Q$. While the background evolution remains adequately described by Eq.(5.16). The energy conservation equations for matter and dark energy are expressed as

$$\dot{\rho}_m + 3H\rho_m = Q \,, \tag{5.25}$$

$$\dot{\rho}_d + 3H(\rho_d + p_d) = -Q \,. \tag{5.26}$$

Here we have used $p_m = 0$ for the matter component and assume a constant EoS $w = p_d/\rho_d \simeq -1$ for dark energy. [10] Thus for $Q > 0$, energy flows from dark energy to matter, and for $Q < 0$ energy flows from matter to dark energy. Using Eq.(5.25) and (5.26), the ratio of matter and dark energy density $\rho \equiv \rho_m/\rho_d$ evolves as

$$\frac{d\rho}{dt} = 3H\rho\left[w + \frac{Q}{9H^3M_p^2}\frac{(1+\rho)^2}{\rho}\right] \,. \tag{5.27}$$

[10] We will have to chose the dark energy EoS to be near, but slightly less than, -1 to insure stability [149].

Unlike the ΛCDM universe corresponding to $Q = 0$, this expression allows for a non-trivial fixed point if $Q \propto H^3$. In what follows we consider one of the simplest model of interacting dark energy that have this feature, namely $Q = 3H\Gamma\rho_m$ with a constant $\Gamma > 0$. In this case, Eq.(5.25) and Eq.(5.26) become

$$\frac{d\rho_m}{da} + 3(1-\Gamma)\frac{\rho_m}{a} = 0 \,, \tag{5.28}$$

$$\frac{d\rho_d}{da} + 3(1+w)\frac{\rho_d}{a} + 3\Gamma\frac{\rho_m}{a} = 0 \,. \tag{5.29}$$

Here we used the scale factor a instead of the cosmic time t as it is more convenient to describe the evolution before the bounce. Using this new time coordinate, Eq.(5.27) becomes

$$\frac{d\rho}{da} = \frac{3}{a}\left[\Gamma\rho^2 + (\Gamma + w)\rho\right] \,. \tag{5.30}$$

This equation can be solved analytically. Setting the initial condition $\rho = \rho_0$ at $a = 1$, we have

$$\rho(a) = \frac{\rho_0(w+\Gamma)}{(w+\Gamma+\rho_0\Gamma)a^{-3(w+\Gamma)} - \rho_0\Gamma} \,. \tag{5.31}$$

In Fig.5.3 we compare $\rho(a)$ for an interacting dark energy model against the ΛCDM prediction and show how the fixed point is approached at $\rho = \rho^+$ for $a \ll 1$. The value of ρ^+ is obtained using Eq.(5.30) and the condition $\frac{d\rho}{da} = 0$. We find two constant solutions of ρ,

$$\rho^+ = -\frac{\Gamma + w}{\Gamma} \quad \text{and} \quad \rho^- = 0 \,. \tag{5.32}$$

Thus in a situation with $\Gamma \ll 1$, we have $\rho \simeq \rho+ \gg 1$ for $a \ll 1$ and this nearly constant stage is matter dominated.

In what follows, we show how a slight red tilt for $P_\varphi(k)$ is produced from this interacting dark energy model. Solving Eq.(5.28) we find $\rho_m \propto a^{-3(1-\Gamma)}$ and using this with the first Friedmann Equation (5.16) in the regime where ρ is approximately constant, we find $a(t) \propto t^{2/3(1-\Gamma)} \propto \tau^{2/(1-3\Gamma)}$. The perturbations of φ are again be given by Eq. (5.5) with,

$$\frac{a''}{a} = \frac{\left(\frac{2}{1-3\Gamma} - \frac{1}{2}\right)^2 - 1/4}{\tau^2} = \frac{v_s^2 - 1/4}{\tau^2}. \tag{5.33}$$

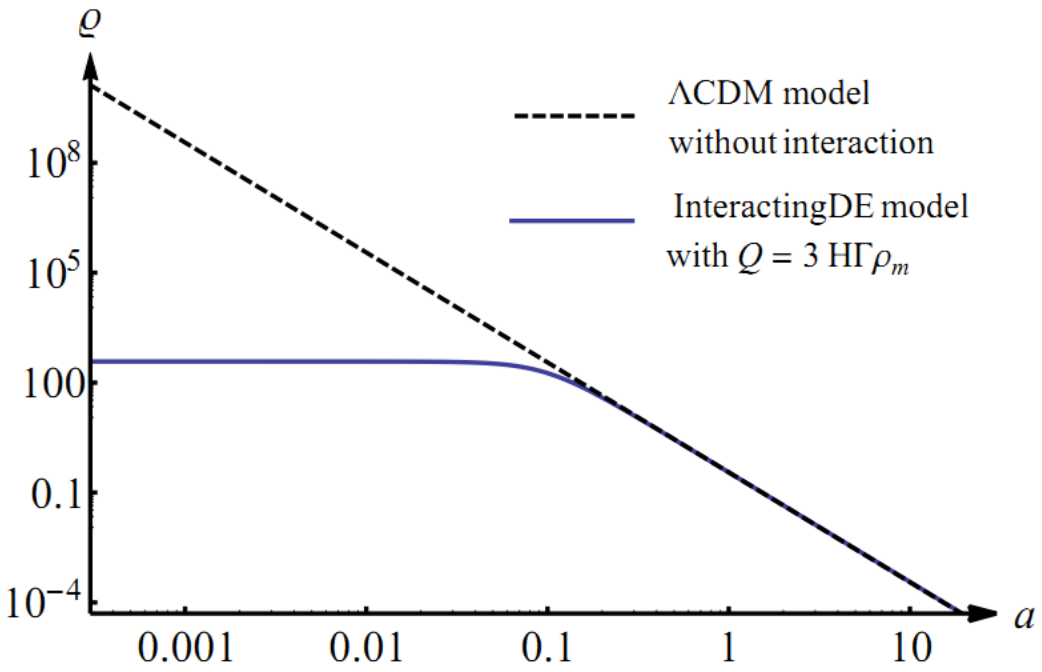

Figure 5.3: The evolution of DM to DE energy density ratio $\rho \equiv \rho_m/\rho_d$ in two different models. Here we set $\Gamma = 0.0026$ and $w = -1$.

The spectral index is therefore, $n_s - 1 = 3 - 2v_s = 4 - \frac{4}{1-3\Gamma}$. The latest Planck measurements [58] set $n_s = 0.968 \pm 0.006$ which fixes $\Gamma = 0.0026 \pm 0.0005$ in order to get the measured red tilt. Another feature, arising due to being near the fix point, is that the running of n_s will be small and negative, the exact value is related to the time variation of ρ.

Having such energy transfer will also affect the late time universe by altering the cosmological expansion. Therefore this model can, and has, been tested by late time observations [131, 129]. The analysis of [131] fits $\Gamma = 0.002272^{+0.00103}_{-0.00137}$ at the 68% confidence level for Planck+BAO data, and $\Gamma = 0.001494^{+0.00065}_{-0.00116}$ at the 68% confidence level for Planck+BAO+SNIa+H0 data. There are still large uncertainties in these constraints but the fit suggests a 2 sigma deviation from ΛCDM and an agreement with the demands to generate the proper red tilt. Improvements on measurements in the not so distant future will further determine the viability of such scenarios.

5.5 Conclusion

As an alternative to the simple picture given by the inflationary scenario, current Matter Bounce models require many intricacies to agree with observations. The original idea of having a single massless scalar field responsible for the CMB perturbations cannot explain the observed red tilt. Additional parameters must be added to achieve these features. This presents a difficult challenge for the Matter Bounce scenario, however, if the new parameters are expected to exist, observational opportunities are also present. This is where a particularly interesting feature of the Matter Bounce comes into play: the energy density of the universe at the time the statistical properties of the perturbations are frozen in can be very low, in some cases many order of magnitude smaller than today's energy density. Hence unlike other pre Big Bang or early universe scenarios, only low energy degrees of freedom are relevant during the times of CMB mode horizon crossing. The observations that uncover those degrees of freedom are made at low redshifts where their effects are most easily seen. The cosmological constant is an example: it is a parameter of the theory that only becomes important during the late stages of our universe. In a universe where the Matter Bounce occurred, this opens the possibility of determining the identity of the extra parameters that make up a viable model, especially when considering the recent cosmological hints of modified gravity [133]. To illustrate how the hunt for these parameters might ensue, we note that a deviation from perfect matter contraction would give a red tilt to perturbations. Whatever is responsible for this deviation is likely to also cause a similar effect after the bounce and can be observationally detected. The introduction of a coupling in the dark sector that allows energy to flow from dark matter to dark energy is able to support a contracting phase giving the correct n_s. These interacting model have been considered as extensions of ΛCDM [131, 129] and the best fit to the Planck+BAO+SNIa+H0 data has the coupling Γ deviate from 0 at the 2 sigma confidence level. Intriguingly, the strength of

the coupling needed to set the measured CMB value of n_s sits comfortably within the error bars found by this analysis.

It is interesting to speculate further about the potential new signatures that might arise in viable Matter Bounce models. For instance, another issue faced by matter bounce scenario is to realize a small tensor-to-scalar ratio consistent with the CMB observations, which has been comprehensively reviewed in [82]. However, if future low redshift observations could detect a small graviton mass [19], this feature would change the details of how the tensor modes are created during the contracting phase and affect the predictions for the tensor-to-scalar ratio. Therefore, besides the specific example about interacting dark energy considered in this chapter, it is also interesting to further explore the role of massive graviton in matter bounce models as another example of our idea.

Additionally, probing the matter bounce using low redshift observations could also shed light on experimental tests of nonsingular bounces by other mechanisms, such as by using the direct dark matter searches or the BBN bound as analyzed in Refs.[150, 151, 152, 153].

CHAPTER 6

FINAL REMARKS

The study of modified theories of gravity allow us to broaden the horizons of what we can expect in the late and early Universe. This gives us the ability to formulate more creative models which can fit the observed data. For example, the exotic solutions uncovered in Chapter 3 could point to the existence of surprising new objects at high energies (i.e. relevant in the early Universe). Note that such examples of modified gravity have underlying issues and so are not meant to be taken as serious contenders to a better description of gravity than what is currently given by General Relativity. Instead, they merely serve as toy models which we use to explore the possibilities of what gravitational theories can offer. To complement the above logic, lines of work similar to the one of Chapter 5 attempt to develop new ideas that can determine whether these speculative models hold some truth. In that particular chapter we've explored novel ways to test the ideas behind bouncing cosmologies. Models with a bounce are hard to construct as they generally require a violation of the NEC. Hence one would expect that bouncing cosmologies only occurs in some of these exotic theories of modified gravity. The result of Chapter 5 shows that identifying certain early and late time observations in our Universe could lend support to this idea, hinting that expending energy to improve these models could be fruitful. Employing this type of strategy to push our ignorance of the unknown is sound as they are cheap and fosters creativity. Hopefully the strategy will prove to be successful in the future.

REFERENCES

[1] F. Duplessis and D. A. Easson, Phys. Rev. D **92**, no. 4, 043516 (2015) doi:10.1103/PhysRevD.92.043516 [arXiv:1506.00988 [gr-qc]].

[2] Y. F. Cai, F. Duplessis and E. N. Saridakis, Phys. Rev. D **90**, no. 6, 064051 (2014) doi:10.1103/PhysRevD.90.064051 [arXiv:1307.7150 [hep-th]].

[3] Y. F. Cai, F. Duplessis, D. A. Easson and D. G. Wang, Phys. Rev. D **93**, no. 4, 043546 (2016) doi:10.1103/PhysRevD.93.043546 [arXiv:1512.08979 [astro-ph.CO]].

[4] F. Duplessis and T. Vachaspati, arXiv:1701.01501 [astro-ph.HE].

[5] A. Einstein, "The foundation of the general theory of relativity", Annalen Phys. 49 (1916) 769-822.

[6] R. P. Woodard, Rept. Prog. Phys. **72**, 126002 (2009) doi:10.1088/0034-4885/72/12/126002 [arXiv:0907.4238 [gr-qc]].

[7] S. Weinberg, "Photons and gravitons in perturbation theory: Derivation of Maxwell's and Einstein's equations," Phys. Rev. 138, B988 (1965).

[8] S. Weinberg, "Photons And Gravitons In S Matrix Theory: Derivation Of Charge Conservation And Equality Of Gravitational And Inertial Mass," Phys. Rev. 135, B1049 (1964).

[9] A. Nicolis, R. Rattazzi and E. Trincherini, Phys. Rev. D **79**, 064036 (2009) doi:10.1103/PhysRevD.79.064036 [arXiv:0811.2197 [hep-th]].

[10] Stelle, Phys. Rev. D **16**, 953 (1977)

[11] T. Biswas, E. Gerwick, T. Koivisto and A. Mazumdar, Phys. Rev. Lett. **108**, 031101 (2012) doi:10.1103/PhysRevLett.108.031101 [arXiv:1110.5249 [gr-qc]].

[12] D. Lovelock, J. Math. Phys. **12**, 498 (1971)

[13] T. Padmanabhan and D. Kothawala, Phys. Rept. **531**, 115 (2013) doi:10.1016/j.physrep.2013.05.007 [arXiv:1302.2151 [gr-qc]].

[14] L. Alvarez-Gaume, A. Kehagias, C. Kounnas, D. Lüst and A. Riotto, Fortsch. Phys. **64**, no. 2-3, 176 (2016) doi:10.1002/prop.201500100 [arXiv:1505.07657 [hep-th]].

[15] T. P. Sotiriou and V. Faraoni, Rev. Mod. Phys. **82**, 451 (2010) doi:10.1103/RevModPhys.82.451 [arXiv:0805.1726 [gr-qc]].

[16] A. De Felice and S. Tsujikawa, Living Rev. Rel. **13**, 3 (2010) doi:10.12942/lrr-2010-3 [arXiv:1002.4928 [gr-qc]].

[17] F. Sbisá, Eur. J. Phys. **36**, 015009 (2015) doi:10.1088/0143-0807/36/1/015009 [arXiv:1406.4550 [hep-th]].

[18] K. Hinterbichler, Rev. Mod. Phys. **84**, 671 (2012) doi:10.1103/RevModPhys.84.671 [arXiv:1105.3735 [hep-th]].

[19] C. de Rham, Living Rev. Rel. **17**, 7 (2014) doi:10.12942/lrr-2014-7 [arXiv:1401.4173 [hep-th]].

[20] A. Kehagias, C. Kounnas, D. Lust and A. Riotto, arXiv:1502.04192 [hep-th].

[21] H. Lu, A. Perkins, C. N. Pope and K. S. Stelle, Phys. Rev. Lett. **114**, no. 17, 171601 (2015) [arXiv:1502.01028 [hep-th]].

[22] C. Kounnas, D. Lust and N. Toumbas, Fortsch. Phys. **63**, 12 (2015) [arXiv:1409.7076 [hep-th]].

[23] M. S. Morris and K. S. Thorne, Am. J. Phys. **56**, 395 (1988).

[24] O. James, E. von Tunzelmann, P. Franklin and K. S. Thorne, arXiv:1502.03809 [gr-qc].

[25] M. Van Raamsdonk, Gen. Rel. Grav. **42**, 2323 (2010) [Int. J. Mod. Phys. D **19**, 2429 (2010)] [arXiv:1005.3035 [hep-th]].

[26] J. Maldacena and L. Susskind, Fortsch. Phys. **61**, 781 (2013) [arXiv:1306.0533 [hep-th]].

[27] V. Frolov, M. Markov and V. Mukhanov *Phys. Lett.* **B216**, 272 (1989).

[28] G. Veneziano, *Phys. Lett.* **B265**, 287 (1991).

[29] D. Morgan, *Phys. Rev.* **D45**, R1005 (1992).

[30] V. Mukhanov and R. Brandenberger, *Phys. Rev. Lett.* **68**, 1969 (1992).

[31] L. Smolin, *Class. Quant. Grav.* **9**, 173 (1992).

[32] A. Tseytlin and C. Vafa, *Nucl. Phys.* **B372**, 443 (1992).

[33] M. Trodden, V. Mukhanov and R. Brandenberger, *Phys. Lett.* **B316**, 483 (1993).

[34] G. Alberghi, D. Lowe and M. Trodden, *JHEP* **9907:020** (1999).

[35] R. Daghigh, J. Kapusta and Y. Hosotani, "False Vacuum Black Holes and Universes", hep-ph/0008006, (2000).

[36] D. A. Easson and R. H. Brandenberger, JHEP **0106**, 024 (2001) [hep-th/0103019].

[37] D. A. Easson, JHEP **0302**, 037 (2003) [hep-th/0210016].

[38] S. Deser and B. Tekin, Phys. Rev. Lett. **89**, 101101 (2002) [hep-th/0205318].

[39] S. Deser and B. Tekin, Phys. Rev. D **67**, 084009 (2003) [hep-th/0212292].

[40] S. Deser and B. Tekin, Phys. Rev. D **75**, 084032 (2007) [gr-qc/0701140].

[41] N. Lashkari, C. Rabideau, P. Sabella-Garnier and M. Van Raamsdonk, arXiv:1412.3514 [hep-th].

[42] M. Fierz, W. Pauli, Proc. Roy. Soc. Lond. A **173**, 211 (1939).

[43] H. van Dam and M. J. G. Veltman, Nucl. Phys. B **22**, 397 (1970); V. I. Zakharov, JETP Lett. **12**, 312 (1970).

[44] A. I. Vainshtein, Phys. Lett. B **39**, 393 (1972).

[45] D. G. Boulware, S. Deser, Phys. Rev. D **6**, 3368 (1972).

[46] N. Arkani-Hamed, H. Georgi and M. D. Schwartz, Annals Phys. **305**, 96 (2003).

[47] C. de Rham and G. Gabadadze, Phys. Rev. D **82**, 044020 (2010); C. de Rham, G. Gabadadze and A. J. Tolley, Phys. Rev. Lett. **106**, 231101 (2011).

[48] S. F. Hassan and R. A. Rosen, JHEP **1204**, 123 (2012); S. F. Hassan and R. A. Rosen, Phys. Rev. Lett. **108**, 041101 (2012).

[49] C. de Rham, G. Gabadadze, L. Heisenberg and D. Pirtskhalava, Phys. Rev. D **83**, 103516 (2011); G. D'Amico, C. de Rham, S. Dubovsky, G. Gabadadze, D. Pirtskhalava and A. J. Tolley, Phys. Rev. D **84**, 124046 (2011); K. Koyama, G. Niz and G. Tasinato, JHEP **1112**, 065 (2011).

[50] A. E. Gumrukcuoglu, C. Lin and S. Mukohyama, JCAP **1111**, 030 (2011); A. E. Gumrukcuoglu, C. Lin and S. Mukohyama, Phys. Lett. B **717**, 295 (2012); A. De Felice, A. E. Gumrukcuoglu and S. Mukohyama, Phys. Rev. D **88**, 124006 (2013).

[51] D. Comelli, M. Crisostomi, F. Nesti and L. Pilo, JHEP **1203**, 067 (2012) [Erratum-ibid. **1206**, 020 (2012)]; D. Comelli, M. Crisostomi and L. Pilo, JHEP **1206**, 085 (2012); V. F. Cardone, N. Radicella and L. Parisi, Phys. Rev. D **85**, 124005 (2012); P. Gratia, W. Hu and M. Wyman, Phys. Rev. D **86**, 061504 (2012); T. Kobayashi, M. Siino, M. Yamaguchi and D. Yoshida, Phys. Rev. D **86**, 061505 (2012); D. Langlois and A. Naruko, Class. Quant. Grav. **29**, 202001 (2012); Y. -F. Cai, D. A. Easson, C. Gao and E. N. Saridakis, Phys. Rev. D **87**, 064001 (2013); Y. -l. Zhang, R. Saito and M. Sasaki, JCAP **1302**, 029 (2013); G. Leon, J. Saavedra and E. N. Saridakis, Class. Quant. Grav. **30**, 135001 (2013); K. Hinterbichler, J. Stokes and M. Trodden, Phys. Lett. B **725**, , 1 (2013); K. Zhang, P. Wu and H. Yu, Phys. Rev. D **87**, 063513 (2013); M. S. Volkov, Class. Quant. Grav. **30**, 184009 (2013); G. Tasinato, K. Koyama and G. Niz, Class. Quant. Grav. **30**, 184002 (2013); H. Li and Y. Zhang, arXiv:1304.4780 [gr-qc]; N. Khosravi, G. Niz, K. Koyama and G. Tasinato, JCAP **1308**, 044 (2013); T. Q. Do and W. F. Kao, Phys. Rev. D **88**, 063006 (2013); M. Sasaki, D. -h. Yeom and Y. -l. Zhang, Class. Quant. Grav. **30**, 232001 (2013); Y. -l. Zhang, R. Saito, D. -h. Yeom and M. Sasaki, arXiv:1312.0709 [hep-th]; S. I. Vacaru, arXiv:1401.2882 [physics.gen-ph].

[52] A. De Felice, A. E. Gumrukcuoglu and S. Mukohyama, Phys. Rev. Lett. **109**, 171101 (2012); A. De Felice, A. E. Gumrukcuoglu, C. Lin and S. Mukohyama, JCAP **1305**, 035 (2013); A. De Felice, A. E. Gumrukcuoglu, C. Lin and S. Mukohyama, Class. Quant. Grav. **30**, 184004 (2013).

[53] R. Utiyama and B. S. DeWitt, J. Math. Phys. **3**, 608 (1962).

[54] S. Deser, J. H. Kay and K. S. Stelle, Phys. Rev. Lett. **38**, 527 (1977).

[55] G. A. Vilkovisky, Class. Quant. Grav. **9**, 895 (1992).

[56] A. A. Starobinsky, Phys. Lett. B **91**, 99 (1980).

[57] P. A. R. Ade *et al.*, arXiv:1303.5082 [astro-ph.CO].

[58] P. A. R. Ade *et al.* [Planck Collaboration], arXiv:1502.01589 [astro-ph.CO].

[59] R. H. Brandenberger, hep-ph/9910410.

[60] D. Baumann, doi:10.1142/9789814327183_0010 arXiv:0907.5424 [hep-th].

[61] R. R. Caldwell, M. Kamionkowski and N. N. Weinberg, Phys. Rev. Lett. **91**, 071301 (2003) doi:10.1103/PhysRevLett.91.071301 [astro-ph/0302506].

[62] A. Borde, A. H. Guth and A. Vilenkin, Phys. Rev. Lett. **90**, 151301 (2003) doi:10.1103/PhysRevLett.90.151301 [gr-qc/0110012].

[63] P. A. R. Ade *et al.* [BICEP2 and Keck Array Collaborations], [arXiv:1510.09217 [astro-ph.CO]].

[64] P. A. R. Ade *et al.* [BICEP2 and Planck Collaborations], Phys. Rev. Lett. **114**, 101301 (2015) [arXiv:1502.00612 [astro-ph.CO]].

[65] C. W. Misner, Phys. Rev. Lett. **22**, 1071, (1969)

[66] J. K. Erickson, D. H. Wesley, P. J. Steinhardt and N. Turok, Phys. Rev. D **69**, 063514 (2004) doi:10.1103/PhysRevD.69.063514 [hep-th/0312009].

[67] J. Khoury, B. A. Ovrut, P. J. Steinhardt and N. Turok, Phys. Rev. D **64**, 123522 (2001) [hep-th/0103239].

[68] D. A. Easson, I. Sawicki and A. Vikman, JCAP **1111**, 021 (2011) doi:10.1088/1475-7516/2011/11/021 [arXiv:1109.1047 [hep-th]].

[69] Y. F. Cai, D. A. Easson and R. Brandenberger, JCAP **1208**, 020 (2012) doi:10.1088/1475-7516/2012/08/020 [arXiv:1206.2382 [hep-th]].

[70] A. Ijjas and P. J. Steinhardt, arXiv:1606.08880 [gr-qc].

[71] S. Gielen and N. Turok, arXiv:1510.00699 [hep-th].

[72] D. Battefeld and P. Peter, Phys. Rept. **571**, 1 (2015) doi:10.1016/j.physrep.2014.12.004 [arXiv:1406.2790 [astro-ph.CO]].

[73] M. Libanov, S. Mironov and V. Rubakov, JCAP **1608**, no. 08, 037 (2016) doi:10.1088/1475-7516/2016/08/037 [arXiv:1605.05992 [hep-th]].

[74] M. K. Parikh, JHEP **1510**, 089 (2015) doi:10.1007/JHEP10(2015)089 [arXiv:1501.04606 [hep-th]].

[75] B. A. Bassett, S. Tsujikawa and D. Wands, Rev. Mod. Phys. **78**, 537 (2006) [astro-ph/0507632].

[76] R. H. Brandenberger, arXiv:1206.4196 [astro-ph.CO].

[77] V. F. Mukhanov, H. A. Feldman and R. H. Brandenberger, Phys. Rept. 215, 203 (1992)

[78] D. Wands, Phys. Rev. D **60**, 023507 (1999) doi:10.1103/PhysRevD.60.023507 [gr-qc/9809062].

[79] N. D. Birrell & P. C. W. Davies, Cambridge, Uk: Univ. Pr. (1982) 340p

[80] L. Perreault Levasseur, Phys. Rev. D **88**, no. 8, 083537 (2013) doi:10.1103/PhysRevD.88.083537 [arXiv:1304.6408 [hep-th]].

[81] V. F. Mukhanov, H. A. Feldman and R. H. Brandenberger, Phys. Rept. **215**, 203 (1992). doi:10.1016/0370-1573(92)90044-Z

[82] Y. F. Cai, Sci. China Phys. Mech. Astron. **57**, 1414 (2014) doi:10.1007/s11433-014-5512-3 [arXiv:1405.1369 [hep-th]].

[83] M. Novello and S. E. P. Bergliaffa, Phys. Rept. **463**, 127 (2008) doi:10.1016/j.physrep.2008.04.006 [arXiv:0802.1634 [astro-ph]].

[84] J. L. Lehners, Phys. Rept. **465**, 223 (2008) doi:10.1016/j.physrep.2008.06.001 [arXiv:0806.1245 [astro-ph]].

[85] M. Gasperini and G. Veneziano, Astropart. Phys. **1**, 317 (1993) doi:10.1016/0927-6505(93)90017-8 [hep-th/9211021].

[86] G. Veneziano, Phys. Lett. B **265**, 287 (1991). doi:10.1016/0370-2693(91)90055-U

[87] R. H. Brandenberger and C. Vafa, Nucl. Phys. B **316**, 391 (1989). doi:10.1016/0550-3213(89)90037-0

[88] T. Battefeld and S. Watson, Rev. Mod. Phys. **78**, 435 (2006) doi:10.1103/RevModPhys.78.435 [hep-th/0510022].

[89] R. H. Brandenberger, Class. Quant. Grav. **32**, no. 23, 234002 (2015) doi:10.1088/0264-9381/32/23/234002 [arXiv:1505.02381 [hep-th]].

[90] F. Finelli and R. Brandenberger, Phys. Rev. D **65**, 103522 (2002) doi:10.1103/PhysRevD.65.103522 [hep-th/0112249].

[91] Y. F. Cai, T. Qiu, Y. S. Piao, M. Li and X. Zhang, JHEP **0710**, 071 (2007) doi:10.1088/1126-6708/2007/10/071 [arXiv:0704.1090 [gr-qc]].

[92] Y. F. Cai, T. Qiu, R. Brandenberger, Y. S. Piao and X. Zhang, JCAP **0803**, 013 (2008) doi:10.1088/1475-7516/2008/03/013 [arXiv:0711.2187 [hep-th]]; Y. F. Cai and X. Zhang, JCAP **0906**, 003 (2009) doi:10.1088/1475-7516/2009/06/003 [arXiv:0808.2551 [astro-ph]]; Y. F. Cai, T. t. Qiu, J. Q. Xia and X. Zhang, Phys. Rev. D **79**, 021303 (2009) doi:10.1103/PhysRevD.79.021303 [arXiv:0808.0819 [astro-ph]].

[93] Y. F. Cai, T. t. Qiu, R. Brandenberger and X. m. Zhang, Phys. Rev. D **80**, 023511 (2009) doi:10.1103/PhysRevD.80.023511 [arXiv:0810.4677 [hep-th]].

[94] R. Brandenberger, Phys. Rev. D **80**, 043516 (2009) doi:10.1103/PhysRevD.80.043516 [arXiv:0904.2835 [hep-th]].

[95] Y. F. Cai and E. N. Saridakis, JCAP **0910**, 020 (2009) doi:10.1088/1475-7516/2009/10/020 [arXiv:0906.1789 [hep-th]].

[96] X. Gao, Y. Wang, W. Xue and R. Brandenberger, JCAP **1002**, 020 (2010) doi:10.1088/1475-7516/2010/02/020 [arXiv:0911.3196 [hep-th]].

[97] Y. F. Cai, S. H. Chen, J. B. Dent, S. Dutta and E. N. Saridakis, Class. Quant. Grav. **28**, 215011 (2011) doi:10.1088/0264-9381/28/21/215011 [arXiv:1104.4349 [astro-ph.CO]].

[98] J. de Haro and J. Amoros, Phys. Rev. Lett. **110**, no. 7, 071104 (2013) doi:10.1103/PhysRevLett.110.071104 [arXiv:1211.5336 [gr-qc]].

[99] Y. F. Cai, S. Capozziello, M. De Laurentis and E. N. Saridakis, arXiv:1511.07586 [gr-qc].

[100] C. Lin, R. H. Brandenberger and L. Perreault Levasseur, JCAP **1104**, 019 (2011) doi:10.1088/1475-7516/2011/04/019 [arXiv:1007.2654 [hep-th]].

[101] T. Qiu, J. Evslin, Y. F. Cai, M. Li and X. Zhang, JCAP **1110**, 036 (2011) doi:10.1088/1475-7516/2011/10/036 [arXiv:1108.0593 [hep-th]].

[102] Y. F. Cai, E. McDonough, F. Duplessis and R. H. Brandenberger, JCAP **1310**, 024 (2013) doi:10.1088/1475-7516/2013/10/024 [arXiv:1305.5259 [hep-th]].

[103] Y. F. Cai and E. Wilson-Ewing, JCAP **1403**, 026 (2014) doi:10.1088/1475-7516/2014/03/026 [arXiv:1402.3009 [gr-qc]].

[104] S. Alexander, C. Bambi, A. Marciano and L. Modesto, Phys. Rev. D **90**, no. 12, 123510 (2014) doi:10.1103/PhysRevD.90.123510 [arXiv:1402.5880 [gr-qc]].

[105] S. Alexander, Y. F. Cai and A. Marciano, Phys. Lett. B **745**, 97 (2015) doi:10.1016/j.physletb.2015.04.026 [arXiv:1406.1456 [gr-qc]].

[106] R. H. Brandenberger, AIP Conf. Proc. **1268**, 3 (2010) doi:10.1063/1.3483879 [arXiv:1003.1745 [hep-th]].

[107] J. Quintin, Z. Sherkatghanad, Y. F. Cai and R. H. Brandenberger, Phys. Rev. D **92**, no. 6, 063532 (2015) doi:10.1103/PhysRevD.92.063532 [arXiv:1508.04141 [hep-th]].

[108] Y. F. Cai, W. Xue, R. Brandenberger and X. Zhang, JCAP **0905**, 011 (2009) doi:10.1088/1475-7516/2009/05/011 [arXiv:0903.0631 [astro-ph.CO]].

[109] J. de Haro and Y. F. Cai, Gen. Rel. Grav. **47**, no. 8, 95 (2015) doi:10.1007/s10714-015-1936-y [arXiv:1502.03230 [gr-qc]].

[110] E. Elizalde, J. Haro and S. D. Odintsov, Phys. Rev. D **91**, no. 6, 063522 (2015) doi:10.1103/PhysRevD.91.063522 [arXiv:1411.3475 [gr-qc]].

[111] Y. F. Cai and E. Wilson-Ewing, JCAP **1503**, no. 03, 006 (2015) doi:10.1088/1475-7516/2015/03/006 [arXiv:1412.2914 [gr-qc]].

[112] L. Amendola, Phys. Rev. D **62**, 043511 (2000) doi:10.1103/PhysRevD.62.043511 [astro-ph/9908023].

[113] D. Comelli, M. Pietroni and A. Riotto, Phys. Lett. B **571**, 115 (2003) doi:10.1016/j.physletb.2003.05.006 [hep-ph/0302080].

[114] B. Wang, J. Zang, C. Y. Lin, E. Abdalla and S. Micheletti, Nucl. Phys. B **778**, 69 (2007) doi:10.1016/j.nuclphysb.2007.04.037 [astro-ph/0607126].

[115] E. J. Copeland, M. Sami and S. Tsujikawa, Int. J. Mod. Phys. D **15**, 1753 (2006) doi:10.1142/S021827180600942X [hep-th/0603057].

[116] Y. F. Cai, E. N. Saridakis, M. R. Setare and J. Q. Xia, Phys. Rept. **493**, 1 (2010) doi:10.1016/j.physrep.2010.04.001 [arXiv:0909.2776 [hep-th]].

[117] M. Li, X. D. Li, S. Wang and Y. Wang, Commun. Theor. Phys. **56**, 525 (2011) doi:10.1088/0253-6102/56/3/24 [arXiv:1103.5870 [astro-ph.CO]].

[118] L. Amendola and D. Tocchini-Valentini, Phys. Rev. D **66**, 043528 (2002) doi:10.1103/PhysRevD.66.043528 [astro-ph/0111535].

[119] Z. K. Guo, N. Ohta and S. Tsujikawa, Phys. Rev. D **76**, 023508 (2007) doi:10.1103/PhysRevD.76.023508 [astro-ph/0702015 [ASTRO-PH]].

[120] C. G. Boehmer, G. Caldera-Cabral, R. Lazkoz and R. Maartens, Phys. Rev. D **78**, 023505 (2008) doi:10.1103/PhysRevD.78.023505 [arXiv:0801.1565 [gr-qc]].

[121] J. H. He and B. Wang, JCAP **0806**, 010 (2008) doi:10.1088/1475-7516/2008/06/010 [arXiv:0801.4233 [astro-ph]]; J. H. He, B. Wang and P. Zhang, Phys. Rev. D **80**, 063530 (2009) doi:10.1103/PhysRevD.80.063530 [arXiv:0906.0677 [gr-qc]].

[122] K. Koyama, R. Maartens and Y. S. Song, JCAP **0910**, 017 (2009) doi:10.1088/1475-7516/2009/10/017 [arXiv:0907.2126 [astro-ph.CO]].

[123] J. Q. Xia, Phys. Rev. D **80**, 103514 (2009) doi:10.1103/PhysRevD.80.103514 [arXiv:0911.4820 [astro-ph.CO]].

[124] Y. H. Li and X. Zhang, Phys. Rev. D **89**, no. 8, 083009 (2014) doi:10.1103/PhysRevD.89.083009 [arXiv:1312.6328 [astro-ph.CO]]; Y. H. Li, J. F. Zhang and X. Zhang, Phys. Rev. D **90**, no. 12, 123007 (2014) doi:10.1103/PhysRevD.90.123007 [arXiv:1409.7205 [astro-ph.CO]].

[125] T. Delubac *et al.* [BOSS Collaboration], Astron. Astrophys. **574**, A59 (2015) doi:10.1051/0004-6361/201423969 [arXiv:1404.1801 [astro-ph.CO]].

[126] V. H. Cardenas, Phys. Lett. B **750**, 128 (2015) doi:10.1016/j.physletb.2015.08.064 [arXiv:1405.5116 [astro-ph.CO]].

[127] V. Sahni, A. Shafieloo and A. A. Starobinsky, Astrophys. J. **793**, no. 2, L40 (2014) doi:10.1088/2041-8205/793/2/L40 [arXiv:1406.2209 [astro-ph.CO]].

[128] V. Salvatelli, N. Said, M. Bruni, A. Melchiorri and D. Wands, Phys. Rev. Lett. **113**, no. 18, 181301 (2014) doi:10.1103/PhysRevLett.113.181301 [arXiv:1406.7297 [astro-ph.CO]].

[129] E. Abdalla, E. G. M. Ferreira, J. Quintin and B. Wang, arXiv:1412.2777 [astro-ph.CO].

[130] J. Valiviita and E. Palmgren, JCAP **1507**, 015 (2015) doi:10.1088/1475-7516/2015/07/015 [arXiv:1504.02464 [astro-ph.CO]].

[131] A. A. Costa, X. D. Xu, B. Wang, E. G. M. Ferreira and E. Abdalla, Phys. Rev. D **89**, no. 10, 103531 (2014) [arXiv:1311.7380 [astro-ph.CO]].

[132] S. Alexander, S. Cormack and M. Gleiser, arXiv:1507.00727 [hep-th].

[133] E. Di Valentino, A. Melchiorri and J. Silk, arXiv:1509.07501 [astro-ph.CO].

[134] J. Khoury and P. J. Steinhardt, Phys. Rev. Lett. **104**, 091301 (2010) [arXiv:0910.2230 [hep-th]].

[135] E. I. Buchbinder, J. Khoury and B. A. Ovrut, Phys. Rev. D **76**, 123503 (2007) [hep-th/0702154].

[136] E. Wilson-Ewing, JCAP **1303**, 026 (2013) [arXiv:1211.6269 [gr-qc]].

[137] P. J. Steinhardt and N. Turok, Science **312**, 1180 (2006) [astro-ph/0605173].

[138] M. Koehn, J. L. Lehners and B. Ovrut, arXiv:1512.03807 [hep-th].

[139] J. Quintin, Y. F. Cai and R. H. Brandenberger, Phys. Rev. D **90**, no. 6, 063507 (2014) [arXiv:1406.6049 [gr-qc]].

[140] A. De Felice, J. M. Gerard and T. Suyama, Phys. Rev. D **81**, 063527 (2010) [arXiv:0908.3439 [gr-qc]].

[141] L. Battarra, M. Koehn, J. L. Lehners and B. A. Ovrut, JCAP **1407**, 007 (2014) doi:10.1088/1475-7516/2014/07/007 [arXiv:1404.5067 [hep-th]].

[142] P. P. Avelino, C. J. A. P. Martins, C. Santos and E. P. S. Shellard, Phys. Rev. Lett. **89**, 271301 (2002) [Phys. Rev. Lett. **89**, 289903 (2002)] [astro-ph/0211066].

[143] Y. L. Bolotin, A. Kostenko, O. A. Lemets and D. A. Yerokhin, Int. J. Mod. Phys. D **24**, no. 03, 1530007 (2014) [arXiv:1310.0085 [astro-ph.CO]].

[144] L. P. Chimento, A. S. Jakubi, D. Pavon and W. Zimdahl, Phys. Rev. D 67, 083513 (2003);

[145] L. Amendola, Phys. Rev. D **62**, 043511 (2000) [arXiv:astro-ph/9908023].

[146] X. Zhang, Mod. Phys. Lett. A **20**, 2575 (2005) [arXiv:astro-ph/0503072].

[147] R. G. Cai and A. Wang, JCAP **0503**, 002 (2005) [arXiv:hep-th/0411025].

[148] Z. K. Guo, R. G. Cai and Y. Z. Zhang, JCAP **0505**, 002 (2005) [astro-ph/0412624].

[149] J. H. He, B. Wang and E. Abdalla, Phys. Lett. B **671**, 139 (2009) doi:10.1016/j.physletb.2008.11.062 [arXiv:0807.3471 [gr-qc]].

[150] Y. K. E. Cheung and J. D. Vergados, JCAP **1502**, no. 02, 014 (2015) doi:10.1088/1475-7516/2015/02/014 [arXiv:1410.5710 [hep-ph]].

[151] C. Li, R. H. Brandenberger and Y. K. E. Cheung, Phys. Rev. D **90**, no. 12, 123535 (2014) doi:10.1103/PhysRevD.90.123535 [arXiv:1403.5625 [gr-qc]].

[152] C. Li, arXiv:1512.06794 [astro-ph.CO].

[153] Y. K. E. Cheung, J. U. Kang and C. Li, JCAP **1411**, no. 11, 001 (2014) doi:10.1088/1475-7516/2014/11/001 [arXiv:1408.4387 [astro-ph.CO]].

[154] E. Poisson, *A Relativist?s Toolkit* (Cambridge University Press, Cambridge, England, 2004).

[155] I. Sawicki and A. Vikman, Phys. Rev. D **87**, no. 6, 067301 (2013) doi:10.1103/PhysRevD.87.067301 [arXiv:1209.2961 [astro-ph.CO]].

[156] A. Adams, N. Arkani-Hamed, S. Dubovsky, A. Nicolis and R. Rattazzi, JHEP **0610**, 014 (2006) doi:10.1088/1126-6708/2006/10/014 [hep-th/0602178].

[157] V. A. Rubakov, Phys. Usp. **57**, 128 (2014) [Usp. Fiz. Nauk **184**, no. 2, 137 (2014)] doi:10.3367/UFNe.0184.201402b.0137 [arXiv:1401.4024 [hep-th]].

[158] M. Parikh and J. P. van der Schaar, Phys. Rev. D **91**, no. 8, 084002 (2015) doi:10.1103/PhysRevD.91.084002 [arXiv:1406.5163 [hep-th]].

[159] A. Neronov and I. Vovk, Science **328**, 73 (2010) doi:10.1126/science.1184192 [arXiv:1006.3504 [astro-ph.HE]].

[160] S. Ando and A. Kusenko, Astrophys. J. **722**, L39 (2010) doi:10.1088/2041-8205/722/1/L39 [arXiv:1005.1924 [astro-ph.HE]].

[161] W. Essey, S. Ando and A. Kusenko, Astropart. Phys. **35**, 135 (2011) doi:10.1016/j.astropartphys.2011.06.010 [arXiv:1012.5313 [astro-ph.HE]].

[162] H. Tashiro, W. Chen, F. Ferrer and T. Vachaspati, Mon. Not. Roy. Astron. Soc. **445**, no. 1, L41 (2014) doi:10.1093/mnrasl/slu134 [arXiv:1310.4826 [astro-ph.CO]].

[163] W. Chen, B. D. Chowdhury, F. Ferrer, H. Tashiro and T. Vachaspati, Mon. Not. Roy. Astron. Soc. **450**, no. 4, 3371 (2015) doi:10.1093/mnras/stv308 [arXiv:1412.3171 [astro-ph.CO]].

[164] W. Chen, J. H. Buckley and F. Ferrer, Phys. Rev. Lett. **115**, 211103 (2015) doi:10.1103/PhysRevLett.115.211103 [arXiv:1410.7717 [astro-ph.HE]].

[165] J. D. Finke, L. C. Reyes, M. Georganopoulos, K. Reynolds, M. Ajello, S. J. Fegan and K. McCann, Astrophys. J. **814**, no. 1, 20 (2015) doi:10.1088/0004-637X/814/1/20 [arXiv:1510.02485 [astro-ph.HE]].

[166] A. Brandenburg and K. Subramanian, Phys. Rept. **417**, 1 (2005) doi:10.1016/j.physrep.2005.06.005 [astro-ph/0405052].

[167] R. Durrer and A. Neronov, Astron. Astrophys. Rev. **21**, 62 (2013) doi:10.1007/s00159-013-0062-7 [arXiv:1303.7121 [astro-ph.CO]].

[168] J. M. Wagstaff and R. Banerjee, JCAP **1601**, 002 (2016) doi:10.1088/1475-7516/2016/01/002 [arXiv:1409.4223 [astro-ph.CO]].

[169] T. Vachaspati, arXiv:1606.06186 [astro-ph.CO].

[170] A. Elyiv, A. Neronov and D. V. Semikoz, Phys. Rev. D **80**, 023010 (2009) doi:10.1103/PhysRevD.80.023010 [arXiv:0903.3649 [astro-ph.CO]].

[171] A. J. Long and T. Vachaspati, JCAP **1509**, no. 09, 065 (2015) doi:10.1088/1475-7516/2015/09/065 [arXiv:1505.07846 [astro-ph.CO]].

[172] R. Alves Batista, A. Saveliev, G. Sigl and T. Vachaspati, Phys. Rev. D **94**, no. 8, 083005 (2016) doi:10.1103/PhysRevD.94.083005 [arXiv:1607.00320 [astro-ph.HE]].

[173] A. E. Broderick, P. Tiede, M. Shalaby, C. Pfrommer, E. Puchwein, P. Chang and A. Lamberts, arXiv:1609.00387 [astro-ph.HE].

[174] T. Fitoussi, R. Belmont, J. Malzac, A. Marcowith, J. Cohen-Tanugi and P. Jean, doi:10.1093/mnras/stw3365 arXiv:1701.00654 [astro-ph.HE].

[175] H. Tashiro and T. Vachaspati, Phys. Rev. D **87**, no. 12, 123527 (2013) doi:10.1103/PhysRevD.87.123527 [arXiv:1305.0181 [astro-ph.CO]].

[176] B. Degrange and G. Fontaine, Comptes Rendus Physique **16** 587 doi:10.1016/j.crhy.2015.07.003 [arXiv:1604.05488 [astro-ph.HE]].

[177] H. Krawczynski and E. Treister, Front. Phys. (Beijing) **8**, 609 (2013) doi:10.1007/s11467-013-0310-3 [arXiv:1301.4179 [astro-ph.CO]].

[178] E. Massaro, P. Giommi, C. Leto, P. Marchegiani, A. Maselli, M. Perri, S. Piranomonte and S. Sclavi, Astron. Astrophys. **495** (2009) 691 doi:10.1051/0004-6361:200810161 [arXiv:0810.2206 [astro-ph]]

[179] A. Neronov and D. Semikoz, Phys.Rev. D80 (2009) 123012, arXiv:0910.1920.

[180] M. Ackermann *et al.* [Fermi-LAT Collaboration], Astrophys. J. Suppl. **222**, no. 1, 5 (2016) doi:10.3847/0067-0049/222/1/5 [arXiv:1508.04449 [astro-ph.HE]].

[181] M. Ackermann *et al.* [Fermi-LAT Collaboration], Phys. Rev. Lett. **116**, no. 15, 151105 (2016) doi:10.1103/PhysRevLett.116.151105 [arXiv:1511.00693 [astro-ph.CO]].

[182] N. Graham and K. D. Olum, Phys. Rev. D **76**, 064001 (2007) doi:10.1103/PhysRevD.76.064001 [arXiv:0705.3193 [gr-qc]].

APPENDIX A

GHOSTS IN CLASSICAL FIELD THEORY

In this appendix we will introduce the concept of ghost fields and discuss the issues of their presence in a theory. We will approach the question only from a classical point of view, namely we will not discuss the unitarity problems that they cause in a quantum mechanically setting. For such discussion we refer the reader to the review in [17]. Consider a scalar field theory containing N fields along with a given background $\tilde{\Phi}_i(\vec{x},t)$ where $i \in \{1,...,N\}$. We can write down an effective Lagrangian density for the perturbations $\phi_i = \Phi_i - \tilde{\Phi}_i$ which, to second order, takes the form,

$$\mathscr{L}^{(2)} = \frac{1}{2}U_{ij}\dot{\phi}^i\dot{\phi}^j - \frac{1}{2}V_{ij}\partial\phi^i\partial\phi^j - \frac{1}{2}W_{ij}\phi^i\phi^j, \tag{A.1}$$

and has a Hamiltonian density,

$$\mathscr{H} = \frac{1}{2}U_{ij}\dot{\phi}^i\dot{\phi}^j + \frac{1}{2}V_{ij}\partial\phi^i\partial\phi^j + \frac{1}{2}W_{ij}\phi^i\phi^j. \tag{A.2}$$

We have three matrices U,V,W and their properties will signal possible instabilities which we will now discuss. Note that if this is the whole system, the overall sign of the Lagrangian does not matter. Hence without loss of generality we will assume that at least one of the three matrices is positive definite. We will also simplify the discussion by asking that the matrices all have full rank as otherwise we'd need to find the non vanishing higher order terms of the Lagrangian to continue the discussion.

A healthy theory will have the three matrices U,V,W be of the same definiteness, i.e. all positive in our case. If either U,V or W fails to be positive definite there will exist instabilities called ghosts, gradient or tachyonic respectively. The failure of being positive definite implies the existence of at least one direction in field space which has negative eigenvalue and hence the Hamiltonian density (A.2) will be unbounded from below.

Gradient and ghost instabilities suggest something very wrong with the theory. This is not the case for tachyons, which arises when W is not positive definite but U,V are. As

an example consider a theory with one field expanded around $\tilde{\Phi} = 0$ giving $U = 1,\ V = 1$ and $W = \lambda < 0$. The Lagrangian density in Fourier space is,

$$\mathscr{L}_k^{(2)} = \frac{1}{2}\dot{\phi_k}^2 + \frac{1}{2}k^2{\phi_k}^2 - \frac{1}{2}\lambda\phi_k^2. \tag{A.3}$$

This is a well defined theory and the instability has a physical meaning that usually indicates the existence of a rapidly changing background. For long wavelength modes satisfying $k^2 < -\lambda$, we have a runaway solution $\phi_k(t) \sim e^{it\sqrt{\lambda+k^2}}$ meaning that perturbations will eventually grow large and the perturbation expansion around a specific background will lose its applicability. However as long as we focus on timescales shorter than $t_{inst} = 1/\sqrt{-\lambda}$ - which is the timescale of the fastest growing unstable mode - we are still in the perturbative regime and can get a sense of what the theory is doing.

On the other hand, a ghost instabilities does not offer us such luxury. Going back to the one field example but now with $U = \lambda < 0,\ V = 1$ and $W = m^2$, the Lagrangian becomes,

$$L = \frac{\lambda}{2}\dot{\phi_k}^2 + \frac{1}{2}k^2\phi_k^2 - \frac{m^2}{2}\phi_k^2. \tag{A.4}$$

By changing the sign of the kinetic term, we now find that the modes all have runaway solutions $\phi_k(t) \sim e^{it\sqrt{m^2+k^2}/\sqrt{\lambda}}$. This causes a problem because there is no timescale at which the theory stays in the perturbative regime, therefore there is no regime in which the perturbative expansion is applicable. A similar thing occurs for gradient instabilities, where $U = 1, V = \lambda < 0$ and $W = m^2$.

One might try to introduce a cutoff Λ on k and then argue that this is an effective field theory only defined for wavelengths smaller than Λ. Such a cutoff will introduce a lower bound on the timescale of instability. In such setting the fastest perturbations to become uncontrollably large only do so after some time akin to $t_{inst} \sim 1/(\Lambda\sqrt{-\lambda})$. Unfortunately, by imposing such cutoff we are also forbidding the theory to describe any phenomenon on any timescales shorter than the one defined by your smallest wavelength, namely t_{inst}. Hence the regime in which the EFT is defined is also the one in which it cannot be

perturbative. Hence this raises concern and confusion about the meaning of any calculation that is performed in such theories.

Our fear of ghosts can be summarized in the following way. The runaway behavior arises because it takes negative energy to excite a ghost mode. As we expect all field to be coupled to gravity and because quantum mechanics insures that the ghost fields cannot be set to vanish identically, a ghost field coupled to gravity will be able to explore any part of their phase space from an entropic point of view as exciting a mode k of each field cost 0 energy. If we have a cutoff Λ, then the phase space is not infinite and the time of instability is finite but any calculations cannot be trusted from our EFT viewpoint. If we do not have a cutoff, such as in a Lorentz Invariant theory, then the phase space is infinite and the theory blows up instantaneously.

APPENDIX B

THE RAYCHAUDURI EQUATION AND THE NEC

This Appendix illustrates how the Null Energy Condition (NEC) is required to be violated if one were to harbor wormhole solutions in General Relativity. We intend this section to be instructive to a reader unfamiliar with the subject but leave out most details and refer the interested party to the excellent book cited in [154].

The language of differential geometry is at the core of modern gravitation. In this paradigm, gravity is felt by test masses solely due to the properties of the manifold on which they reside. We attribute to the manifold the *spacetime* coordinates x_μ and keep track of the information regarding its local curvature through the metric $g_{\mu\nu}(t,x,y,z)$. A specific theory of gravity can be defined by an action such as the Einstein-Hilbert action 2.1 introduced in Chapter 1. The action allows us to determine the dynamical degrees of freedom in the metric and how they propagate. It also provides a description of how external matter affects the metric and hence affect the local properties of the manifold.

We wish to point out that one does not require an action to determine the behavior of geodesics of test particles. If one has a specific metric in hand and impose the requirement of a symmetric and metric compatible connection (i.e. the connection is chosen to be the *Christoffel symbols*), one can reconstruct the local geometry of the manifold which completely fixes the geodesics. Consider a particle moving with four momentum $k^\mu = \frac{dx^\mu}{d\lambda}$ for some parametrization λ of its trajectory, the geodesic equation is then,

$$k^\alpha \nabla_\alpha k^\mu = \kappa k^\mu, \tag{B.1}$$

where $\kappa = d\ln L/d\lambda$ with L being the Lagrangian of our test particle. In general, one can find a reparametrization λ^* such that $\kappa = 0$. We call these λ^*'s *affine* parameters and we shall assume such parametrization choice from now on as it simplifies the geodesic equation.

Consider two geodesics γ_0 and γ_1 who are describe by the same affine parameter λ and have coordinates $x^\mu(\lambda,s)$. Here we've introduced the parameter $s \in [0,1]$ which labels a

continuous family of curves which interpolates between γ_0 and γ_1 whose curves are labeled by the values $s \in \{0,1\}$. We define the tangeant vector of this family as $\xi^\alpha = \partial x^\alpha / \partial s$ and tune it so that it is orthogonal to our first geodesic, i.e. $\xi^\alpha k_\alpha|_{s=0} = 0$. One can then show that the acceleration of this vector at $s = 0$ is,

$$k^\mu \nabla_\mu (k^\mu \nabla_\mu \xi^\alpha) = -R^\alpha_{\zeta\rho\sigma} k^\zeta \xi^\rho k^\sigma. \tag{B.2}$$

This is called the *geodesic deviation equation* and shows how the curvature (through the Riemann tensor) can impact the behavior of neighboring geodesics by creating a relative acceleration between them.

This relative acceleration leads to interesting conclusions. Consider the expansion scalar $\theta = \nabla_\alpha k^\alpha$, which represents the fractional rate of change in the cross section of a congruence of geodesics. Namely,

$$\theta = \frac{1}{\delta V}\frac{d}{d\lambda}\delta V \quad \text{for timelike geodesics,} \tag{B.3}$$

$$\theta = \frac{1}{\delta A}\frac{d}{d\lambda}\delta A \quad \text{for null geodesics,} \tag{B.4}$$

where difference between the null and timelike cases arises because the cross-section of a bundle of null geodesic is only two dimensional as there is no rest frame. If one uses coordinates in which the geodesic congruence is hypersurface orthogonal, a lengthy calculations shows that,

$$\frac{d\theta}{d\lambda} = -\frac{1}{p}\theta^2 - \sigma^{\alpha\beta}\sigma_{\alpha\beta} - R_{\alpha\beta}k^\alpha k^\beta. \tag{B.5}$$

Here $p = 2$ or $p = 3$ for null and timelike geodesics respectively, and σ is the shear tensor. The equations for $\frac{d\theta}{d\lambda}$ are called the Raychaudhuri equations, the overall sign of the right hand side describes whether the underlying manifold confers an attractive or repulsive attraction between the geodesics. For instance, a congruence of light rays passing through a wormhole would initially have a negative expansion scalar θ as they are approaching the throat, however once through the sign of θ must change to prohibit them from meeting at

a single point, causing a caustic and a hence a singularity. A wormhole would then require $\frac{d\theta}{\lambda} > 0$ as a minimal condition for θ to flip sign from negative to positive. A look at the Raychaudhuri equations shows that the first two terms are the negatives of a squared quantity, hence the only chance for $\frac{d\theta}{\lambda} > 0$ to be satisfied is if

$$R_{\mu\nu}k^{\mu}k^{\nu} < 0. \tag{B.6}$$

This imposes a condition on the Ricci scalar. To go further we must introduce a specific theory of gravity, so let us consider GR and null geodesics (the same argument with timelike geodesics imposes even stronger conditions). In GR the EOM for the metric are the Einstein equations,

$$R_{\mu\nu} - \frac{1}{2}Rg_{\mu\nu} = \frac{1}{M_p^2}T_{\mu\nu}. \tag{B.7}$$

Dotting these with $k^{\mu}k^{\nu}$ we find,

$$R_{\mu\nu}k^{\mu}k^{\nu} = \frac{1}{M_p^2}T_{\mu\nu}k^{\mu}k^{\nu}. \tag{B.8}$$

The condition B.6 would require matter that satisfies

$$T_{\mu\nu}k^{\mu}k^{\nu} < 0. \tag{B.9}$$

The opposite of this, namely the condition that $T_{\mu\nu}k^{\mu}k^{\nu} > 0$ for any future-pointing null vector k^{ν} is called the Null Energy Condition (NEC). Hence within the context of GR, wormhole solutions (and by the same arguments, bouncing solutions) requires a type of matter that violates the NEC. This requirement cast doubts on the existence of such solutions as all known classical matter satisfies the some form of the NEC. Quantum fluctuations which violates the condition have been observed (Casimir fluctuations are an example) however these only do so for short moments and still satisfies a time averaged version of the NEC [182].

What would a theory violating the NEC look like? One can easily construct an example using a scalar field with the wrong sign for its kinetic energy,

$$\mathscr{L} = -\frac{1}{2}\left(\frac{d\varphi}{dt}\right)^2 - V(\varphi). \tag{B.10}$$

This has energy $\rho = -\frac{1}{2}\left(\frac{d\varphi}{dt}\right)^2 + V(\varphi)$ and pressure $p = -\frac{1}{2}\left(\frac{d\varphi}{dt}\right)^2 - V(\varphi)$ so that $\rho + p = -\left(\frac{d\varphi}{dt}\right)^2 < 0$. However as discuss in appendix 5.5, such theory contains a ghost and hence cannot describe anything meaningful. It is possible that any theory capable of a classical violation of the condition would bring pathologies such as ghosts, negative energy densities [155] or superluminal propagation signaling an issue with the theory in the UV [156]. Nevertheless there are have been many attempts to build field theories that might violate the NEC but do not suffer from any glaring issues. The galileons might have succeeded in doing so and a nice review of some current constructions can be found in [157]. It is beyond the scope of this thesis to explore these possibilities and their critiques in further details, but see [74, 158] for an additional point of view on the subject.

APPENDIX C

PROBING STOCHASTIC INTER-GALACTIC MAGNETIC FIELDS USING BLAZAR-INDUCED GAMMA RAY HALO MORPHOLOGY

Inter-galactic magnetic fields can imprint their structure on the morphology of blazar-induced gamma ray halos. We show that the halo morphology arises through the interplay of the source's jet and a two-dimensional surface dictated by the magnetic field. Through extensive numerical simulations, we generate mock halos created by stochastic magnetic fields with and without helicity, and study the dependence of the halo features on the properties of the magnetic field. We propose a sharper version of the Q-statistics and demonstrate its sensitivity to the magnetic field strength, the coherence scale, and the handedness of the helicity. We also identify and explain a new feature of the Q-statistics that can further enhance its power.

C.1 Introduction

Multiple analyses of observed gamma rays [159, 160, 161, 162, 163, 164, 165] provide growing evidence for the existence of inter-galactic magnetic fields (for reviews see [166, 167]). The existence of such magnetic fields poses new questions for cosmology and probably also for particle physics [168, 169]. In addition, a primordial magnetic field can play an important role during structure formation in the universe and could help us understand the ubiquity of magnetic fields in astrophysical bodies.

A critical challenge at this stage is to sharpen observational techniques so that we can better observe and measure inter-galactic magnetic fields. Of the various probes of inter-galactic magnetic fields, blazar-induced gamma ray cascades hold certain key advantages. The gamma ray cascades originate in the voids in the large-scale structure and are mostly immune to complications of a noisy environment. The cascade develops in a relatively small spatial volume and hence is a local probe of the magnetic field in the voids. This is distinct from other methods, such as the Faraday rotation of the cosmic microwave background polarization, that probe an integrated measure of the magnetic field. Gamma

ray cascades are also highly sensitive probes and can trace very weak cosmological magnetic fields.

In this paper we study the effect of stochastic inter-galactic magnetic fields on blazar induced gamma ray halos and some results overlap with those of Refs. [170, 171, 172, 173, 174]. The cascade process is complicated and all analyses use some simplifying assumptions. For example, the analysis in Ref. [171] only considered non-stochastic magnetic field configurations. Other simplification schemes, such as the "large spherical observer" method employed in Ref. [172], transport arrival directions of gamma rays for distant observers to a single Earth-bound observer. This technique is certainly useful to study spectral properties of the cascade, but there is a danger that it loses or shuffles the spatial information of gamma ray arrival directions that is crucial for morphological studies. Our focus is on the effect of stochastic magnetic fields that are statistically isotropic and with or without helicity. So we carefully analyse the spatial information of the gamma rays that is useful for deducing properties of the magnetic field but, for the present, we only include an approximate description of the cascade development.

An important helpful concept that we develop in this paper is that of the "PP surface" (see Sec. C.4). This spatial surface holds the key to halo morphology and many of the features that we see in our simulations can be understood in terms of the shape of the PP surface and its intersection with the blazar jet.

We have applied a refined version of the Q-statistics first proposed in Ref. [175] to study the morphology of halos. Our results show that this statistic can successfully extract the helicity of the magnetic field. Our simulations also reveal that the plot of $Q(R)$, where R is a variable that will be explained below, has an additional bump. We are able to show that this bump is a genuine feature of the Q-statistic and explain it in terms of properties of the PP surface in Sec. C.8. Thus this extra feature of $Q(R)$ may become an observational

tool in future.

We give some background information in Sec. C.2 and C.3, discuss our simulation techniques in Sec. C.4, discuss features of the halo in Sec. C.5, introduce the Q-statistic in Sec. C.6 and apply it to stochastic fields in Sec. C.7. As mentioned above, we discuss the bump feature in $Q(R)$ in Sec. C.8. We summarize our conclusions in Sec. C.10. Our stochastic magnetic field generation scheme is described in Appendix C.9.

C.2 Astrophysical Sources of High Energy Photons

Before we delve deeper into the details of halo formation mechanism, we will briefly review the astrophysical objects that emits high energy photons and are considered point sources. The TeV photons from these sources induce electromagnetic cascades through pair production with the extragalactic background light, $\gamma_{\rm EBL}\,\gamma_{\rm TeV} \to e^+e^-$. In the presence of a magnetic field, the charged leptons follow spiral paths as they propagate and lose energy due to inverse Compton scattering with the cosmic microwave background (CMB) photons. The up-scattered CMB photons have gamma ray energies and produce extended halos around the direction of the sources.

As the initial TeV photons propagates over hundreds of Mpc before pair producing leptons, we will be interested in extragalactic sources. This makes Active Galactic Nuclei (AGN) as our prime candidate sources [176], these are luminous objects found at the center of a galaxy and thought to be accreting supermassive blackholes of mass anywhere from 10^6 to $10^{10}M_\odot$ [177]. The term AGN was coined after astronomical accuracy improved in a way that allowed astronomers to discover that many luminous sources, which appeared to have different properties, originated from objects found at the center of galaxies. Hence the nomenclature of AGN classes has its root in the historical discovery of objects in that class. Example of AGN includes Seyfert galaxies, QSO (Quasi-Stellar Object), Radio galaxies

and quasars. The most luminous class are the quasars, the name originated from a contraction of "quasi-stellar radio source" as they were first discovered as powerful radio emitters. These quasars may or may not have relativistic jets, however whenever they do and Earth finds itself in the line of sight (LoS), we call the objects blazars. Having these sources' jet point in our direction allow us easily detect the blazars positions. In the next section we review how the collimated TeV photons being emitted along the jets LoS give rise to secondary γ emissions which are responsible for the formation of halo. Although the latest update (January 2015) of the Roma BZCAT features 3561 observed blazars [178], no detection of these halos have been found within the precision of the observations. However there were indirect detection of the secondary emissions which enabled to impose lower bound constraints on the strength of the IGMF [159].

C.3 Blazar Halos From an Intergalactic Magnetic Field

As previously stated, here we briefly discuss the formation of the halo under simplifying assumptions. Consider a blazar located at the origin of our coordinate system described by the unit basis vectors $\hat{\mathbf{x}}, \hat{\mathbf{y}}, \hat{\mathbf{z}}$. We choose $\hat{\mathbf{z}}$ so that Earth is located at $\mathbf{r}_{\rm E} = -d_s\hat{\mathbf{z}}$ where d_s is the comoving distance to the source,

$$d_s = \frac{1}{a_0 H_0}\int_0^{z_s} \frac{1}{\sqrt{\Omega_m(1+z)^3+\Omega_\Lambda}}dz \simeq \frac{z_s}{0.22}\text{Gpc}. \tag{C.1}$$

To perform the integral, we have used $\Omega_\Lambda \approx 0.69$, $\Omega_m \approx 0.31$, $H_0 \approx 0.67h$ as found in Ref. [58] and we have also assumed that $z_s \ll 1$ and used natural units so that $c = 1$. For all the simulations in this paper we will choose $d_s = 1$ Gpc.

The blazar will typically emit photons in a collimated jet which we approximate to be a conical region with half-opening angle $\theta_{\rm jet} \approx 5^\circ$. The energy $E_{\gamma 0}$ of these photons must lie above some threshold of about a TeV if they are to produce an electron-positron pair from interaction with the Extragalactic Background Light (EBL). Due to the opacity

of the EBL, the TeV photons will travel a mean free path (MFP) determined by the pair production cross section $\sigma_{\gamma\gamma}$ and the number density of the EBL photons $n_{\rm EBL}$,

$$D_{\gamma 0} = \langle \sigma_{\gamma\gamma} n_{\rm EBL} \rangle^{-1} \simeq (80{\rm Mpc}) \frac{\kappa}{(1+z_{\gamma\gamma})^2} \Big(\frac{10{\rm TeV}}{E_{\gamma 0}} \Big), \tag{C.2}$$

We have assumed that $n_{\rm EBL} \propto (1+z_{\gamma\gamma})^{-2}$ to approximate the MFP in the final equality [179]. Following [171] we will set $\kappa = 1$ as this dimensionless constant is estimated to lie in the range of $0.3 < \kappa < 3$. The comoving distance from the source to the pair production event is given by $D^c_{\gamma 0} = (1+z_{\gamma\gamma}) D_{\gamma 0}$.

The redshift of the produced lepton pairs will depend on the relative position of the leptons to the source. Since $D^c_{\gamma 0} \ll d_s$, we make the approximation $z_{\gamma\gamma} \approx z_s$ and we can write,

$$D^c_{\gamma 0} \simeq (80{\rm Mpc}) \frac{\kappa}{(1+z_s)} \Big(\frac{10{\rm TeV}}{E_{\gamma 0}} \Big). \tag{C.3}$$

The energy of each of the produced leptons will be $E_e \approx E_{\gamma 0}/2$. These leptons are expected to travel a distance D_e before losing most of their energy through inverse Compton (IC) cooling which occurs by upscattering CMB photons. The cooling distance is

$$D_e = \frac{3 m_e^2}{4 \sigma_T U_{CMB} E_e} \simeq (31 \text{ kpc}) \Big(\frac{5 \text{ TeV}}{E_e} \Big) \Big(\frac{1.22}{1+z_{\gamma\gamma}} \Big)^4 \tag{C.4}$$

where $\sigma_T = 6.65 \times 10^{-25} {\rm cm}^2$ is the Thomson scattering cross section and $U_{CMB}(z_{\gamma\gamma}) \simeq (0.26 \text{ eV/cm}^3)(1+z_{\gamma\gamma})^4$ is the CMB energy density. Note that we can assume the whole cascade development happens around redshift $z_{\gamma\gamma}$ as $D_e \ll D_{\gamma 0}$. At that redshift, the average energy of a CMB photon is

$$E_{CMB} \simeq (6 \times 10^{-4} \text{ eV})(1+z_{\gamma\gamma}), \tag{C.5}$$

which implies that, from energy conservation, the upscattered photons will have energy

$$E_\gamma = \frac{4}{3} E_{CMB} \frac{E_e^2}{m_e^2} \simeq (77 \text{ GeV}) \Big(\frac{E_{\gamma 0}}{10 \text{ TeV}} \Big)^2. \tag{C.6}$$

As the lepton propagates, it upscatters $\approx (10\text{TeV})/(10\text{GeV}) \sim 10^3$ photons, and produces a gamma ray cascade in the 1-100 GeV range if the initial gamma ray had an energy of a few TeV. Clearly not every photon upscattered by the leptons will reach Earth. Those that do must come from a set of events that satisfy a set of three constraints given in Ref. [171] that we now describe.

After pair production, the lepton's initial velocity will be almost parallel to the momentum of the parent photon with a negligible deviation of order the inverse Lorentz boost factor $m_e/E_e \sim 10^{-6}$. Their subsequent trajectory will be determined by the magnetic field $\mathbf{B}(\mathbf{x})$ through the Lorentz force. If the magnetic field is incoherent on length scales smaller than the cooling distance $D_e \sim 30$ kpc, the lepton trajectories will be diffusive and this situation is much harder to analyze. So we focus on magnetic fields that are coherent on scales that are much larger than D_e. Then the lepton trajectories are bent in an effectively constant magnetic field and follow a helical trajectory with gyroradius

$$R_L = R_{L0}|\mathbf{v}_\perp|, \quad \text{with } R_{L0} = \frac{E_e}{e|\mathbf{B}|}, \tag{C.7}$$

which depends on the lepton's perpendicular velocity to $\mathbf{B}$, *i.e.* $\mathbf{v}_\perp = \mathbf{v} - (\mathbf{v}\cdot\hat{\mathbf{B}})\hat{\mathbf{B}}$.

The quantity $2\pi R_{L0}$ is useful as it denotes the distance the lepton must travel in order to perform a full revolution. The value of R_{L0} is a function of the redshift as it depends on $|\mathbf{B}|$. For magnetic fields frozen in the plasma, the field strength redshifts as $|\mathbf{B}| = B_0(1+z_{\gamma\gamma})^2 \approx B_0(1+z_s)^2$ where B_0 is the magnetic field magnitude today. With

$$R_{L0} \simeq 3.5 \text{ Mpc } \left(\frac{E_e}{5 \text{ TeV}}\right)\left(\frac{B_0}{10^{-15}G}\right)^{-1}\left(\frac{1+z_s}{1.22}\right)^{-2}, \tag{C.8}$$

we can evaluate the ratio

$$\frac{D_e}{2\pi R_{L0}} \simeq 0.0106 \left(\frac{E_\gamma}{10 \text{ GeV}}\right)^{-1}\left(\frac{B_0}{10^{-15}G}\right)\left(\frac{1+z_s}{1.22}\right)^{-2} \tag{C.9}$$

which determines the angular deflection of the leptons.

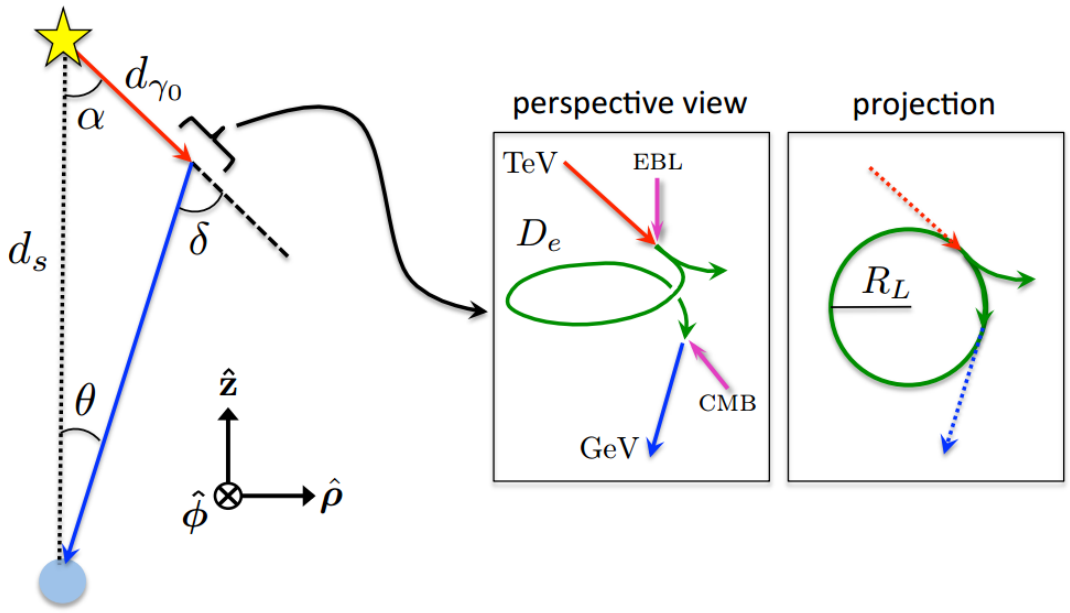

Figure C.1: A TeV photon emitted from a blazar travels a comoving distance of $d_{\gamma 0}$ before scattering off an EBL photon and pair producing leptons. The lepton trajectories are bent due to the local magnetic field over a very short distance compared to the distance to the source, d_s, and are shown in the insets. (The insets show huge bending whereas we have only considered magnetic fields that give small bending.) Inverse-Compton scattering of a lepton and CMB photons results in a cascade of GeV energy gamma rays arriving at Earth from the direction of the pair production. [Sketch taken from [171].]

As depicted in Fig. C.1, let us introduce the following angles: θ is the arrival angle of the GeV photon with respect to the source location, δ represents the angle between the upscattered photon and the TeV photon, α is the angle subtended by the TeV photon's momentum, $\mathbf{r}_E$ the vector from the source to Earth, and finally ϕ is the azimuthal angle in which the whole (planar) scattering process take place. We also introduce the polar vectors $\hat{\boldsymbol{\rho}}$ and $\hat{\phi}$, in the $\hat{\mathbf{x}}, \hat{\mathbf{y}}$ plane. It is important to emphasize that the whole process occurs in a plane to a good approximation because $D_e \ll D^c_{\gamma 0}, d_s$ and the length of the lepton trajectory can be ignored. Then there are only 3 points that are relevant (the source, the pair production point, and the observer) and they always lie in a plane.

Applying the sine formula to the triangle in Fig. C.1 we get our first constraint

$$d_s \sin(\theta) = d_{\gamma 0} \sin(\delta). \tag{C.10}$$

where $d_{\gamma 0}$ is the distance traveled by the TeV photon and is a random variable drawn from a distribution that depends on the MFP $D^c_{\gamma 0}$ in Eq. (C.3). This is discussed in detail in Sec. C.4.

The bending angle δ is related to the distance traveled by the lepton through the local magnetic field which we write as $\mathbf{B} = B\hat{\mathbf{n}}_{||}$. We also decompose the lepton's initial velocity at time $t_i = 0$, $\mathbf{v}(t_i = 0) = v_{||}\hat{\mathbf{n}}_{||} + v_\perp \hat{\mathbf{n}}_\perp$, where $\hat{\mathbf{n}}_\perp \cdot \hat{\mathbf{n}}_{||} = 0$. At some later time t the velocity is

$$\mathbf{v}(t) = v_{||}\hat{\mathbf{n}}_{||} + v_\perp \cos(\omega t)\hat{\mathbf{n}}_\perp \pm v_\perp \sin(\omega t)(\hat{\mathbf{n}}_\perp \times \hat{\mathbf{n}}_{||}), \tag{C.11}$$

Here we introduced the angular frequency of the orbital motion $\omega = v_\perp / R_L = 1/R_{L0}$ and the $+$ $(-)$ sign refers to the positron (electron) trajectory. A CMB photon upscattered at time t_{IC} will be directed along the lepton's trajectory and so the deflection angle of Figure C.1 can be expressed as $\cos(\delta) = \hat{\mathbf{v}}(0) \cdot \hat{\mathbf{v}}(t_{IC})$. Using Eq. (C.11) we can derive the second constraint,

$$1 - \cos(\delta) = \Big(1 - (\hat{\mathbf{v}}(0) \cdot \hat{\mathbf{B}})^2\Big)\Big(1 - \cos(t_{IC}/R_{L0})\Big). \tag{C.12}$$

The time of inverse Compton scattering t_{IC} is a stochastic variable. Given its value and the magnetic field direction, the constraints determine the bending angle, δ.

A single propagating lepton will be able to upscatter CMB photons towards Earth only at certain times when the lepton's momentum is directed towards Earth. Photons upscattered at other times will not reach Earth and we can safely ignore them. The number of photons upscattered by a lepton is very large ($\sim 10^3$), with mean deviation angles between the photons $\sim 10^{-3} \times 0.01$ (see Eq. (C.9)). This angle is large enough that we only expect ~ 1 of the cascade photons from any lepton to reach Earth. This allows us to adopt the strategy that we first select a value of t_{IC} from an exponential probability distribution as

described in Sec. C.4 and then solve the constraint equations to find all TeV gamma rays from the blazar that upscatter CMB photons that reach Earth. For different values of t_{IC}, different TeV gamma rays from the blazar will lead to observed photons. In this way, we will be able to track the photons that arrive on Earth and not waste computational effort on those that go elsewhere.

The third and final constraint is that the cascade gamma ray lies in the plane specified by $\hat{\phi}$. This requires that the Lorentz force in the azimuthal $\hat{\phi}$ direction vanishes between the time of pair production and IC scattering. Namely the ϕ component of the impulse must vanish,

$$J_\phi = \hat{\phi} \cdot \mathbf{J} = \hat{\phi} \cdot \left(\pm e \int_0^{t_{IC}} dt\ \mathbf{v}(t) \times \mathbf{B} \right) = 0. \tag{C.13}$$

The impulse can be simplified by pulling out the assumed constant magnetic field of the integral and defining

$$\mathbf{v}_{\text{avg}} = \frac{1}{t_{IC}} \int_0^{t_{IC}} dt\ \mathbf{v}(t). \tag{C.14}$$

The geometrical setup of Fig. C.1 forces $\mathbf{v}_{\text{avg}}$ to bisect the angle δ and therefore its unit vector can be written as

$$\hat{\mathbf{v}}_{\text{avg}} = \sin\big(\delta/2 - \theta\big)\hat{\boldsymbol{\rho}} - \cos\big(\delta/2 - \theta\big)\hat{\mathbf{z}}. \tag{C.15}$$

Decomposing $\mathbf{B}$ as

$$\mathbf{B} = b_\rho \hat{\boldsymbol{\rho}} + b_\phi \hat{\phi} + b_z \hat{\mathbf{z}} \tag{C.16}$$

allows us to write

$$\hat{\phi} \cdot \hat{\mathbf{v}}_{\text{avg}} \times \hat{\mathbf{B}} = -b_\rho \cos\big(\delta/2 - \theta\big) - b_z \sin\big(\delta/2 - \theta\big) = 0. \tag{C.17}$$

To summarize this section, Eqs. (C.10), (C.12) and (C.17) are the constraints that need to be satisfied by the variables (θ, δ, ϕ) given a magnetic field realization and initial velocity of the TeV gamma ray (both of which depend on (θ, δ, ϕ)), the source-observer distance (d_s), the distance to pair production ($d_{\gamma 0}$), and the photon upscattering time (t_{IC}).

C.4 Halo Simulations

For events that satisfy the constraints in Eqs. (C.10), (C.12) and (C.17), an observer on Earth will receive flux at a polar angle of θ from the line of sight to the blazar and at an azimuthal angle ϕ. Solving these constraints requires the use of numerical methods when considering general $\mathbf{B}(\mathbf{x})$ and when including the stochasticity in the propagating distances (PDs) of the initial gamma ray and pair produced leptons.

Therefore to simulate one observed photon, we supply the distance $d_{\gamma 0}$ traversed by some TeV gamma ray of energy $E_{\gamma 0}$ emitted from the source before it pair produces leptons, one of which in turn travels a distance ct_{IC} before emitting a photon of energy E_γ. Once these 4 values $d_{\gamma 0}$, $E_{\gamma 0}$, ct_{IC} and E_γ, are set and an ambient magnetic field is given, one can numerically solve the constraint equations for θ, δ and ϕ. The process is repeated until N (which we chose to be 1000 or 5000 per simulation) observed photons are simulated. This will create the halo that one would observe if the source was emitting isotropically. For a source with a specific jet orientation we only retain the events whose initial TeV photons lie within the jet. These small number of events give us the observed halo that will be shown in our plots.

Let us go through the details regarding the generation of $d_{\gamma 0}$, $E_{\gamma 0}$, ct_{IC} and E_γ. We must supply some energy distribution for gamma rays emitted by blazars; for this we assume a power law spectrum [180, 181] and follow Ref. [173] by choosing a spectral index of $\Gamma \simeq 2.5$ that is characteristic of the TeV sources. This yields a spectrum given by,

$$\frac{dN_{\gamma 0}}{dE_{\gamma 0}} \sim \left(\frac{E_{\gamma 0}}{\text{TeV}}\right)^{-2.5}. \tag{C.18}$$

We shall also impose a 10 TeV cutoff on the emitted photon energy. The distance $d_{\gamma 0}$ traversed by a TeV gamma ray before turning into a pair of leptons is drawn from the

exponential distribution,

$$P[d_{\gamma 0}] = \frac{1}{D^c_{\gamma 0}(E_{\gamma 0})} e^{-d_{\gamma 0}/D^c_{\gamma 0}(E_{\gamma 0})}. \tag{C.19}$$

The resulting leptons will have energies E_e given by Eq. (C.6) and they will upscatter numerous CMB photons along their trajectories. The mean free path between each scattering is given by $l_{\rm MFP} = (n_{CMB}\sigma_T)^{-1}$, where n_{CMB} is the number density of CMB photons. The lepton loses energy with each scattering and subsequent scatterings lead to lower energy cascade gamma rays. Hence we run Monte Carlo simulations to determine the distributions $P(ct_{IC}, E_\gamma | E_e^{(\rm ini)})$, giving us the probability that a lepton with initial energy $E_e^{(\rm ini)}$ upscatters a CMB photon to energy E_γ after traveling a distance $d_e = ct_{IC}$. Examples of these distributions are shown in Fig. C.2. Note that d_e will generally be much smaller than the cooling distance D_e. Only events that lead to observed photons of energy between $E_{\rm min} = 5$ GeV and $E_{\rm max} = 50$ GeV will be retained as these are in energies of observational interest for the statistical analysis done in Sec. C.6.

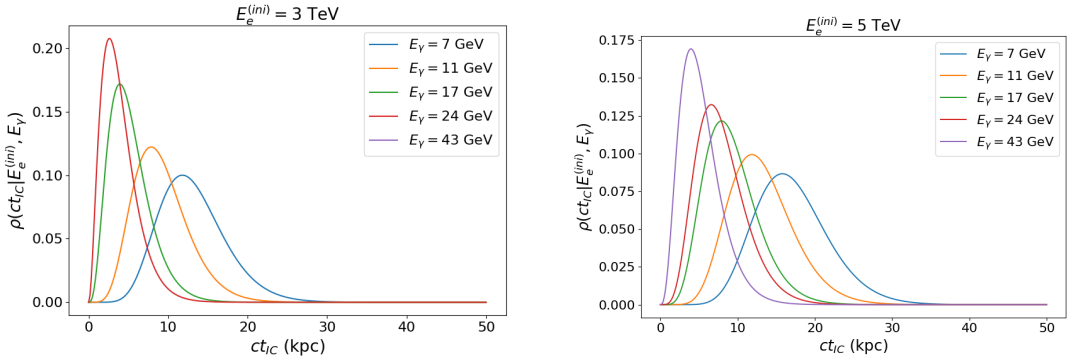

Figure C.2: Examples of the probability distribution for the distance traveled by leptons of initial energy $E_e = E_{\gamma 0}/2$ before it upscatters a CMB photon to E_γ. These distributions are for leptons evolving in the CMB light at a redshift of $z \approx 0.24$, corresponding to a source located at $d_s \approx 1$ Gpc from Earth. Note that the final distribution for $E_\gamma = 43$ GeV does not appear on the left as the lepton does not possess enough energy to upscatter the CMB photons to these energies.

We will solve the constraint equations in a variety of magnetic field backgrounds, starting with simple analytic configurations for illustration purposes, and then move on to

the more realistic case of stochastic, isotropic magnetic fields. Our procedure to generate stochastic, isotropic magnetic fields is described in Appendix C.9.

As a warm up, and to compare our method with the results of Ref. [171], we consider a source that radiates TeV photons isotropically in two different magnetic field backgrounds. The first background,

$$\mathbf{B} = B_0\Big(\cos(\beta)\hat{\mathbf{y}} - \sin(\beta)\hat{\mathbf{z}}\Big), \tag{C.20}$$

with $\beta = \pi/4$, is a uniform magnetic field pointing at an angle $\pi/4$ from the line of sight. The second background is a maximally helical field

$$\mathbf{B} = B_0\Big(\sin(2\pi z/\lambda)\hat{\mathbf{x}} + \cos(2\pi z/\lambda)\hat{\mathbf{y}}\Big). \tag{C.21}$$

Here λ is the coherence length of the helical field. We will take $d_s = 1$ Gpc, $B_0 = 10^{-14}$ G and $\lambda = 500$ Mpc as the prototypical values and eventually vary them one at a time to see their effect on the halo morphology.

Next we solve the constraint equations and determine the arrival directions θ, ϕ for several different energies E_γ, for an isotropically emitting source. The points located further away from the source direction usually corresponds to lower energy photons. This is expected since leptons that travel long distances (and hence allow for a large bending angle) will have already lost a lot of energy and upscatter less energetic photons. This behavior can be seen from the distribution shown in Fig C.2.

We show halos for the simple field configurations of Eqs.(C.20) and (C.21) in Fig. C.3. Looking closely at Fig. C.3, the drawn points are triangular; upright triangles are gamma rays that originate from electrons and inverted triangles are those that originate from positrons. The distinction is made clearer in Fig. C.4 where red (black) points originate from positron (electron) processes. If the source was taken to be a jet, gamma rays predominantly from one of the two leptons will be observed.

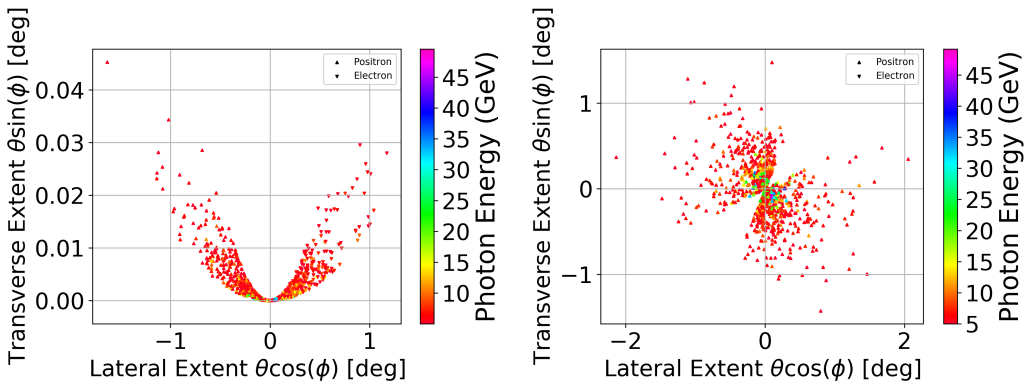

Figure C.3: Example of halos from blazars in a uniform (left) and maxially helical (right) inter-galactic magnetic field as given in Eqs. (C.20) and (C.21). The colors denote the energy of the observed gamma ray.

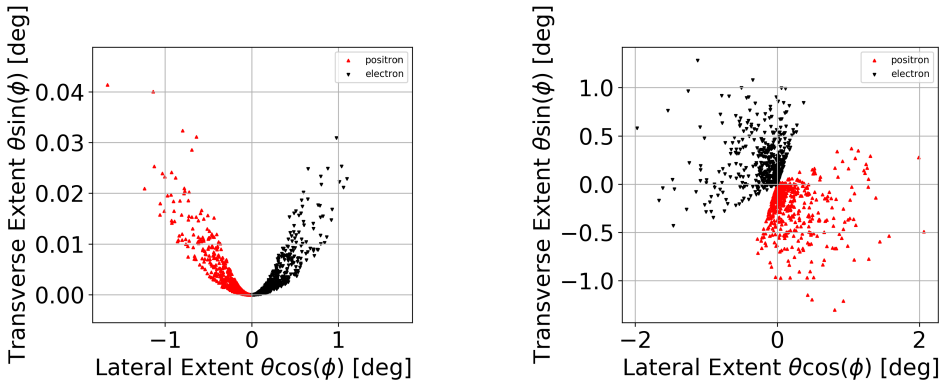

Figure C.4: Same as in Fig. C.3 but now red (black) points originate from inverse Compton scattering due to positrons (electrons). If the source was taken to emit along a jet, most of the observed gamma rays would originate from either positron or electron processes but not both.

The constraint equations are quite complicated to solve but there is a helpful visualization. First consider the third constraint equation, Eq. (C.17), and note that b_ρ and b_ϕ are also functions of θ, δ and ϕ. So Eq. (C.17) provides one functional relation between these variables that only depends on the magnetic field background. Hence the magnetic field defines a two-dimensional surface in space. We will call this the "Pair Production surface" or the "PP surface" since only lepton pair production at this surface can send GeV gamma rays to the observer. In Fig. C.5 we show the PP surface for the magnetic fields of Eqs. (C.20) and (C.21). On these plots we also show the pair production locations, "PP

locations", that resulted in the halos of Fig. C.3. Note that a gamma ray from the source will propagate a certain distance, $d_{\gamma 0}$ and then pair produce. So the pair production points also lie on a sphere of radius $d_{\gamma 0}$. This is partly enforced by the law of sines in Eq. (C.10), which gives a relation between δ and θ. The intersection of this sphere and the PP surface define a one-dimensional curve in space; CMB photons that are inverse Compton scattered along the one-dimensional curve can propagate to Earth. However, not all points on this one-dimensional curve will satisfy the final constraint. Namely, Eq. (C.12), picks out a limited set of points on the one-dimensional curve and these give the trajectories of the gamma rays that are observed.

The PP surface can be found analytically for simple cases. For instance, the constraint in Eq. (C.17) with the helical magnetic field from Eq. (C.21), which has $b_z = 0$, reduces to,

$$b_\rho \cos(\delta/2 - \theta) = 0, \tag{C.22}$$

with

$$b_\rho = \boldsymbol{B} \cdot \hat{\boldsymbol{\rho}} = \sin(2\pi z/\lambda + \phi). \tag{C.23}$$

As $\cos(\delta/2 - \theta) = 0$ has only one solution at $\delta = \pi,\ \theta = 0$ in the physical range $\theta \in [0, \pi/2]$, $\delta \in [0, \pi]$, the surface is mainly determined by $b_\rho = 0$ which translates to,

$$\phi = -\frac{2\pi z}{\lambda}. \tag{C.24}$$

This equation describes a spiral structure as seen in Figure C.5.

Until now, we have been assuming that the source emits photons isotropically. Below, we will also consider the case when the source emits photon in a collimated jet. In that case, there is a fourth constraint restricting the relevant part of the PP surface to where it intersects the jet, and it is quite possible that there is no solution. We ignore such cases as they are observationally irrelevant. In following figures we will show PP locations, even if they do not lie within the jet. Only those PP locations that lie within the jet will lead to

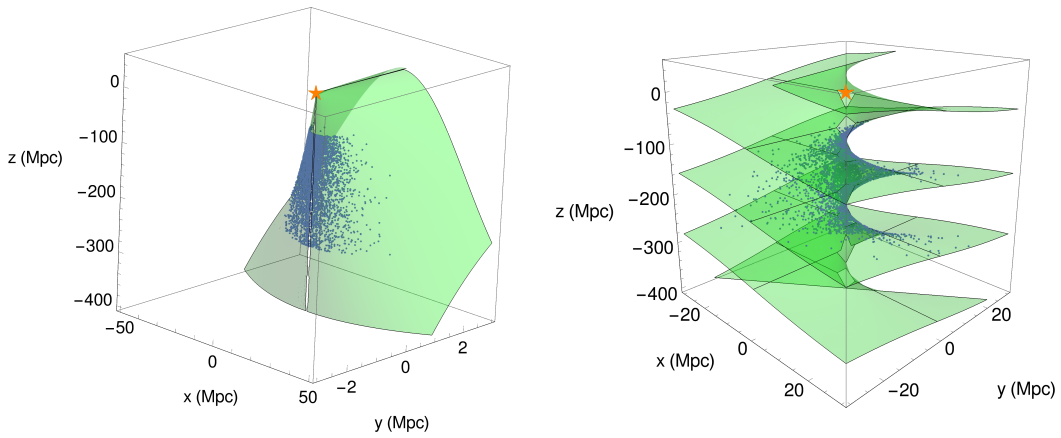

Figure C.5: The PP surface for the uniform magnetic field of Eq. (C.20) (left) and the maximally helical magnetic field of Eq. (C.21) (right). The source is located at the orange star; the observer is at $z = -1$ Gpc. The blue points are the events that give rise to the halos shown in Figs. C.3.

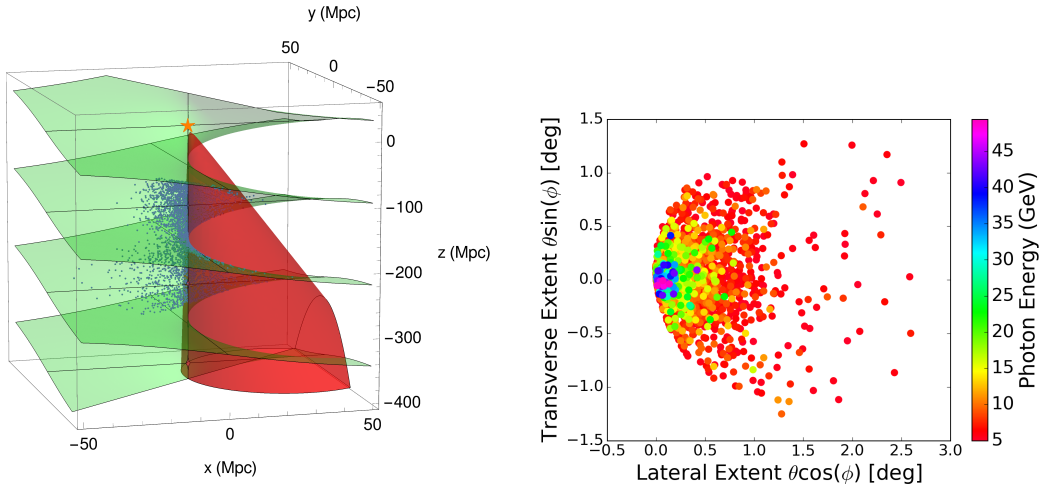

Figure C.6: Example of how a blazar with a jet will only shine and activate a small region of the PP surface (left) and the resultant halo (right). The magnetic field is given in Eq. (C.21) with $B_0 = 10^{-14}$G, $\lambda = 250$ Mpc.

observed gamma rays. For instance, Fig. C.6 presents an example in which the source has a jet with half-opening angle $\theta_{\rm jet} = 5^\circ$ and the magnetic field is given by Eq. (C.21). The jet direction is chosen so that the Earth lies within the cone of the jet and the blazar can be seen directly. The left plots in both figures shows that the jet picks out a small region of the PP surface, and the right plots show the resulting halo.

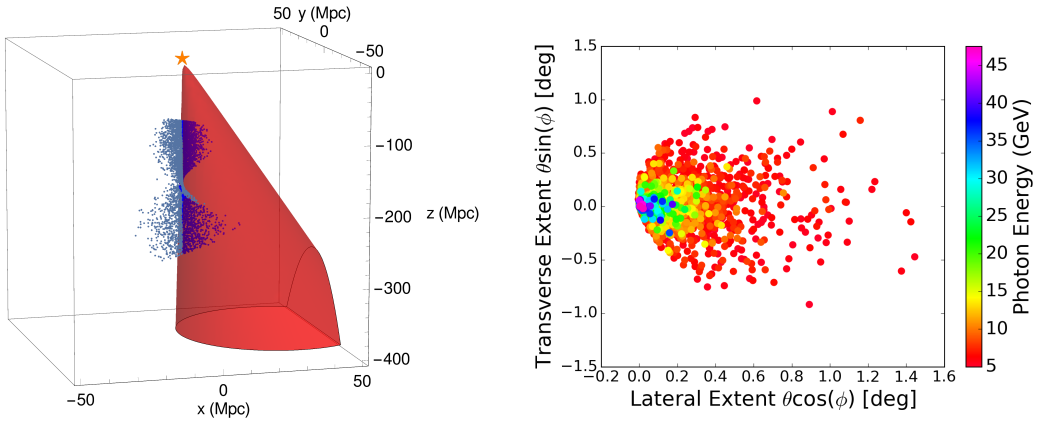

Figure C.7: Monte Carlo simulation using the magnetic field of Eq. (C.21) and with the same setup as in Fig. C.6 but with B_0 reduced to $5 \times 10^{-15} G$. Compared to the right panel of Fig. C.6, we see that the high energy gamma rays (blue and green points) are more clustered and so the halo size is smaller at fixed energy.

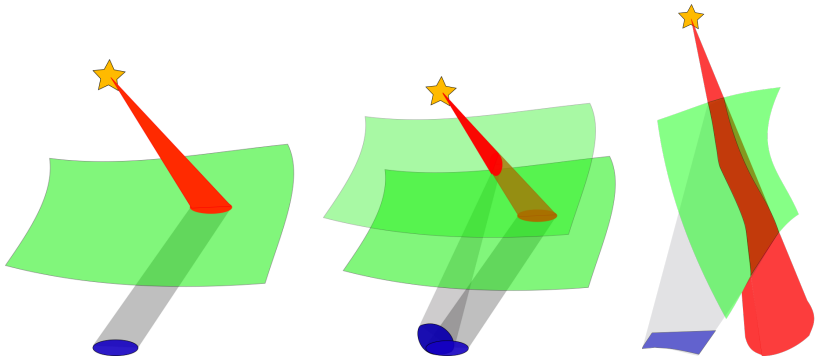

Figure C.8: Sketch of a blazar jet shown in red intersects the green PP surface which delimits the shape of the halo (shown in blue) as seen by some observer. The halo photons must be distributed in the blue region. A situation similar to the one depicted in the middle and third sketch can be seen from the simulations in Fig. C.6 and Fig. C.9 below. The differences between the many possible shapes arise due the characteristics of the intersection between the blazar's jet and the PP surface.

C.5 Parameter Dependence of Halo Morphologies

In this section we discuss the structure of the halo as the parameters B_0, λ and the sign of the helicity of the maximally helical magnetic field in Eq. (C.21) are varied. The concept of the PP surface will be a useful tool for this discussion as it allows us to clearly see how the magnetic field dictates the halo's shape.

The magnetic field strength directly affects the amount of bending of the lepton trajectories since the gyroradius $R_L \propto 1/B_0$. Therefore a weak magnetic field will require that the initial TeV gamma ray is already propagating nearly towards Earth. Thus reducing B_0 will shrink the size of the halo at any given gamma ray energy, although lower energy gamma rays may now enter the field of view. This can be seen in Fig. C.7 which was created using $B_0 = 5 \times 10^{-15}$ G and $\lambda = 250$ Mpc. The plot looks almost identical to Fig. C.6, which was created using $B_0 = 10^{-14}$ G, except that the extent of the halo in the x and y directions, for photons of the same energy, has shrunk by a factor of ~ 2.

If one does not track the photon's energy, the effect of a change in B_0 is not easily seen through the morphology of the halos as their shapes and sizes are determined by the intersection of the jet and the PP surface. We show a few examples of this interplay in the sketch of Fig. C.8. Understanding this could allow us to learn valuable information about the inter-galactic magnetic field in the region probed by the PP locations by observing the halo's shape. In a real situation, we cannot observe the full halo shape as it will be contaminated by background photons coming from other sources. However, we can still extract certain useful halo information since the background is expected to be stochastically isotropic and certainly not parity odd.

Another important thing to note is that we have assumed the jet and the power spectrum to be fixed on the timescale necessary for the creation of the halos. Namely, the path length of two events (i.e. the sum of the magnitude of the two vectors shown in Fig. C.1) will differ as a function of their bending angle. Hence this can introduce a significant time delay between the subsequent observations of two initial TeV photons emitted from the source at the same time. If this time delay is large, as would occur for events whose PP locations are Megaparsecs apart, we would expect the source dynamics to alter its power spectrum and jet direction in that timeframe – making our fixed jet assumption false. A quick change in jet direction would translate in observed events arising from potentially very different regions of the PP surface. Fortunately, this should not affect our final results once we average over many realizations as this already stacks random jet oritentations together. A large power spectrum variability could introduce more drastic effects but we will neglect this complication in this initial exploration.

Let us quickly comment on the dependence of the morphology on the coherence length of **B**. As can be seen from Eq. (C.3), the MFP $D^c_{\gamma 0}$ of the TeV photons are of the order of $10-100$ Mpc. Any magnetic field with coherence length much larger than $D^c_{\gamma 0}$ will appear constant in space. On the other hand, for $\lambda_c \ll D^c_{\gamma 0}$, the halo will be produced from a rapidly varying part of the PP surface and will be more scattered.

The helicity of the magnetic field in Eq. (C.21) can be flipped by changing $x \to -x$. A flip in the helicity simply leads to a parity inversion of the PP surface and the halo spiral also changes handedness. However, to get more statistics, we will investigate both helicities using independent simulations in Sec. C.7.

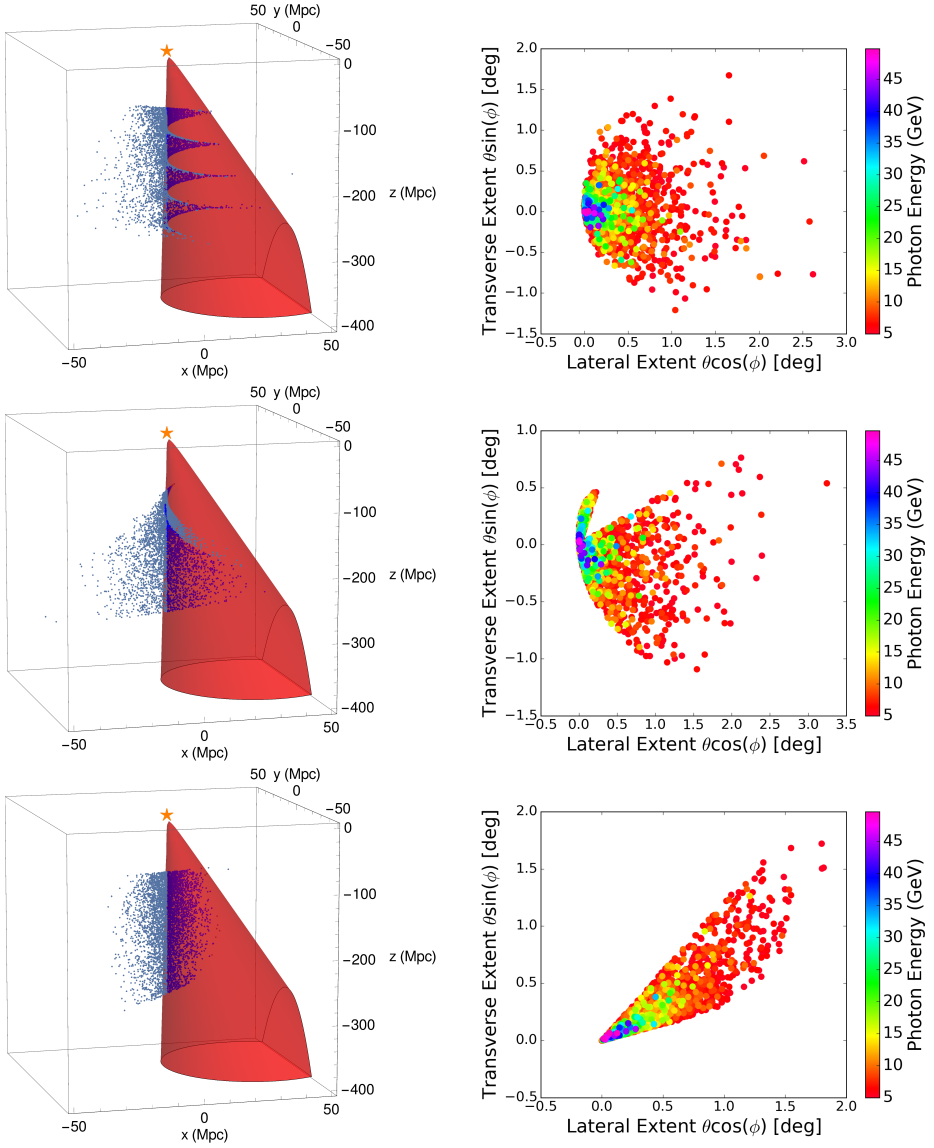

Figure C.9: The PP locations on the PP surface and jet (left) and corresponding halo (right) for $\lambda = 100, 500, 2000$ Mpc for the magnetic field in Eq. (C.21) with $B_0 = 10^{-14}$ G. The direction to the source is at $\theta = 0$.

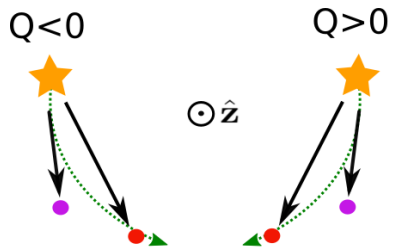

Figure C.10: Illustration of the Q-statistic. The plot represents two blazar halos in the observational plane, each halo with just two photons, one at high energy (purple) and the other at low energy (red). The image of the blazars is denoted by the stars and the line of sight to the blazar (along $\hat{\mathbf{z}}$) points out of the plane of the page as denoted by the arrow tip. The left sketch shows a situation where $Q < 0$ since $\mathbf{n}_{\rm red} \times \mathbf{n}_{\rm purple} \cdot \mathbf{n}_{\rm blazar} < 0$; similarly the sketch of the blazar on the right shows a $Q > 0$ situation.

C.6 The Q Statistic

One of the main goals of this work is to determine if the helicity of the inter-galactic magnetic field can be deduced from the shape of the blazar halos. As we have seen, under certain conditions, a helical inter-galactic magnetic field can produce a clear spiral-like structure in a gamma ray halo. Hence it is important to develop a statistical technique that is sensitive to this structure. A statistic, called Q, was developed in Ref. [175], and was applied to the *diffuse* gamma ray background observed by the Fermi telescope in Refs. [162, 163]. A non-zero value of Q was observed with high confidence in comparison to Monte Carlo simulations that assume no inter-galactic magnetic field.

One can see from the halo plots above, *e.g.* Fig. C.3, that the arrival direction of high energy photons tend to lie closer to the blazar line-of-sight than those for lower energy photons. Hence different locations of the PP surface are sampled by photons of different energies and the observed gamma rays can carry an imprint of any curvature or twist of the PP surface. More precisely, the work of Ref. [175] showed that a left (right) handed helical magnetic field will create left (right) handed spiral patterns in the observed photons.

Below we briefly review the idea behind a slightly modified version of the Q statistic proposed in Ref. [175]. We will apply the statistics on regions surrounding an observed blazar whose angular position will be denoted by the unit vector $\mathbf{n}^{(3)} = \hat{\mathbf{z}}$. We consider a disk of radius R centered on the location of the source and consider the set of photons within this disk. These photons are binned according to their energies into non-overlapping bins ΔE_1, ΔE_2. We use N_2 to denote the number of photons in bin ΔE_2 within the disk of radius R. We then perform the sum,

$$Q(\Delta E_1, \Delta E_2, R) = -\mathbf{n}^{(3)} \cdot \left(\frac{1}{N_2} \sum_{j=1}^{N_2} \mathbf{n}_j^{(2)} \times \left[\frac{\sum_{i=1}^{N_1} \mathbf{n}_i^{(1)} \Theta(\mathbf{m}_i^{(1)} \cdot \mathbf{m}_j^{(2)})}{\sum_{i=1}^{N_1} \Theta(\mathbf{m}_i^{(1)} \cdot \mathbf{m}_j^{(2)}) + \varepsilon} \right] \right) \tag{C.25}$$

where $\mathbf{n}_i^{(a)} \equiv \mathbf{n}_i(\Delta E_a)$ is the unit vector denoting the arrival direction of photon i in bin a; $\mathbf{m}_i^{(a)}$ is the unit vector obtained by projecting $\mathbf{n}_i^{(a)}$ on to the xy-plane: $\mathbf{m}_i^{(a)} = \mathbf{n}_i^{(a)} - (\mathbf{n}_i^{(a)} \cdot \hat{\mathbf{z}})\hat{\mathbf{z}}$. We've also introduced the infinitesimal quantity ε to keep the denominator from vanishing. The original Q statistic in Ref. [175] was defined without the Heaviside function (Θ) in Eq. (C.25). We illustrate the $Q-$statistic in Fig. C.10.

In the presence of background gamma rays in addition to the blazar gamma rays, we expect $Q(R)$ to start near 0 at $R = 0$, grow to a peak value near $R = R_{\rm halo}$, where $R_{\rm halo}$ is the angular radius of the halo, and finally come back down towards 0 at large R where the signal becomes background dominated. However in mock maps with no background, the value of Q should asymptotically flatten out to its maximal value attained at $R_{\rm halo}$, and its value will be negative (positive) for right (left) handed magnetic fields. We can see this behavior in Fig. C.11 where we simulate the halo without any stochasticity and with the magnetic field of Eq. (C.21).

To showcase the Q-statistic in this paper we will separate the gamma rays in three

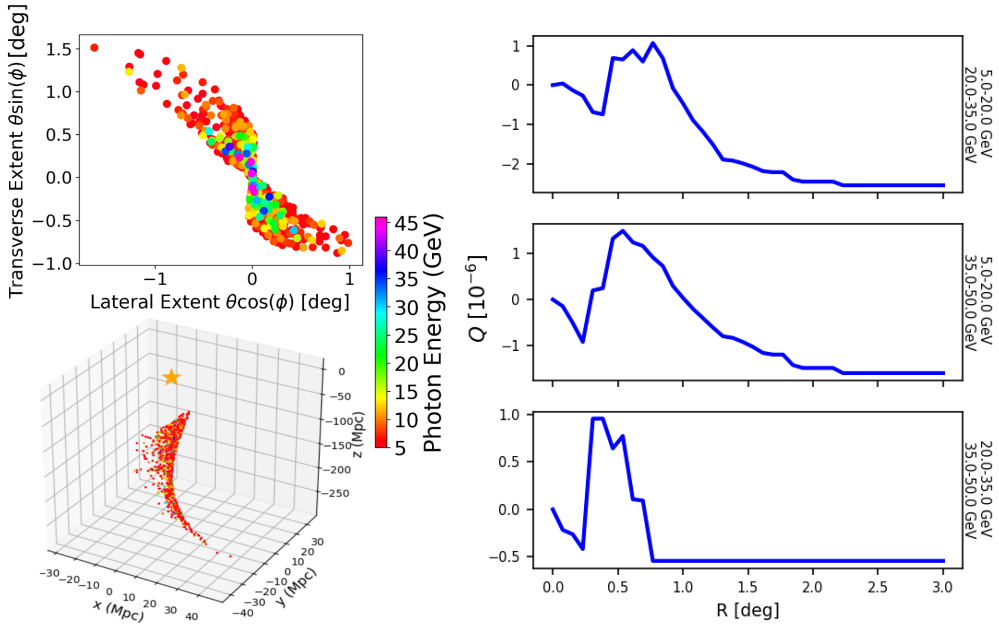

Figure C.11: (Top Left) A set of simulated observed photons from the halo formed by a blazar's jet with half-opening angle of 5°. The surrounding random magnetic field was created with parameters described in Eq. (C.28) and has the form given by Eq. (C.27). (Bottom Left) The PP locations of the photons responsible for the halo. (Right) The result of applying the Q-statistic to the observed photons on the right.

energy bins:

$$\Delta E_1 = (5,20),\ \Delta E_2 = (20,35),\ \Delta E_3 = (35,50), \tag{C.26}$$

all numbers in GeV. This choice was the real reason we only simulated photons between 5 to 50 GeV.

C.7 The Q Statistic Applied to Stochastic Magnetic Fields

The result of Fig. C.11 is noisy and can be misleading as we are dealing with random magnetic fields. Indeed, these fields can sometimes create halos whose Q-statistics suggest the wrong helicity. It is therefore important to average over many realizations of the magnetic field and the jet orientation. Each realization will simulate a blazar with a jet of half-opening angle $\theta_{\rm jet} = 5^\circ$ and having Earth in its LoS. The jet is also constrained to generate a halo

with at least 3 events in order for the statistics to be applied; this condition is easily satisfied if Earth is in the jet's LoS. Jets pointing further away from the LoS might still yield observable photons but we would not be able to identify these blazars and so we don't simulate those cases.

We will consider magnetic fields of the form,

$$\mathbf{B}(\mathbf{x}) = \frac{1}{2N^2+2} \sum_{\mathbf{k}\in K} \mathbf{b}(\mathbf{k}, f_{\rm H}, B_{\rm rms}) e^{i\mathbf{k}\cdot\mathbf{x}} \tag{C.27}$$

with the set K consisting of $2N^2+2$ vectors which have magnitude $k_{\rm mag}$ and whose directions are approximatively uniformly spread over the unit sphere. Half of the Fourier coefficients $\mathbf{b}(\mathbf{k}, f_{\rm H}, B_{\rm rms})$ are drawn from their respective distribution as outlined in Appendix C.9, while the other half are set by the requirement $\mathbf{b}(\mathbf{k}, f_{\rm H}, B_{\rm rms}) = \mathbf{b}^*(-\mathbf{k}, f_{\rm H}, B_{\rm rms})$, necessary for obtaining a real value for the magnetic field. The value of $-1 \leq f_{\rm H} \leq 1$ controls the handedness of the field, namely $f_{\rm H} = 1$ (-1) corresponds to a maximally right-handed (left-handed) helical field. Finally $B_{\rm rms}$ determines the root mean square of $\mathbf{B}(\mathbf{x})$.

In Fig. C.11 we compute the Q-statistics for 100 realizations of halos created with a random magnetic field created using the parameters

$$\begin{aligned} B_{\rm rms} &= 1\times 10^{-14}\,{\rm G},\ k_{\rm mag} = 0.01/{\rm Mpc}, \\ f_{\rm H} &= +1,\ 2N^2+2 = 27, \end{aligned} \tag{C.28}$$

where $2N^2+2$ is the number of directions of the $\mathbf{k}$ vector in Eq. (C.27). In Fig. C.12 we plot the average of Q over all the realizations, denoted $\overline{Q}(R)$, for the same runs as in Fig. C.11 and for the three gamma ray energy bin combinations. By doing so, we have in mind of averaging the Q-statistics obtained from small regions around multiple observed blazars. The plot also shows the standard error in $\overline{Q}(R)$ which is given by the standard deviation of $Q(R)$ divided by the square root of the number of realizations in the Monte Carlo simulations. The standard error follows from the central limit theorem and is the

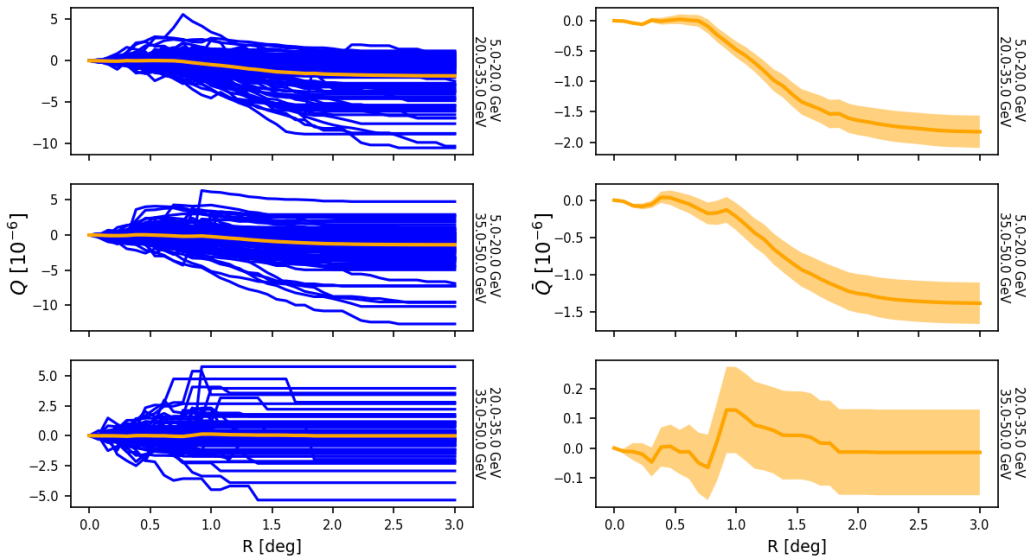

Figure C.12: (Left) $Q(R)$ versus R for 100 Monte Carlo runs when the stochastic magnetic fields are generated using the parameters shown in Eq. (C.28) with $f_H = +1$. The mean $\overline{Q}(R)$ is shown by the orange curve. (Right) A zoomed-in view of $\overline{Q}(R)$. The width of the error band is given by the standard error *i.e.* standard deviation of the 100 Monte Carlo $Q(R)$ values divided by the square root of the sample size (100).

error in using the sample mean to estimate the population mean. However, it assumes that the samples, Monte Carlo simulations in our case, from which values of $Q(R)$ are drawn are independent and identically distributed. This is certainly true in our setup but may not be true for actual observations in which the same photons might contribute to the $Q(R)$ calculated for blazars that are close to each other. In addition, there will be variation in the distance to observed blazars and other source characteristics. We plan to take some of these factors into account in a follow-up analysis.

Pushing the statistics further, we are clearly able to distinguish between many different properties of the magnetic field as the number of realization increases. For instance, we have plotted $\overline{Q}(R)$ versus R for 1000 Monte Carlo simulations for $f_H = 0, \pm 1$ (Fig. C.13) and the plots show a clear correlation between $\overline{Q}(R)$ and the helicity of the magnetic field. We can also notice distinct oscillations that occur at small R. It is also reassuring that the

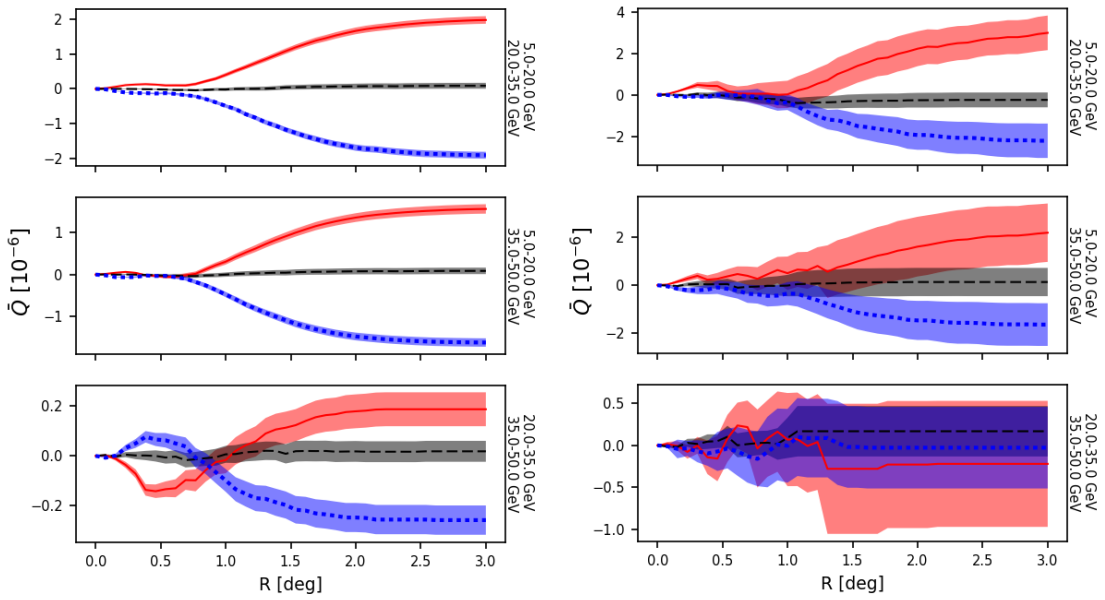

Figure C.13: $\bar{Q}(R)$ versus R when averaging for 1000 simulations (left) and 20 simulations (right). The realizations had parameters $f_{\rm H} = -1$ (red, solid), $f_{\rm H} = 0$ (black, dashed) and $f_{\rm H} = +1$ (blue, dotted) for the three energy bin combinations: $(\Delta E_1, \Delta E_2)$ (top row), $(\Delta E_1, \Delta E_3)$ (middle row) and $(\Delta E_2, \Delta E_3)$ (bottom row) where the bins are defined in Eq. (C.26). The other parameters of the stochastic magnetic fields are given in Eq. (C.28) and the bands denote standard error of $\bar{Q}$.

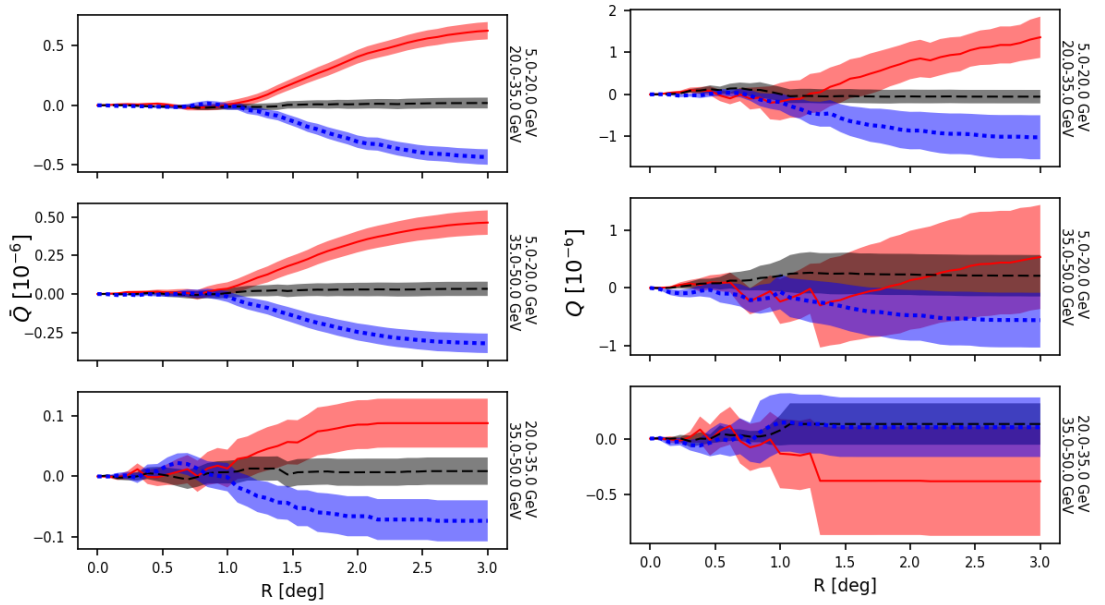

Figure C.14: Analysis of the same data as found in Fig. C.13 but computed with the original definition of Q. Namely, we replaced the Θ term in Eq. (C.25) by 1. It is clear both from the magnitude and the size of the error bars that the modified Q is a sharper statistics.

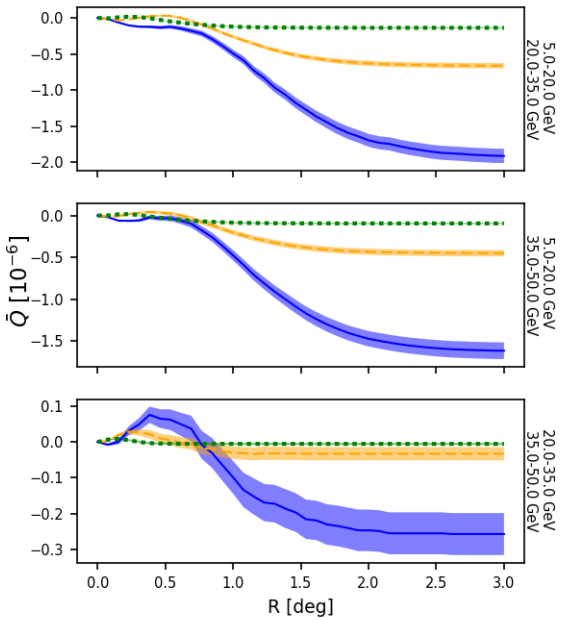

Figure C.15: $\bar{Q}$ versus R for 1000 simulations with $B_{\rm rms} = 10^{-14}$ G (blue,solid), 5×10^{-15} G (orange, dashed), and $2 \times 5 \times 10^{-15}$ G (green, dotted) and $f_H = 1$, $k = 0.01/\text{Mpc}$.

$f_H = +1$ plot is the mirror image of the $f_H = -1$ curve, just as we would expect due to parity reflection. Within the clean context studied here, we only need $\sim 10-20$ halos before we can detect the sign of the helicity through the sign of the Q's at large R. However this number depends heavily on the properties of the magnetic field, source variability and background. Hence the determination of the exact amount of data required to make such detection will require a careful analysis of these parameters and therefore is relegated to future work.

In Fig. C.14, we show that the Θ factor in our definition of Q in Eq. (C.25) improves the resolution. Without the Θ factor, the Q-statistic is determined by the cross product of the *average* arrival direction of the photons (in two energy bins) within a radius R of the source. Because of the electron-positron symmetry, photons tend to arrive on either side of the source (see Fig. C.4), and the average arrival direction tends to be near the origin. Introducing the Θ factor ensures that for every high energy photon selected, we only average

the low energy photons that arrive on the same side with respect to the source. Then there is a larger contribution to the value of Q. Essentially the Θ term limits the sum to gamma rays within the electron (or the positron) branch of the halo (see Fig. C.4).

Next we examine the dependence of $\overline{Q}(R)$ on magnetic field parameters. In Fig. C.15 we plot $\overline{Q}(R)$ for several different magnetic field strengths and for fixed helicity $f_H = 1$. We see that increasing the magnetic field strength leads to an increasing amplitude of $\overline{Q}$ for *all* energy combinations. The increase is due to the magnitude of $\mathbf{n_1} \times \mathbf{n_2}$ which becomes larger as the bending allows $\mathbf{n_1}$, $\mathbf{n_2}$ to point further apart.

The effect of changing the magnetic field coherence scale is shown in Fig. C.16 where the magnetic field strength and other parameters are fixed and only $k_{\rm mag}$ is varied. The magnetic field with larger coherence length gives a larger signal, but there is a turning point as extremely large coherence scale fields will behave like uniform fields. The signal for smaller correlation length is washed out but the suppression depends on the energy combination. This is to be expected from the analysis of Ref. [175] since $\overline{Q}$ with a certain energy combination is sensitive to the magnetic helicity power spectrum at a definite coherence scale that is determined by the combination of energies. To probe magnetic fields on small length scales, it is necessary to consider gamma rays whose energies are close together [175]. Thus the energy bins also have to be smaller and this means that the statistics is poorer.

C.8 The Features at Small R

The Q-statistic is essentially a measure of the differential rotation found in the arrival direction of photons of different energies. Q will be negative (positive) if the rotation is right (left)-handed as is depicted in Fig. C.10. The results of our Monte Carlo simulations, for example in Fig. C.13, show that $\overline{Q}$ has some oscillation at small R which is made abun-

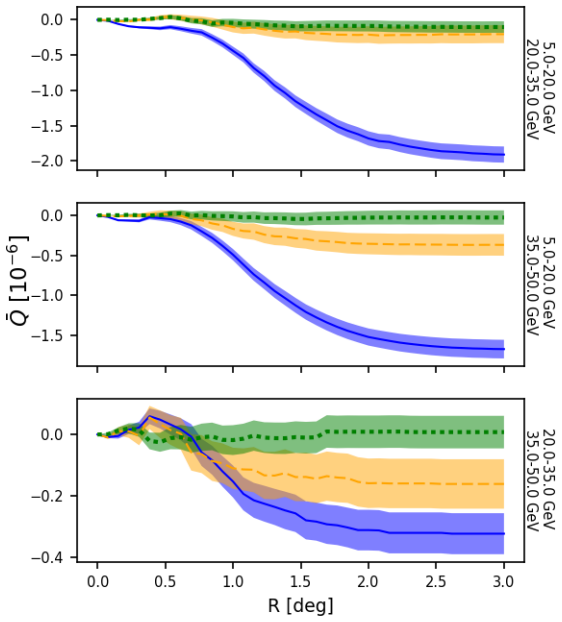

Figure C.16: $\overline{Q}$ versus R for 1000 simulations with $k = 0.01/\text{Mpc}$ (solid, blue), $k = 0.05/\text{Mpc}$ (orange, dashed), $k = 0.1/\text{Mpc}$ (green, dotted) with $B_{\text{rms}} = 1 \times 10^{-14}$ G and $f_H = +1$.

dantly clear for the $\overline{Q}$ using the largest energy bins. Here we provide an explanation of this small R feature. What the Q-statistic allow us to probe is the shape of the PP surface. As already mentioned, it is clear from Fig. C.11 that high energy photons are found close to the LoS and the low energy ones are further out. However there is another important piece of information, namely the z coordinate of their PP locations; generally z will be small (more negative) if it is low on the PP surface and hence close to Earth.

Remember that to give a contribution to Q, one requires a high energy photon (γ_{HE}) and a low energy photon (γ_{LE}) as is shown in Fig. C.10. If most γ_{LE} photons have PP locations higher up on the PP surface than the γ_{HE}'s, the Q-statistic measures the twist of the PP surface as one traverses it from bottom to the top. This is in contrast to whenever the low energy photons originate from PP locations close to Earth when compared to those of γ_{HE}. As the twist is parity odd, these two cases contribute to $\overline{Q}$ with opposite signs and is the reason for these oscillations.

We can understand this effect explicitly with a little bit more thought. When R is very small, we expect to see events with small bending angles. These mainly occur when the lepton upscatters a photon towards Earth early after it was pair produced. The small R observed γ_{HE} (γ_{LE}) photons must therefore have originated from TeV leptons with high (low) energies. Because TeV gamma ray have a MFP that decreases with energy, we then expect the γ_{LE} to be produced at PP locations closer to Earth than the γ_{HE} ones, therefore Q initially measures the twist from top to bottom and $|Q|$ grows as R departs from 0.

However as R increases further two things occur. First, the observed photons entering the field of view come from events experiencing more bending that at small R. This means that the lepton had to travel further and in the process has loss more energy, therefore the maximal energy of the new photons will be lower and won't contribute to the high energy bin. Hence the average z of the PP location of the high energy photons is fixed at small R. Second, most of the volume entering the field of view will be located closer to the source due to projection effects. For this reason, the events from PP locations at high z starts to enter the field of view at a quicker rate than the events at low z. We are now in the reverse situation: a large majority of photons γ_{LE} have PP locations that are higher than the ones for the γ_{HE}. This gives a contribution to Q with the opposite sign pulling the total towards 0 and sometimes even pushes it across (compare the top and bottom panel of Fig. C.13). Finally when R becomes large, the low energy events with PP locations at small z and far from the LoS start contributing to Q and dominate. This process, depicted in Fig. C.17, is responsible for the features before the value of Q flattens out to its asymptotic value.

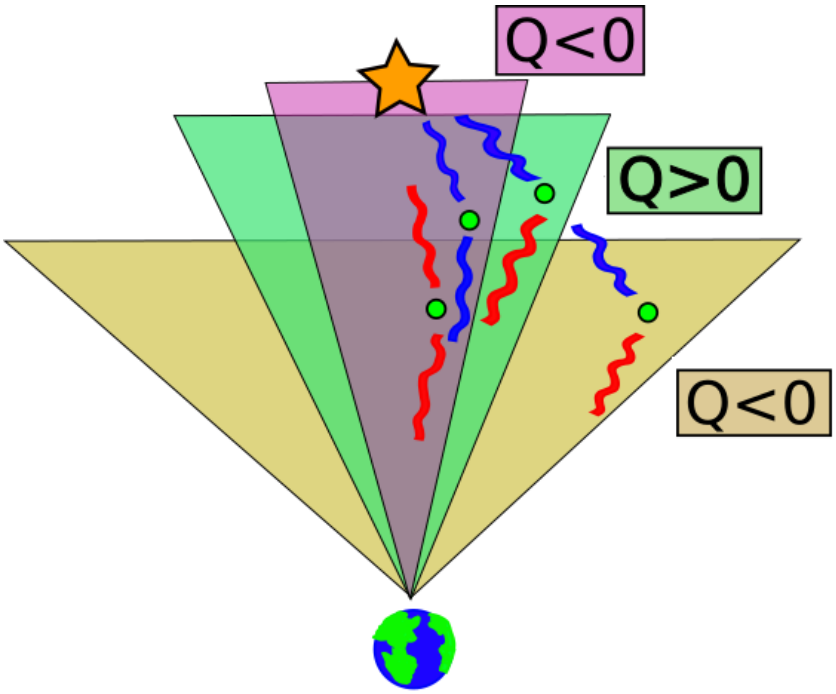

Figure C.17: The sign of the Q-statistic when applied to a halo produced by a magnetic field with $f_H = 1$. Here the squiggly lines represents photons of high (blue) and low (red) energies. The top photons are the initial TeV gamma rays, the green points are the PP locations and the bottom photons are the upscattered GeV photons that are eventually observed. At small R, the events with small bending allows the Q-statistic to measure the twist of the PP surface from top to bottom (purple shaded region, $Q < 0$). When R gets larger and PP surface region near the blazar enters the field of view, the new events entering the field of view contribute to Q with the opposite sign as they are located further up the PP surface than the high energy events which only occurs close to the LoS (green shaded region, $Q > 0$). Finally as R gets large and the whole halo is exposed, the overwhelming low energy events at low z and far from the LoS dominates the signal and drives Q towards its asymptotic value (brown shaded region, $Q < 0$).

C.9 Generation of Isotropic Random Magnetic Fields

In this section we give additional details to the interested reader regarding our methods to generate helical magnetic fields. We achieve this by first decomposing the magnetic field $\mathbf{B}(\mathbf{x})$ in circularly polarized modes with basis vectors $\mathbf{K}^{\pm}(\mathbf{k})$ that are divergence-free eigenfunctions of the Laplace operator

$$\mathbf{K}^{\pm}(\mathbf{k}) = \mathbf{e}^{\pm}(\mathbf{k})\mathrm{e}^{i\mathbf{k}\cdot\mathbf{x}} \equiv \frac{\mathbf{e_1}(\mathbf{k}) \pm i\mathbf{e_2}(\mathbf{k})}{\sqrt{2}}\mathrm{e}^{i\mathbf{k}\cdot\mathbf{x}}. \tag{C.29}$$

The triad of unit vectors, $\{\mathbf{e_1}, \mathbf{e_2}, \mathbf{e_3}\}$, is constructed as

$$\mathbf{e}_1 \equiv \frac{\mathbf{n}_0 \times \hat{\mathbf{k}}}{|\mathbf{n}_0 \times \hat{\mathbf{k}}|},\ \mathbf{e}_2 \equiv \frac{\hat{\mathbf{k}} \times \mathbf{e}_1}{|\hat{\mathbf{k}} \times \mathbf{e}_1|},\ \mathbf{e}_3 = \frac{\mathbf{k}}{k} \equiv \hat{\mathbf{k}} \tag{C.30}$$

where $\mathbf{n}_0$ is any chosen unit vector such that $\mathbf{n}_0 \neq \hat{\mathbf{k}}$.

With these definitions, the $\mathbf{e}$'s form a right-handed orthonormal system and we have,

$$\nabla \cdot \mathbf{K}^{\pm} = 0,\ \nabla \times \mathbf{K}^{\pm} = \pm k\mathbf{K}^{\pm},\ \mathbf{K}^{\pm *}(\mathbf{k}) = -\mathbf{K}^{\pm}(-\mathbf{k}) \tag{C.31}$$

Hence any magnetic field can be decomposed as,

$$\begin{aligned} \mathbf{B}(\mathbf{x}) \quad &= \int \frac{d^3k}{(2\pi)^3}\mathbf{b}(\mathbf{k})\mathrm{e}^{i\mathbf{k}\cdot\mathbf{x}} \\ &= \int \frac{d^3k}{(2\pi)^3}\left[b^{+}\mathbf{K}^{+} + b^{-}\mathbf{K}^{-}\right], \end{aligned} \tag{C.32}$$

with the condition that

$$b^{\pm *}(\mathbf{k}) = -b^{\pm}(-\mathbf{k}) \tag{C.33}$$

to ensure that $\mathbf{B}(\mathbf{x})$ is real. The divergence-free condition, $\nabla \cdot \mathbf{B} = 0$, is automatically satisfied in this procedure.

We are interested in generating random magnetic fields with given energy ($E_B(k)$) and helical ($H_B(k)$) power spectra. The relations between the modes $b^{\pm}(\mathbf{k})$ and the power

spectra are given by

$$\frac{1}{8\pi}\langle|\mathbf{B}(\mathbf{x})|^2\rangle = \int \frac{k^2 dk}{16\pi^3}\left[|b^+|^2 + |b^-|^2\right] \equiv \int E_B(k) d\ln(k) \tag{C.34}$$

and

$$\langle \mathbf{A}(\mathbf{x})\cdot\mathbf{B}(\mathbf{x})\rangle = \int \frac{k dk}{2\pi^2}\left[|b^+|^2 - |b^-|^2\right] \equiv \int H_B(k) d\ln(k). \tag{C.35}$$

The ratio of E_B and H_B will be written in terms of a function $f_H(k)$ as [166],

$$H_B(k) = f_H(k)\frac{8\pi}{k}E_B(k), \tag{C.36}$$

and the "realizability condition" leads to the restriction

$$-1 \leq f_H(k) \leq 1 \tag{C.37}$$

The field is non-helical if $f_H = 0$, maximally right-handed if $f_H = +1$, and maximally left-handed if $f_H = -1$.

Eqs. (C.34), (C.35) and (C.36) allow us to write,

$$|b^\pm|^2 = \left(\frac{2\pi}{k}\right)^3 [1 \pm f_H(k)] E_B(k). \tag{C.38}$$

Hence the modes $|b^\pm(\mathbf{k})|$ are drawn from a normal distribution with mean $\mu^\pm = 0$ and standard deviation $\sigma^\pm = (1 \pm f_H)(2\pi/k)^3 E_B(k)$. We then include a uniformly drawn phase angle $\theta^\pm(\mathbf{k}) \in [0, 2\pi)$ which yields,

$$b^\pm(\mathbf{k}) = |b^\pm(\mathbf{k})| e^{i\theta^\pm(\mathbf{k})} \tag{C.39}$$

In this paper we focus on stochastic magnetic fields that are *isotropic* but have power on a single length scale $\lambda_c = 2\pi/k_{\rm mag}$ and that have either $f_H(k) = 0$ or $f_H(k) = \pm 1$. This corresponds to a delta function distribution for $E_B(k)$ and vanishing or maximal helicity of either sign. To ensure that the magnetic fields are stochastically isotropic, we choose

N^2+1 vectors $\mathbf{k}_n$ ($n=1,...,N^2+1$) that discretize half of the two-sphere of directions in $\mathbf{k}-$space,

$$\mathbf{k}_n = k_{\rm mag}(\sin\theta_i\cos\phi_j, \sin\theta_i\sin\phi_j, \cos\theta_i), \tag{C.40}$$

with

$$\theta_i = \cos^{-1}\left(\frac{2i-1}{N}-1\right),\ \phi_j = 2\pi\frac{(j-1)}{N}, \tag{C.41}$$

for $i,j=1,\ldots,N$, and

$$k_{N^2+1} = k_{\rm mag}(0,0,1) \tag{C.42}$$

Once we have $\mathbf{k}$ and $b^{\pm}(\mathbf{k})$ as described above, we compute

$$\mathbf{b}(\mathbf{k}) = b^{+}\mathbf{K}^{+} + b^{-}\mathbf{K}^{-} \tag{C.43}$$

for every $\mathbf{k}=\mathbf{k}_n$. We also find $\mathbf{b}(-\mathbf{k})$ using the reality condition

$$\mathbf{b}(-\mathbf{k}) = \mathbf{b}^{*}(\mathbf{k}). \tag{C.44}$$

Finally we obtain the random magnetic field,

$$\mathbf{B}(\mathbf{x}) = \frac{\mathbf{1}}{(\mathbf{2N^2+2})}\sum_{\mathbf{k}\in\mathbf{K}}\mathbf{b}(\mathbf{k})\mathbf{e}^{\mathbf{ik\cdot x}} \tag{C.45}$$

where K is the set of vectors $\{\mathbf{k}_n, -\mathbf{k}_n\}$ for $n=1,\ldots,N^2+1$.

C.10 Conclusion

We have studied the effect of stochastic inter-galactic magnetic fields on the morphology of gamma ray halos. The dependence of the morphology on the magnetic field strength, the coherence length, and the helicity were investigated. Most importantly, we have provided an understanding of the structure of the halo in geometrical terms, as arising due to the "PP surface" as determined by the magnetic field. In simple cases, the PP surface can be found analytically (for example, Eq. (C.24)).

To analyze the halo morphology, we have proposed a sharper version of the Q-statistic in Eq. (C.25) and applied it to simulated halos. Our key finding is that Q is a powerful diagnostic of the magnetic helicity (Fig. C.13), field strength (Fig. **??**) and coherence scale (Fig. C.16). Based on the analytical work of Ref. [175], we expect the sensitivity of Q to the coherence scale to depend crucially on the energies of the gamma rays that are used. It would be interesting to quantitatively examine how the sensitivity of Q to the coherence scale can be improved with a choice of energy bins.

In addition, our Monte Carlo simulations have revealed a bump in $\overline{Q}(R)$ at small values of R (see Fig. C.13). We have understood and explained this feature in terms of the PP surface in Sec. C.8. This new feature may become useful in the analysis of real data in the future.

Our present study is limited in a few ways that we plan to overcome in future work. First, we have not included any background gamma rays. These will introduce noise in the evaluation of $\overline{Q}$ and the error bars will increase. We have also limited ourselves to stochastic isotropic magnetic fields but with only one $|\mathbf{k}|-$mode. This is useful at this stage as it allows us to diagnose the effects of changing the coherence scale. In future, we plan to include a spectrum of the magnetic field as motivated by current observations [169]. In future we also plan to incorporate the full development of the electromagnetic cascade into our numerical code, perhaps along the lines of Ref. [172] or [174]. Once we have understood individual blazar halos, we will apply our techniques to the diffuse gamma ray background which is expected to contain halos due to unseen blazars as well as those due to identified blazars.

APPENDIX D

CO-AUTHORS PERMISSION STATEMENT

Permission to use the published work of Chapters 3, 5 and Appendix C as part of the thesis was granted by all co-authors: Yi-Fu Cai, Damien Easson, Tanmay Vachaspati and Dong-Gang Wang.